NASA TECHNICAL MEMORANDUM

NASA TM X-2626

NASA TM X-2626

FLIGHT INVESTIGATION OF 24° BOATTAIL NOZZLE DRAG AT VARYING SUBSONIC FLIGHT CONDITIONS

by Roger Chamberlin

Lewis Research Center

Cleveland, Ohio 44135

NATIONAL AERONAUTICS AND SPACE ADMINISTRATION • WASHINGTON, D. C. • NOVEMBER 1972

1. Report No.	2. Government Accession No.	3. Recipient's Catalog No.
NASA TM X-2626		

4. Title and Subtitle	5. Report Date
FLIGHT INVESTIGATION OF 24° BOATTAIL NOZZLE DRAG AT VARYING SUBSONIC FLIGHT CONDITIONS	November 1972
	6. Performing Organization Code
7. Author(s)	8. Performing Organization Report No.
Roger Chamberlin	E-6846
	10. Work Unit No.
9. Performing Organization Name and Address	764-74
Lewis Research Center National Aeronautics and Space Administration Cleveland, Ohio 44135	11. Contract or Grant No.
	13. Type of Report and Period Covered
12. Sponsoring Agency Name and Address	Technical Memorandum
National Aeronautics and Space Administration Washington, D. C. 20546	14. Sponsoring Agency Code

15. Supplementary Notes

16. Abstract

Four configurations of rounded shoulder boattail nozzle were tested on an underwing nacelle mounted on an F-106B aircraft. A J85-GE-13 turbojet engine provided primary flow. The effects of various parameters on boattail drag were investigated at Mach numbers of 0.6 and 0.9. The parameters studied were Reynolds number, angle-of-attack, nozzle pressure ratio, nozzle geometry, and nozzle axial location with respect to the wing. These nozzles simulated nonafterburning configurations appropriate for turbofan powered aircraft with supersonic dash capability. Increasing Reynolds number significantly lowered the boattail drag coefficient of all the nozzles at both $M_0 = 0.6$ and $M_0 = 0.9$.

17. Key Words (Suggested by Author(s))		18. Distribution Statement
Boattail	Flight test	Unclassified - unlimited
Boattail drag	Propulsion system	
Flow separation	Transonic	
Reynolds number effects		

19. Security Classif. (of this report)	20. Security Classif. (of this page)	21. No. of Pages	22. Price*
Unclassified	Unclassified	68	$3.00

* For sale by the National Technical Information Service, Springfield, Virginia 22151

FLIGHT INVESTIGATION OF 24° BOATTAIL NOZZLE DRAG AT VARYING SUBSONIC FLIGHT CONDITIONS

by Roger Chamberlin

Lewis Research Center

SUMMARY

Four configurations of rounded shoulder boattail nozzle were tested on an underwing nacelle mounted on an F-106B aircraft. A J85-GE-13 turbojet engine provided primary flow. The effects of various parameters on boattail drag were investigated at Mach numbers of 0.6 and 0.9. The parameters studied were Reynolds number, angle-of-attack, nozzle pressure ratio, nozzle geometry, and nozzle axial location with respect to the wing. These nozzles simulated nonafterburning configurations appropriate for turbofan powered aircraft with supersonic dash capability.

Increasing Reynolds number significantly lowered the boattail drag coefficient of all the nozzles at both Mach 0.6 and 0.9. The drag reduction was associated with a reduction in the amount of separation on the aft portion of the boattail at high Reynolds numbers. Change in nozzle pressure ratio from 2.3 to 3.8 had little effect on boattail drag. Angle-of-attack had no effect at angles below about 9° to 10° and produced a slight increase in boattail drag at higher angles. At Mach 0.9, increasing the radius of the boattail shoulder reduced the boattail drag. At Mach 0.6, increasing the radius of the boattail shoulder from r/r_c of 0.25 to 0.65 increased boattail drag, and a further increase to 1.00 decreased the drag. This particular effect may be due to the aft underwing nozzle position. Moving the boattail farther aft from the wing trailing edge produced a large increase in boattail drag.

INTRODUCTION

The Lewis Research Center is conducting a flight program to investigate the installed performance of various exhaust nozzles on a turbojet engine (refs. 1 to 4). The powerplant installation being studied is a nacelle mounted under the aft portion of the wing of a modified F-106B aircraft (fig. 1) with the exhaust nozzle just downstream of

the wing trailing edge. Various nozzles designed for supersonic cruise have been tested. The present study is concerned with boattail nozzles designed for use on afterburning turbofan engines on aircraft that would have supersonic dash capability, but which cruise subsonically. In the nonafterburning configuration the boattail angle is high, and the projected boattail area is large. As the boattail angle becomes steeper, there is a greater chance that the external flow will separate. The purpose of this program was to determine the effects of different nozzle geometries and flight conditions on the flow separation characteristics and resulting boattail drag.

Some results on similar boattail nozzles both isolated and installed on a 1/20-scale F-106 model are available from wind tunnel tests. Isolated nozzle data show that decreasing the boattail angle, or rounding the boattail juncture, reduces the amount of separation and the resulting boattail drag (ref. 5) and increasing pressure ratio beyond the design value reduces the drag (ref. 6). Increasing aircraft angle-of-attack on a 1/20 scale F-106 model shows a drag rise at high angles (ref. 7).

Three nozzle geometries were investigated, all with the same 24° boattail angle but designed to have varying corner radii and conical length. Based on isolated data, the first nozzle was very short and was expected to have some separation. The second was longer, had a larger radius at the shoulder, and was expected to be about the shortest nozzle that can be achieved with negligible amounts of separation. The third, a complete circular arc boattail, was the longest of the three. This nozzle was designed to have the shortest possible length and still have very low values of drag. Four nozzles were flight tested, two with the same geometry but with different axial locations relative to the wing. The nozzles were flown two at a time using both the left and right engines (fig. 2). To achieve the low values of jet to nacelle diameter ratio that were needed, the nozzles had small, internal ejector areas. As a result, the J-85 engines could operate only at military or part power. During this flight program, the Reynolds number was varied by changing altitude. In order to hold the other flight conditions (angle-of-attack and Mach number) constant, all the data were taken with the aircraft flying coordinated turns. This permitted us to vary any one of these flight parameters while holding the others constant.

The results include boattail drag coefficient and boattail pressure distribution variations with each of the flight conditions examined and with nozzle pressure ratio, nozzle radius ratio, and nozzle axial location.

APPARATUS AND PROCEDURE

Installation

Details of the airplane modifications and the nacelle-engine assembly are given in

references 2 and 3. A schematic and a photograph of the research nacelle and boattail nozzle are shown in figures 3 and 4. The nacelle was located at the 32-percent semispan with a downward incidence of $4\frac{1}{2}^{\circ}$ (relative to the wing chord) so that the aft portion of the nacelle was tangent to the aft wing lower surface. The nacelle had 0° cant and was positioned to provide approximately 0.64 centimeter (0.25 in.) clearance at the wing trailing edge. Details of the wing modifications, nacelle shape, and mounting strut are given in reference 3. The strut with the wide fairing described in reference 3 was used.

The gas generators for the nozzles were J85-GE-13 turbojet engines with afterburners. The variable-area primary nozzle was locked at 709.7 square centimeters (110 $in.^2$) permitting operation only at military and part power. The secondary cooling air flow was controlled by a rotary valve just ahead of the compressor (fig. 3). Because the ratio of the nozzle exit area to primary area was small ($A_e/A_8 = 1.12$) these nozzles could pump only small amounts of secondary air (1 percent of the primary flow or less); so the secondary flow valve was fixed in the full-open position.

Test Hardware

The four nozzles tested are shown in figure 5. The nozzles were designed to simulate the subsonic configurations of variable geometry supersonic dash nozzles. Figure 6 shows the variations in geometry of the four nozzles. The number designation for each nozzle corresponds to the radius ratio r/r_c multiplied by 100. The radius ratio r/r_c is defined as the ratio of the radius of the boattail shoulder to the radius of a complete circular arc nozzle, with the same boattail angle and ratio of nozzle exit area to nacelle area. Nozzles 25 and 25Ex have the same geometry, but nozzle 25Ex has been shifted 25.4 centimeters (10.0 in.) downstream of the wing trailing edge. All the nozzles had a maximum boattail angle of 24° at the nozzle exit, and a ratio of nozzle exit to nacelle area $A_e/A_{max} = 0.25$. Three values of radius ratio were tested, $r/r_c = 0.25$, 0.65, and 1.00. Nozzles 25, 25Ex, and 65 were part circular arc and part 24° half-angle conic section. The external contours and the other nozzle dimensions are shown in figure 7. A nickel-chromium-base alloy (Rolled Alloy 333) was used for the internal portions of the nozzle, and the external parts were predominantly 304 and 305 stainless steel.

Instrumentation

A new data recording system was developed specifically for the F-106 program (ref. 4), and as a result it was possible to instrument these nozzles quite extensively (see fig. 8). Each nozzle had 10 rows of static pressure orifices, nine in each row

spanning the length of the boattail. The 90 pressure taps were area-weighted to simplify the boattail drag calculations. Ten static pressure orifices were located on the cylindrical section upstream of the boattail.

Tufts were mounted on the upper surface of the left wing and on the upper quadrant of the boattails, and pictures were taken of the tufts with a movie camera in the tail (see fig. 9). New side panels with windows were made for the tail permitting the camera to view the nozzle on either engine or a portion of the left wing. The camera was integrated with the data system so that it ran only during each of the 11.6-second data-scan periods.

Procedure

All the flights were made from Selfridge Air Force Base in Mt. Clemens, Michigan, in a test corridor over Lake Huron. A total of six flights were made; three with nozzles 25 and 65 on the airplane and three with nozzles 25Ex and 100 on the airplane. All data were taken at subsonic Mach numbers, with the majority at $M_0 = 0.6$ and $M_0 = 0.9$. The ranges of flight and engine variables are shown in table I. The data points for pressure ratio variation and for Mach number variation were taken in level flight. All other data were taken in coordinated turns. The means of varying Reynolds number was to change altitude while holding the Mach number constant. By flying in turns angle of attack as well as Mach number could be held constant. Also, at a given altitude and Mach number, angle of attack could be varied by flying tighter turns increasing the load factor. Load factors are also listed in table I. Figures 10 and 11 show elevon deflections with variations in angle-of-attack and altitude. The J-85 engines were run at military power, except to change pressure ratio. A range of pressure ratio was achieved by running the engines between 87- and 100-percent speeds. The engine compressor bleeds open at approximately 97-percent speed.

Data Reduction

Engine airflow was determined using prior engine calibration data (ref. 8) along with in-flight measurements of engine speed, pressure, and temperature at the compressor face. Knowing the compressor inlet flow, the total pressure and temperature at the turbine discharge, and the fuel flow rates, other parameters at the primary nozzle exit, such as effective area A_{E8}, total pressure P_8, and total temperature T_8, were obtained from previous calibrations. The load cells were not operational for this series of flights. All the drag values were determined by pressure integration. The

performance parameter that is presented is a summation of a calculated internal performance, calculated friction drag and the boattail drag from pressure integration.

An error analysis was made to determine the random error band for boattail drag coefficient,

$$C_D = \frac{(p_0 - p_{avg\ boattail})\, A_{boattail}}{q_0\, A_{max}}$$

The calculations were done using one-sigma standard deviations in Mach number M_0 and free-stream static pressure p_0, which are reported in reference 9. Errors in the measurement of the boattail pressures were also taken into account; however, the accuracy of this measurement was improved over that quoted by the manufacturer. The F-106 data system had 10 absolute pressure transducers with an accuracy of ±0.5 percent of full scale in a scanivalve system (ref. 9). The transducer temperature was controlled by heaters to minimize any error due to temperature shifts. One nacelle static orifice on each side of the airplane was monitored by all the transducers on that side of the airplane. This reference pressure was measured by each transducer during each data point. For each data point an average pressure was calculated for the reference orifice on each side of the airplane. All the pressures measured on any one transducer were then adjusted up or down, by the difference between the reference pressure measured by that transducer and the appropriate average value. This technique further reduced the random error possible in the boattail pressure measurement. For each data point the largest difference between the measured reference pressure on any one transducer and the average pressure was used as the one-sigma standard deviation for this measurement. The random error from each of the three parameters, M_0, p_0, and boattail pressure, were combined to give a total error in boattail drag coefficient. These data are presented in figure 12 for nozzle 65 at $M_0 = 0.9$ and $\alpha = 9^\circ$. Similar error analysis presented in reference 9 showed the flight data were more accurate than predicted because assumed errors were based on manufacturer's specifications, which included sources of error not encountered in this application.

RESULTS AND DISCUSSION

Reynolds Number Effect

The most significant effect on boattail drag was produced by changes in Reynolds number. The range of Reynolds number was approximately 2.3×10^7 to 7.0×10^7. The Reynolds number is based on a characteristic length of 5.18 meters (17 ft), which takes

into consideration the wing chord at this station (approximately 7.32 m (24 ft)) and the nacelle length (approximately 3.96 m (13 ft)). For these nozzles there was a marked decrease in drag with increasing Reynolds number (part (a) of figs. 13 to 16). Before giving a possible explanation for this drag reduction, a brief discussion of the flow over the nozzle is pertinent. As the flow approaches the boattail shoulder, the pressure is slightly less than free-stream because of the presence of the wing and the nacelle upstream of this point. Passing over the boattail shoulder the flow overexpands. If the radius of the shoulder is small, making a sharp turn, the overexpansion can be large. Just downstream of the shoulder a recompression begins, and, if the flow is attached, it recompresses along the remaining length of the boattail. At the end of the boattail the flow has generally recompressed to a value greater than the free-stream static pressure. If the flow separates, the point of separation on these nozzles is generally downstream of the shoulder. The overexpansion around the shoulder is the same and so is the recompression until the point of separation. Beyond this point there is only a small rise in the pressure. The result is that this type of separation produces higher boattail drag.

The reduction in drag with increasing Reynolds number was the result of a reduction in the amount of separation on the boattail. This is shown in parts (b) of figures 13 to 16. These figures are based on pressure distributions and tuft pictures. Separation was not always evident from pressure distributions alone, as will be shown later. Unfortunately, only the top portion (315° through 45° meridian angle) of the nozzle was visible with the camera; hence, the reader is cautioned that the determination of separation on the remainder of the nozzle is not absolute, but the trends are repeatable and consistent.

As the Reynolds number is increased the boundary layer becomes thinner. With a thinner turbulent boundary layer the flow will penetrate an adverse pressure gradient farther without separating. So by increasing Reynolds number the boundary layer is thinned and separation is delayed to a point farther downstream. Parts (c) of figures 13 to 16 show the changes in the pressure distributions at one meridian angle (180°) with changes in Reynolds number. As the separation is reduced more recompression is gained on the boattail resulting in lower drag.

The preceding discussion is an example of the typical attached flow-separated flow case. In addition to this, there appears to be a dynamic phenomena which is also affected by Reynolds number. Examination of the pressure data (some representative pressures are shown in appendix C) show some examples of obvious separation while in other regions the flow is obviously attached. However, the majority of data fall between these two. One possible course is that the flow oscillates between being attached and separated. The pressures measured are time-averaged so they reflect a combination of the two actual conditions. When this situation is present, the tufts on the boattail lay flat pointing in the streamwise direction, but they show movements or oscillations.

The oscillations become more severe at lower Reynolds numbers. At these lower Reynolds numbers the pressures become more like those in the obvious separation condition. At high Reynolds numbers the flow may be attached. As the Reynolds number is decreased this same flow becomes unsteady and begins to oscillate between the attached and separated conditions. As the Reynolds number is reduced further, the flow is in the separated mode more and more, until it eventually remains separated.

The two types of separation - the stably separated region, and the time-varying separation - usually are occurring simultaneously on different portions of the boattail, and each varies with changes in Reynolds number. The net result is a reduction in the boattail drag with increasing Reynolds number.

Angle-of-Attack Effect

The effect of angle-of-attack on boattail drag is shown in figure 17, at two different flight conditions, $M_0 = 0.6$ at an altitude of 9144 meters (30 000 ft) and $M_0 = 0.9$ at an altitude of 7620 meters (25 000 ft). At higher angles-of-attack (11° and above) there is a slight increase in boattail drag with increasing angle-of-attack. This is shown on figure 17(a) on all four nozzles tested. At lower angles-of-attack (9° to 10° and below) there is little or no effect of angle-of-attack (fig. 17(b)). Tests run in the Lewis 8- by 6-Foot Supersonic Wind Tunnel (ref. 7) on similar type nozzles mounted on a 1/20-scale F-106 showed similar trends with angle-of-attack. The wind tunnel data show no effect until an angle-of-attack of about 8.5°, beyond which there is an increase in drag. The wind tunnel data also show that this effect is more pronounced at high Mach numbers. Unpublished data from a more recent test with the 1/20-scale model and scaled versions of the same series of 24° boattail nozzles reported herein (but with jet boundary simulators), also showed the same trends.

Effect of Nozzle Geometry

The effect of radius ratio on the boattail drag is shown in figure 18. The pressure distributions from which the drag values were obtained are shown in appendix C. At Mach 0.60 (fig. 18(a)) nozzle 25 has relatively low drag because the flow generally remains attached except at low Reynolds numbers. The flow overexpands at the shoulder but begins recompressing immediately to a value greater than free stream. At Mach 0.6 there is little or no separation on nozzle 65. The overexpansion at the shoulder is not as great as on nozzle 25 because the turn is more gradual, but the recompression does not begin until much farther downstream on the boattail. In comparison to nozzle 25, nozzle 65 has a larger area of low pressure at the maximum overexpansion and has

lower pressures along the remainder of the boattail. Also, the area where the recompression begins is farther downstream than on nozzle 25. In comparison to nozzle 25, nozzle 65 is out of the favorable high-pressure region caused by the installation (ref. 1). This combination yields a higher drag on nozzle 65. Nozzle 100 is a complete circular arc boattail and has the least overexpansion at the shoulder. The recompression on the aft boattail is similar to nozzle 65, but the levels of the pressures are higher. The result is that the drag on nozzle 100 is always lower than the other two. The high drag on nozzle 65 is contrary to what would be expected from isolated data (ref. 10). Therefore, this effect may be due to the particular underwing installation.

At $M_0 = 0.9$ (fig. 18(b)) the boattail drag decreases with increasing radius ratio. On nozzles 25 and 65 there is some separation at all Reynolds numbers. Nozzle 25 with the smaller radius at the shoulder and sharper turn has more separation than either of the others. As discussed before, the separation reduces the recompression on the aft boattail and raises the drag. Nozzle 25 with the most separation has the highest drag; nozzle 65 with some separation has slightly lower drag; and nozzle 100 with little or no separation has the lowest drag.

Pressure Ratio Effect

Figure 19 shows the effect of nozzle pressure ratio P_8/p_0 on boattail drag. Figure 19(a) shows data at Mach 0.6 and an altitude of 4572 meters (15 000 ft). The design pressure ratio at station 9 (the nozzle exit) is $(P/p)_{9,isen} = 3.22$. For the data shown on these plots, the primary jet was overexpanded, since the nozzle pressure ratios P_8/p_0 were always below the design value. It has been shown (ref. 6), on nozzles similar to these, that boattail drag is relatively insensitive to small changes in pressure ratio for values below the design conditions. The off-design data shown here also indicate no effect of pressure ratio.

Figure 19(b) shows data at $M_0 = 0.9$ and at an altitude of 7620 meters (25 000 ft). The pressure ratio range extends from considerably below the design value up to and slightly above it. Below the design pressure ratio there is no effect; but just above the design value the drag begins to drop off as the high pressures feed back on the boattail. This has also been shown previously in the wind tunnel in reference 6.

Mach Number Effect

Two of the nozzles, 25Ex and 100, were tested over a Mach number range from 0.6 to 0.975 (see fig. 20). This was done in level flight at an altitude of 7620 meters (25 000 ft). As Mach number is increased, the drag drops off until approximately

Mach 0.8 on nozzle 25Ex and until a value between Mach 0.9 and 0.95 on nozzle 100. This favorable effect is a result of a terminal shock that moves back over the nacelle and, at a Mach number near 0.95, is just upstream of the nozzle assembly. As described in reference 1, the combination of the flow field of the wing and the flow field around the nacelle, which is reflected by the lower wing surface, amplifies the recompression of the flow through the shock and over the nozzle. When the shock passes off the nozzle there is an abrupt drop in boattail pressures and a corresponding rise in boattail drag. On nozzle 25Ex near Mach 0.8 the adverse effects of separation become large enough to offset the favorable effects of the wing flow and terminal shock. Beyond Mach 0.8 the separation increases and so does the drag. Nozzle 100 has very little separation until much higher Mach numbers are attained.

Figure 20(b) shows the effect of Mach number on nozzle performance. The particular performance parameter is a summation of forces yielding a thrust minus drag that is ratioed to the ideal thrust of the primary flow. The thrust minus drag portion includes internal gross thrust, friction drag, and boattail drag. The friction drag is a theoretical number and the internal gross thrust is a calculated value based on measured engine conditions.

Effect of Nozzle Axial Location

Nozzle 25 and nozzle 25Ex had identical geometries. The difference between the two was that nozzle 25Ex was moved aft 25.4 centimeters (10.0 in.) from the wing trailing edge. This was done by building this nozzle with a 25.4 centimeter (10.0 in.) cylindrical section ahead of the boattail shoulder (see figs. 5(a) and (b)). The drag levels for nozzle 25Ex are considerably greater than with nozzle 25 for all the data presented. The trends and effects of the various parameters investigated are all the same and only the absolute levels changed. When separation is present on nozzle 25, nozzle 25Ex always showed slightly more and although the trends of the pressure distributions were always the same, the levels on nozzle 25Ex were always lower. The change in the drag levels is a result of moving the boattail out of the region of the favorable effects from the wing and terminal shock discussed previously.

Separation-Pressure Distribution Correlation

One of the primary objectives of the test series was to determine the separation characteristics of these different nozzle geometries. Each of the nozzles was extensively instrumented with 90 static pressure taps, and it was hoped to use these pressure distributions to detect separated flow. In addition to the pressure taps, tufts were

mounted on the nozzle and in-flight pictures were taken with a camera in the tail. The camera viewing area, however, was limited to the upper quadrant of the nozzle.

Two theoretical pressure distributions are shown in figure 21, which are typical of the pressures on these nozzles. There is a sharp overexpansion at the shoulder, and then, if the flow remains attached, a recompression occurs along the remainder of the boattail. If the flow separates, it is downstream of the shoulder so there is still an overexpansion at the shoulder and a recompression until the point of separation. Aft of the separation point there is little further recompression. The pressure distributions of the 0° and 30° meridian angle rows in figure 22 are examples of attached flow and the 300° and 330° meridian angle rows are examples of separated flow. The tuft picture on figure 22 confirms this: the outer tufts (15° and 45°) lay flat and steady, the inner tufts (315° and 345°) flop in all directions randomly.

The majority of data taken on these tests, however, did not yield pressure plots that indicated obvious separation or attached flow, as on the previous example. In figure 23 the tufts indicate that the flow over the 45° row is attached, the 15° row is attached until a point near the second or aft tuft, and the other two rows are separated. Knowing the results from the tuft movies, the pressure plots in figure 23 are reasonable, but with just the pressure distributions alone the results are not obvious.

The pressure curves in figure 24 are all very similar and almost parallel. The pictures indicate separation on the last three tufts of the 15° and 45° rows and attached flow on the others. With this information differences in the pressure curves can be found to correlate with the separated and attached regions, but these differences are very small. Figure 25 shows an example where the tufts indicate that the flow is attached on all four rows, but the differences in the pressure curves are larger than the differences seen in figure 24. Figure 26 is an example where the tufts show the flow to be separated on some portion of all four rows. However, the variations in the pressure curves are similar to those in figure 23 where two of the rows have attached flow. The tuft picture in figure 27 is an example of a flow that remains attached except for a small portion on the 315° and 345° rows. The pressure curve on the 300° row does show a small change in slope but the 330° row does not.

These examples show that the presence of a separated flow can not always be detected from the pressure distributions alone. If the pressure curves are at the extremes, similar to the ones shown in figure 21, the flow characteristics are obvious. However, the majority of data recorded on these tests fell somewhere between the two extremes. One possible explanation for this is that the flow is unsteady and oscillates attaching then separating, then reattaching, etc. The pressure measurements are time-averaged so, if this oscillation is occurring, the resulting pressure plots would be somewhere between the two extreme conditions. On many of the test points the tufts were laying flat in the streamwise direction, but were unsteady; oscillating at approximately 30 to 40 hertz.

SUMMARY OF RESULTS

Four variations of boattail nozzles were tested installed just below and aft of the wing trailing edge on an F-106B aircraft at subsonic speeds. The nozzles simulated nonafterburning configurations appropriate for turbofan powered aircraft with supersonic dash capability. The effects on boattail drag of Reynolds number, angle-of-attack, nozzle pressure ratio, and nozzle geometry were investigated. The following results were obtained:

1. Increasing the Reynolds number, by reducing altitude (changing density and viscosity), significantly reduced the boattail drag on all the nozzles at both Mach 0.6 and 0.9.

2. At lower aircraft angle-of-attack (9° to 10° and below) there was little effect of angle-of-attack on boattail drag. At lower speeds and higher angles there was an increase in drag coefficient with increasing angle-of-attack.

3. Increasing nozzle pressure ratio up to the design value (3.2) had little effect on boattail drag coefficient. Increasing pressure ratio above this value (up to 3.8) began to show favorable effects by reducing boattail drag.

4. At Mach 0.9 increasing radius ratio r/r_c decreased the boattail drag. At Mach 0.6 for this particular installation, increasing radius ratio first produced a slight increase and then a decrease in boattail drag coefficient.

5. Moving the shortest nozzle further aft, away from the favorable influence of the wing flow, significantly increased the boattail drag coefficient. But the same trends were observed for variations in major variables such as the Reynolds number.

6. The presence of a separated flow can not always be determined from steady-state pressure distributions alone, in the event that the flow separation is unsteady.

Lewis Research Center,
National Aeronautics and Space Administration,
Cleveland, Ohio, April 20, 1972,
764-74.

APPENDIX A

SYMBOLS

A^*	J-85 primary throat area (variable nozzle-locked, cold), 709.68 cm^2 (110.00 $in.^2$)
A_{E8}	nozzle effective throat area (hot), cm^2 ($in.^2$)
A_e	nozzle exit area, 791.73 cm^2 (122.72 $in.^2$)
A_{max}	maximum cross-sectional area, 3167.12 cm^2 (490.87 $in.^2$)
C_D	drag coefficient, $D/q_0 A_{max}$
C_p	pressure coefficient, $p-p_0/q_0$
D	drag, N (lb)
d	diameter, cm (in.)
F	nozzle gross thrust, N (lb)
$F_{i,p}$	isentropic primary thrust, N (lb)
$(F-D)/F_{i,p}$	nozzle performance
h	altitude, m (ft)
L	characteristic length, 5.18 m (17.00 ft)
l	nozzle length, cm (in.)
M	Mach number
P	total pressure, N/m^2 abs (psia)
p	static pressure, N/m^2 abs (psia)
q	dynamic pressure, N/m^2 abs (psia)
Re	Reynolds number, $\rho vL/\mu$
r	radius, cm (in.)
r_c	radius of complete circular arc boattail with exit to nacelle area ratio = 0.25 and a 24^o boattail angle, 183.52 cm (72.25 in.)
S	axial distance from nacelle station 530.63 (208.91) to nozzle exit, cm (in.)
v	velocity, m/sec (ft/sec)
x	axial distance from boattail shoulder, nacelle station 530.63 (208.91), cm (in.)

Z	axial distance from nacelle station 530.63 (208.91) to point where boattail contour becomes conic section, cm (in.)
α	angle-of-attack, deg
δ	elevon deflection, deg
ρ	density, kg/m^3 ($slug/ft^3$)
μ	coefficient of viscosity, $N\text{-}sec/m^2$ ($slug/ft\text{-}sec$)
ω	ratio of secondary to primary weight flow
$\omega\sqrt{\tau}$	corrected secondary weight flow
τ	ratio of secondary to primary total temperature

Subscripts:

B	boattail
c	circular arc
e	exit
isen	isentropic
0	free stream
8	primary nozzle throat station
9	nozzle exit station

APPENDIX B

WING FLOW

A brief study was made of the airflow over the delta wing on the F-106. This was done to determine whether disturbances from the wing affect the flow over the nozzle, particularly at high angles-of-attack. The modified F-106 had not been flown at these high angles previously.

A wind tunnel and flight wing flow study was done by the British on a delta wing aircraft similar to the F-106 (ref. 11). The wing flow patterns of the two are very similar. Figure 28, extracted from reference 11, shows a diagram of the general flow pattern over a delta wing. At subsonic speeds separation occurs on the leading edge near the wing tip. This creates a vortex sheet that rolls up above the wing (fig. 28) producing a spanwise flow beneath it. The flow not directly entrained by the vortex, passes over the top and reattaches to the wing surface. The end result is three major areas of differing flow: region A, separated flow; region B, spanwise flow parallel to the leading edge; and region C, chordwise flow. As angle-of-attack is increased the vortex moves inboard, influencing a greater portion of the flow over the top of the wing.

On the F-106, if the reattachment line (the line dividing the spanwise flow and the chordwise flow, fig. 28) moves inboard far enough, the vortex sheet would disturb the flow over the test nozzle. Tufts were mounted on the left wing upper surface and elevon (fig. 29) and pictures taken with the camera mounted in the tail (fig. 9). Figure 30 shows two examples of the wing tuft pictures. Figure 31 is a diagram of the observed wing flow at one of these conditions. As can be seen the reattachment line moves inboard a considerable distance; however, the wing flow vortex does not directly influence the flow over the nozzle. The tufts on the elevon just upstream of the nozzle always lay flat and steady in the chordwise direction.

APPENDIX C

PRESSURE DISTRIBUTIONS

Figures 32 to 43 are examples of the actual pressure distributions recorded; they are adjusted for the correction previously discussed in the Data Reduction section. Figures 32 to 35 show the pressures on each nozzle over a range of Reynolds numbers at $M_0 = 0.6$; figures 36 to 39 are the same at $M_0 = 0.9$. Figures 40 to 43 show the pressures over a range of angle-of-attack from 11^o to 14^o at $M_0 = 0.6$ and at an altitude of 9144 meters (30 000 ft).

REFERENCES

1. Wilcox, Fred A.; Samanich, Nick E.; and Blaha, Bernard J.: Flight and Wind Tunnel Investigation of Installation Effects on Supersonic Cruise Exhaust Nozzles at Transonic Speeds. Paper 69-427, AIAA, June 1969.

2. Crabs, Clifford C.; Mikkelson, Daniel C.; and Boyer, Earle O.: An Inflight Investigation of Airframe Effects on Propulsion System Performance at Transonic Speeds. Presented at the 13th Annual Symposium of the Society of Experimental Test Pilots, Los Angeles, Calif., Sept. 25-27, 1969.

3. Mikkelson, Daniel C.; and Head, Verlon L.: Flight Investigation of Airframe Installation Effects on a Variable Flap Ejector Nozzle of an Underwing Engine Nacelle at Mach Numbers from 0.5 to 1.3. NASA TM X-2010, 1970.

4. Groth, Harold W.; Samanich, Nick E.; and Blumenthal, Philip Z.: Inflight Thrust Measuring System for Underwing Nacelles Installed on a Modified F-106 Aircraft. NASA TM X-2356, 1971.

5. Harrington, Douglas E.: Effect of a Rectangular Simulated Wing on the Pressure-Drag Coefficient of Various Boattails at Mach Numbers from 0.60 to 1.47. NASA TM X-52609, 1969.

6. Harrington, Douglas E.: Jet Effects on Boattail Pressure Drag of Isolated Ejector Nozzles at Mach Numbers From 0.60 to 1.47. NASA TM X-1785, 1969.

7. Blaha, Bernard J.: Effect of Underwing Engine Nacelle Shape and Location on Boattail Drag and Wing Pressures at Mach Numbers From 0.56 to 1.46. NASA TM X-1979, 1970.

8. Antl, Robert J.; and Burley, Richard R.: Steady-State Airflow and Afterburning Performance Characteristics of Four J85-GE-13 Turbojet Engines. NASA TM X-1742, 1969.

9. Groth, Harold W.: Nozzle Performance Measurement on Underwing Nacelles of an F-106 Utilizing Calibrated Engines and Load Cells. Paper 71-681, AIAA, June 1971.

10. Schrewsbury, George D.: Effect of Boattail Juncture Shape on Pressure Drag Coefficients of Isolated Afterbodies. NASA TM X-1517, 1968.

11. Dee, F. W.; and Nicholas, O. P.: Flight Determination of Wing Flow Patterns and Buffet Boundaries for the Fairey Delta 2 Aircraft at Mach Numbers Between 0.4 and 1.3, and Comparison With Wind Tunnel Results. Rep. R&M-3482, Aeronautical Research Council, 1967.

TABLE I. - FLIGHT AND ENGINE TEST VARIABLES

Altitude, h		Flight Mach number, M_0					
m	ft	0.6			0.9		
		Angle of attack, α, deg	Nominal Reynolds number, Re	Load factor	Angle of attack, α, deg	Nominal Reynolds number, Re	Load factor
3 048	10 000	11, 13	5.44×10^7	2.4, 3.0	-------	--------	---------
4 572	15 000	↓	4.74	2.0, 2.5	6	7.10×10^7	2.3
6 096	20 000	↓	4.08	1.6, 2.0	6	6.08	1.9
7 620	25 000	↓	3.46	1.3, 1.6	4.5→9	5.19	1.1→2.6
9 144	30 000	11→14	2.89	1.1→1.4	6, 9	4.39	1.2, 2.1
10 668	35 000	-------	--------	---------	6, 9	3.69	1.2, 1.7
12 192	40 000	-------	--------	---------	9	2.94	1.3
13 716	45 000	-------	--------	---------	9	2.31	1.0

Nozzle pressure ratio variation, P_8/p_0:

At $M_0 = 0.6$ and h = 4572 m (15 000 ft) . . . . . 2.2→2.9

At $M_0 = 0.9$ and h = 7620 m (25 000 ft) . . . . . 2.6→3.8

Level flight Mach number variation at h = 7620 m (25 000 ft)

(nozzles 25Ex and 100 only) . . . . . 0.6→0.98

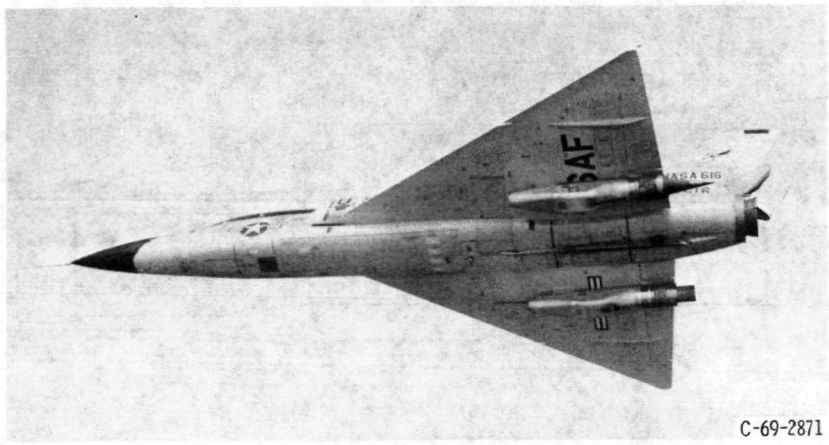

Figure 1. - Modified F-106B in flight.

Figure 2. - Boattail nozzles installed on F-106B aircraft.

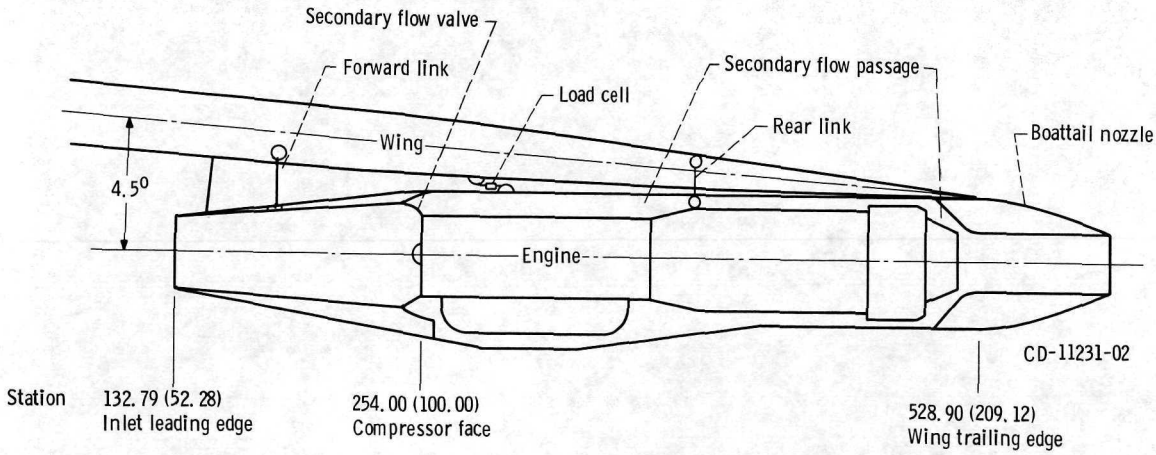

Figure 3. - Schematic of nozzle installation (all dimensions are in cm (in.)).

Figure 4. - Nacelle installation.

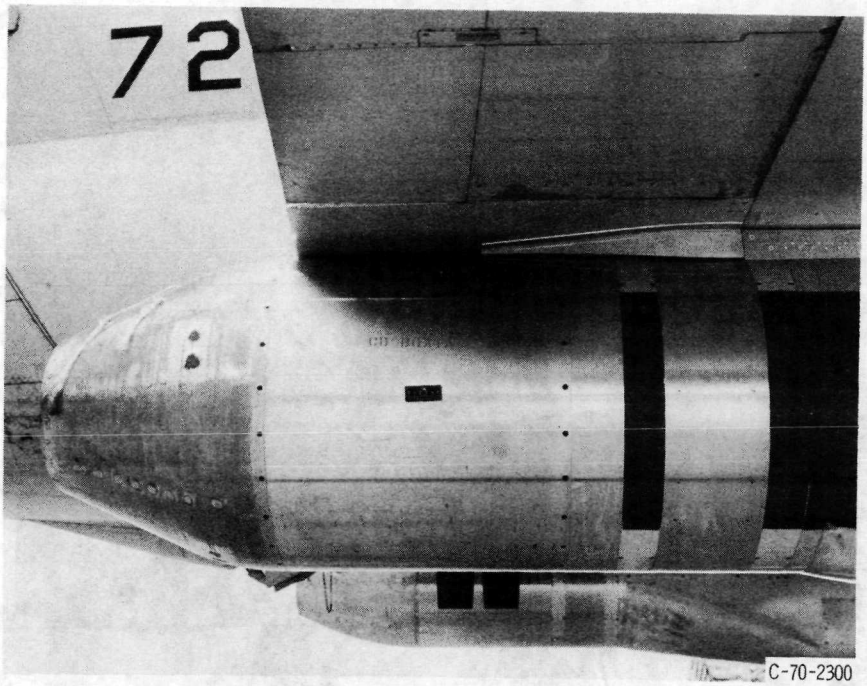

(a) Nozzle 25; radius ratio, 0.25.

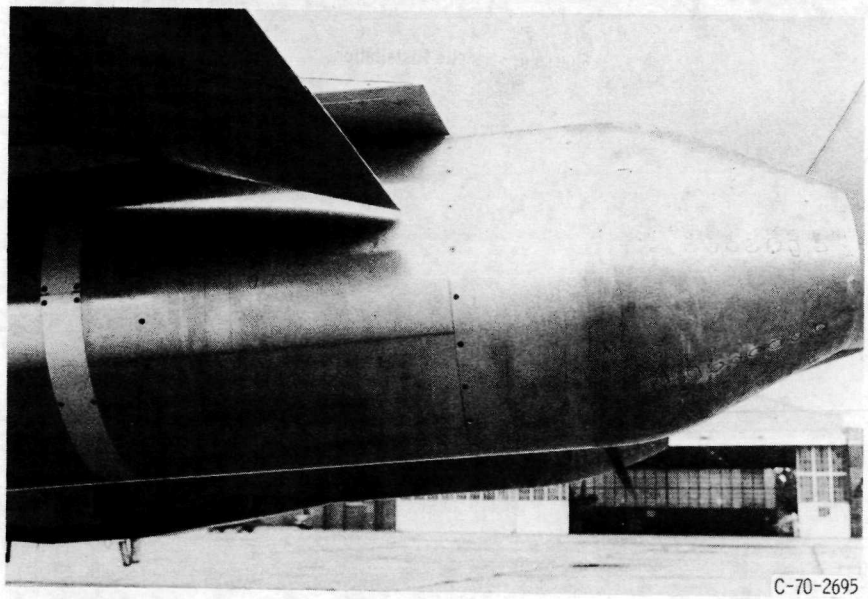

(b) Nozzle 25Ex; radius ratio, 0.25.

Figure 5. - Boattail nozzles.

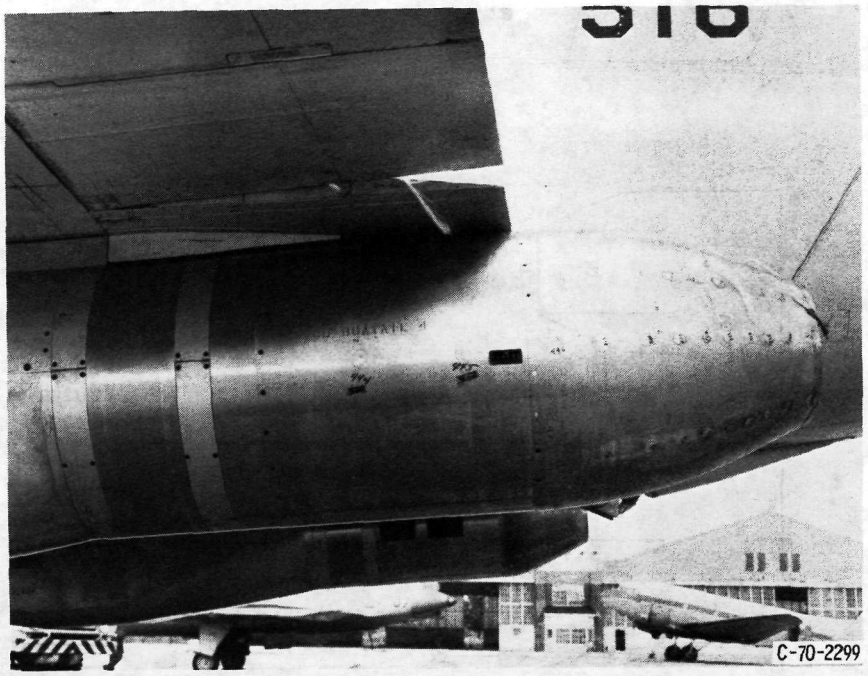

(c) Nozzle 65; radius ratio, 0.65.

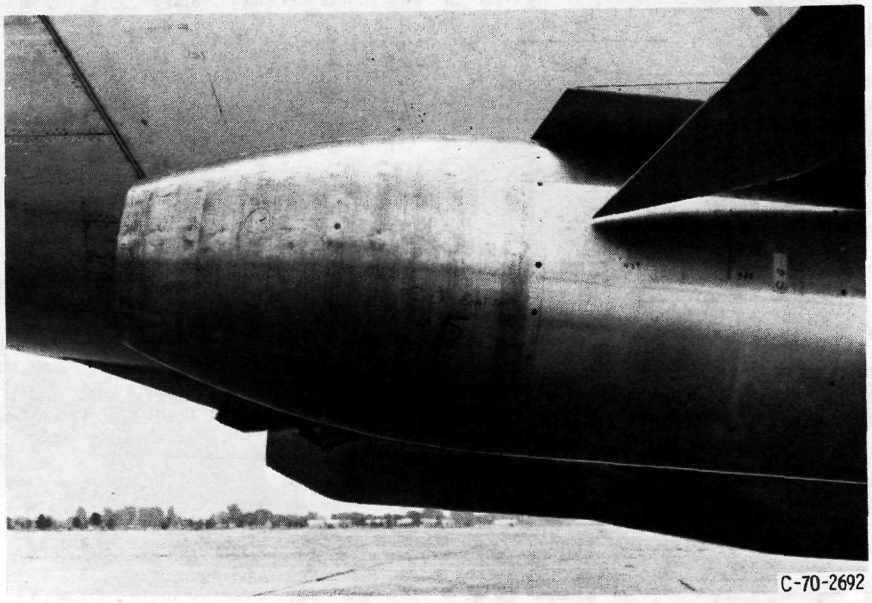

(d) Nozzle 100; radius ratio, 1.00.

Figure 5. - Concluded.

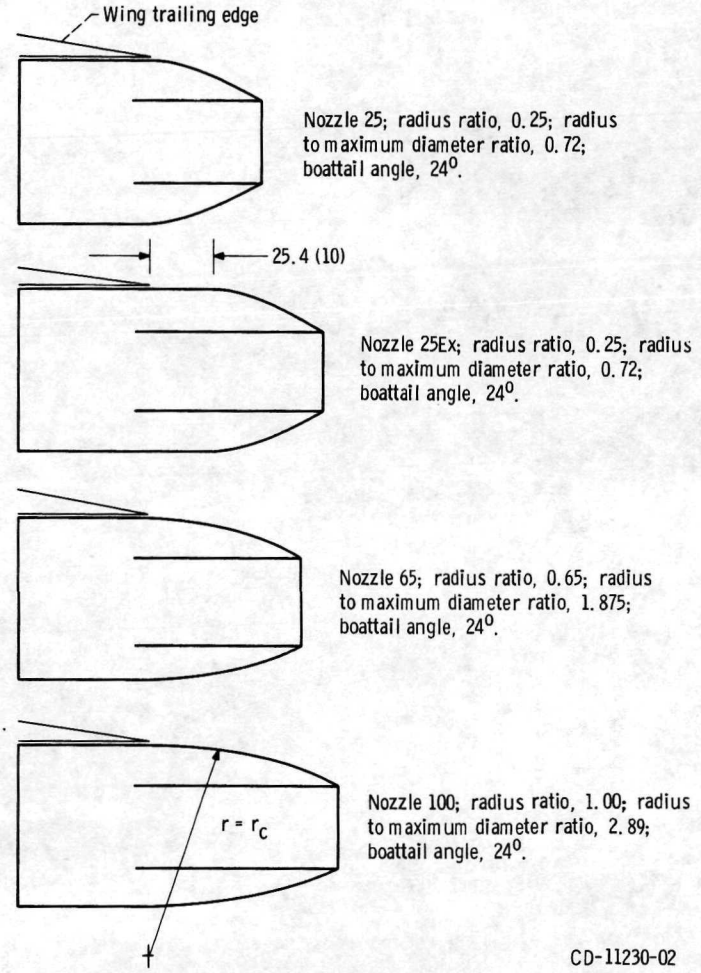

Figure 6. - Radius ratios and boattail angles (all dimensions are in cm (in.)).

Nozzle	S	r	Z
25	45.42 (17.88)	45.87 (18.06)	18.67 (7.35)
25Ex	70.82 (27.88)	45.87 (18.06)	44.07 (17.35)
65	61.01 (24.02)	119.28 (46.96)	48.51 (19.10)
100	74.65 (29.39)	183.52 (72.25)	74.65 (29.39)

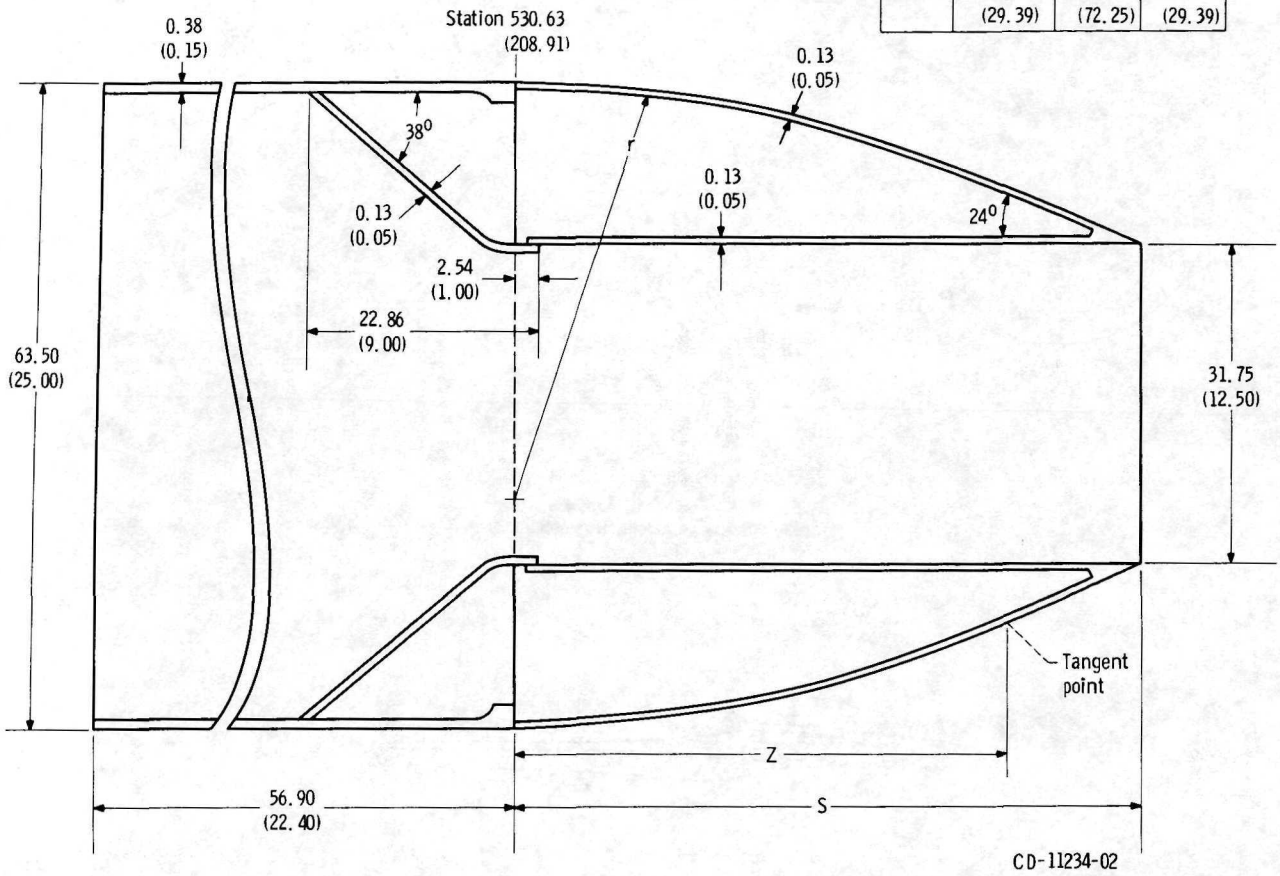

Figure 7. - Boattail nozzle dimensions (all dimensions are in cm (in.)).

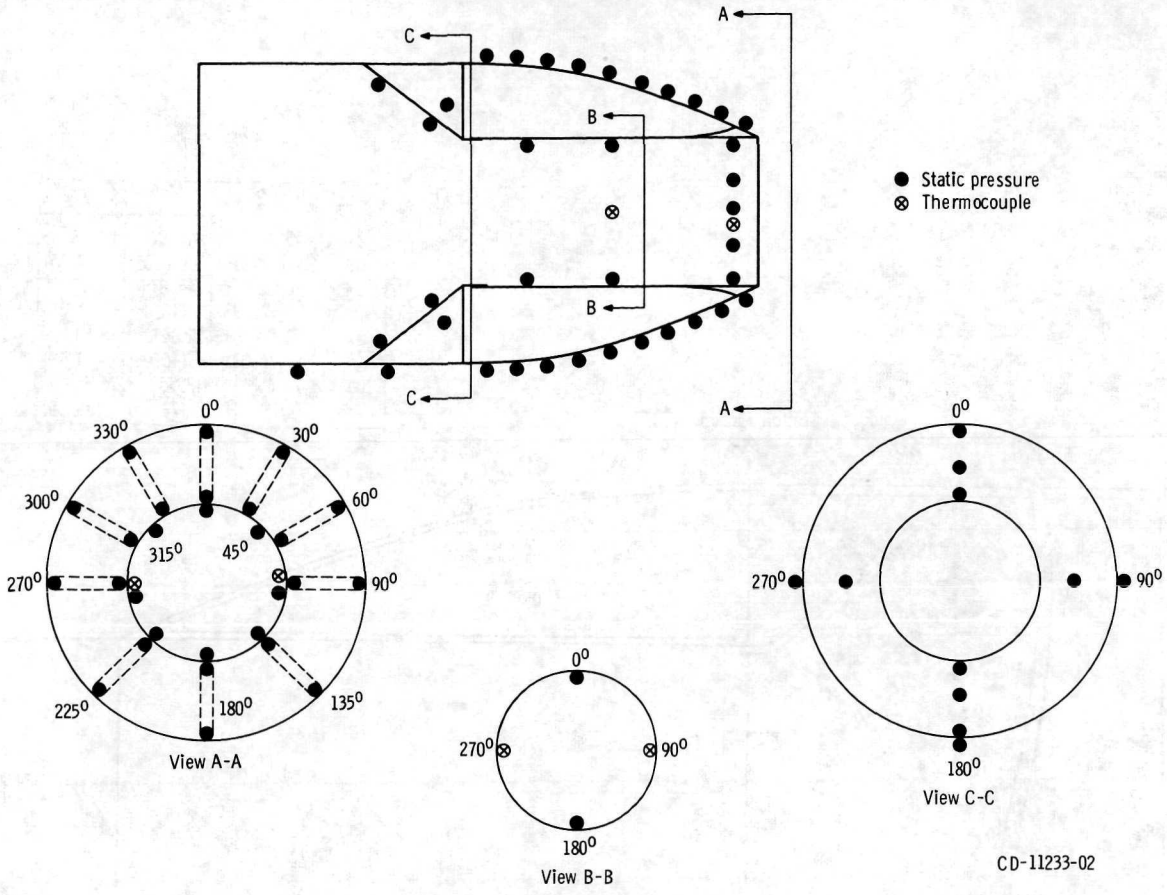

Figure 8. - Boattail nozzle instrumentation.

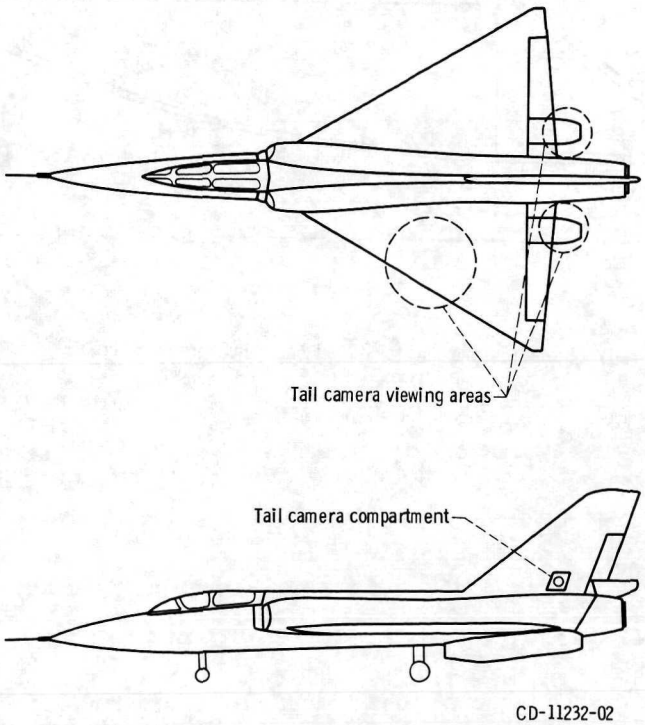

Figure 9. - Tail camera installation.

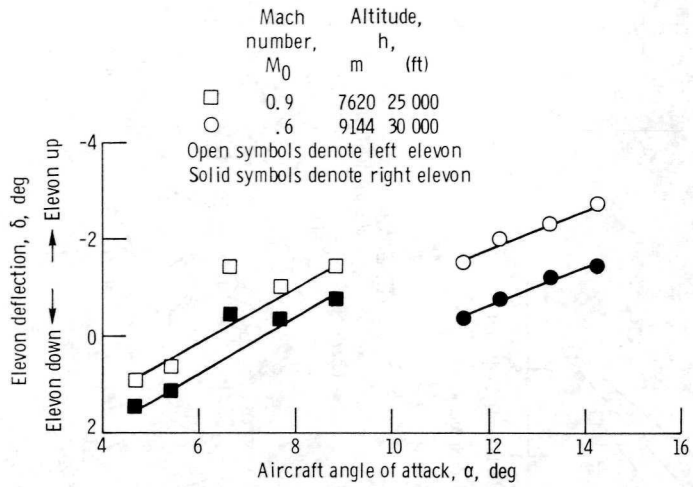

Figure 10. - Elevon deflections in angle-of-attack maneuvers.

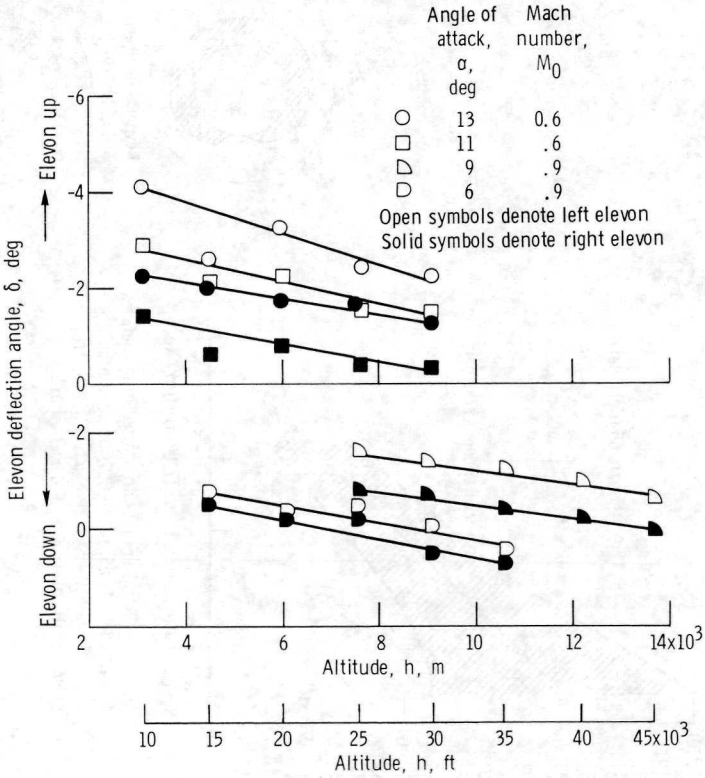

Figure 11. - Elevon deflections with altitude variation.

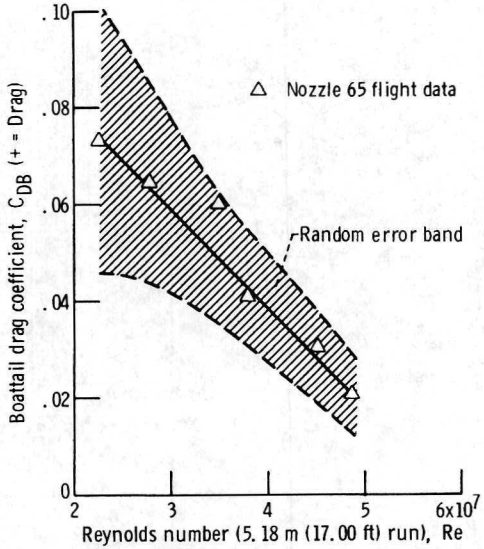

Figure 12. - Random error in boattail drag coefficient. Nozzle 65; Mach 0.9; angle of attack, 9°; 1-sigma deviations in Mach number, free-stream static pressure, and boattail pressure.

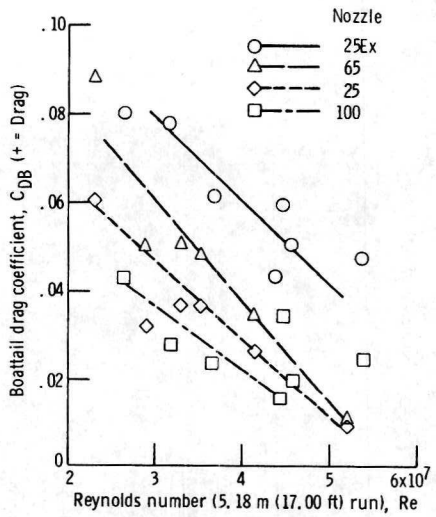

(a) Boattail drag coefficient.

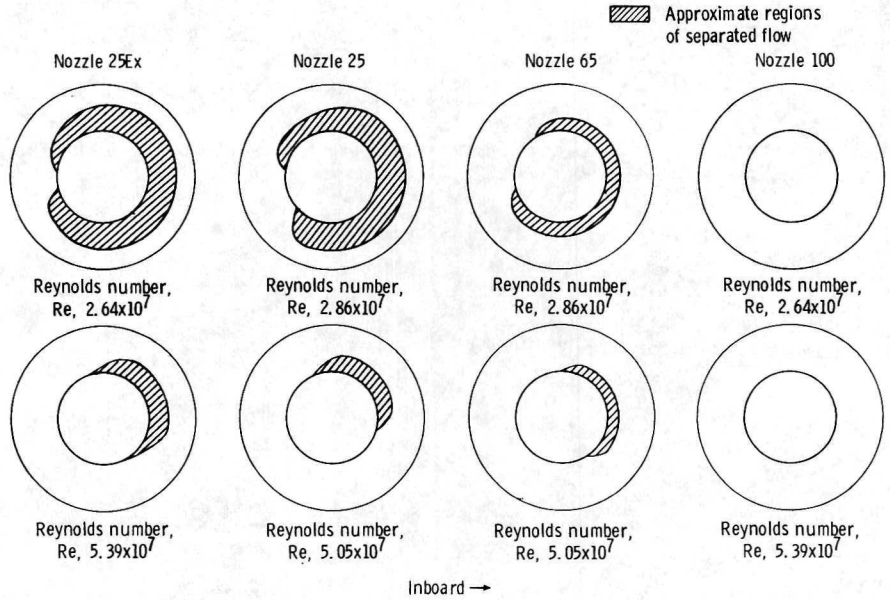

(b) Separation.

Figure 13. - Reynolds number effect on boattail drag, separation characteristics, and pressure distributions. Mach 0.6; angle of attack, 13°.

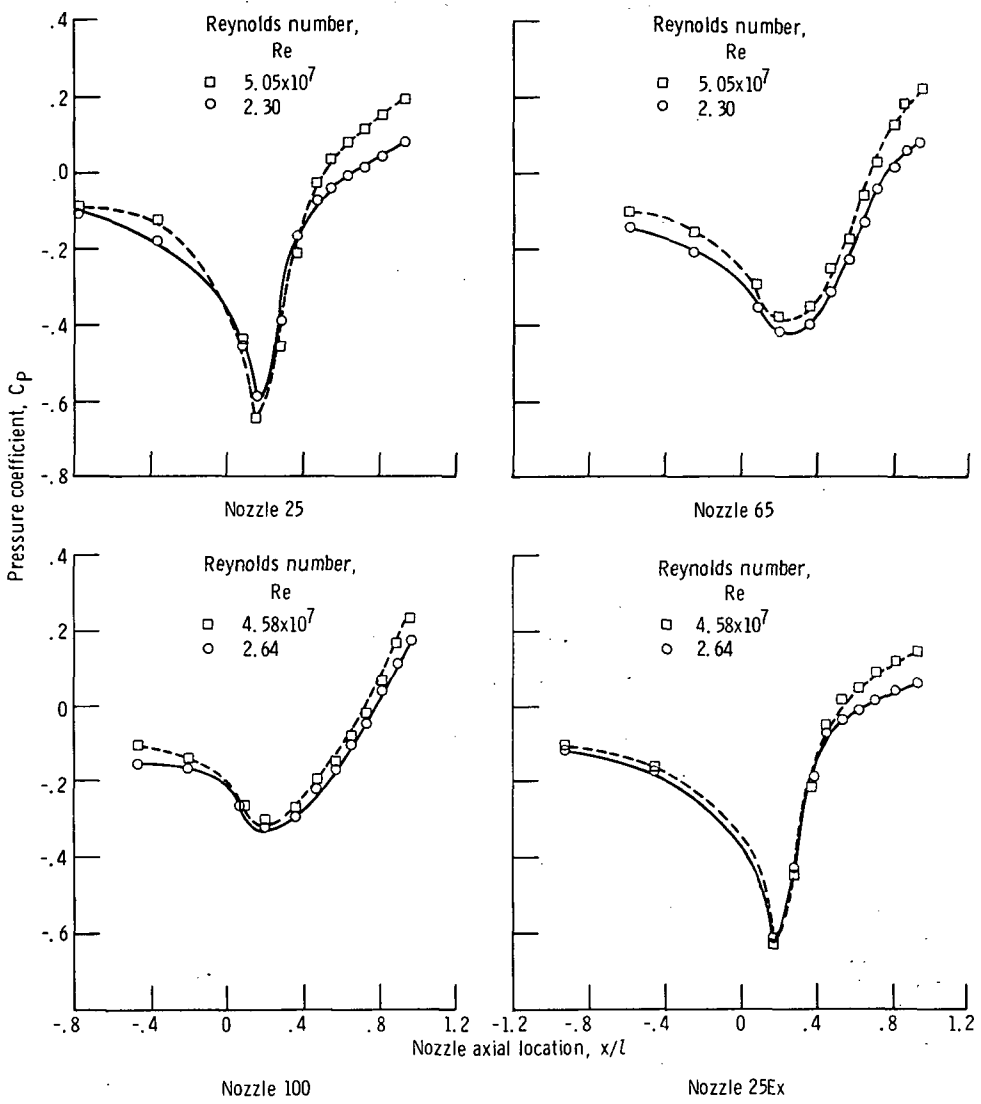

(c) Pressure distribution comparisons; meridian angle, 180°.

Figure 13. - Concluded.

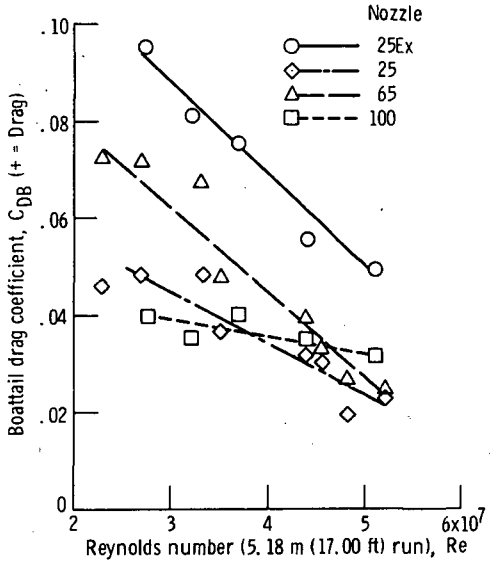

(a) Boattail drag coefficient.

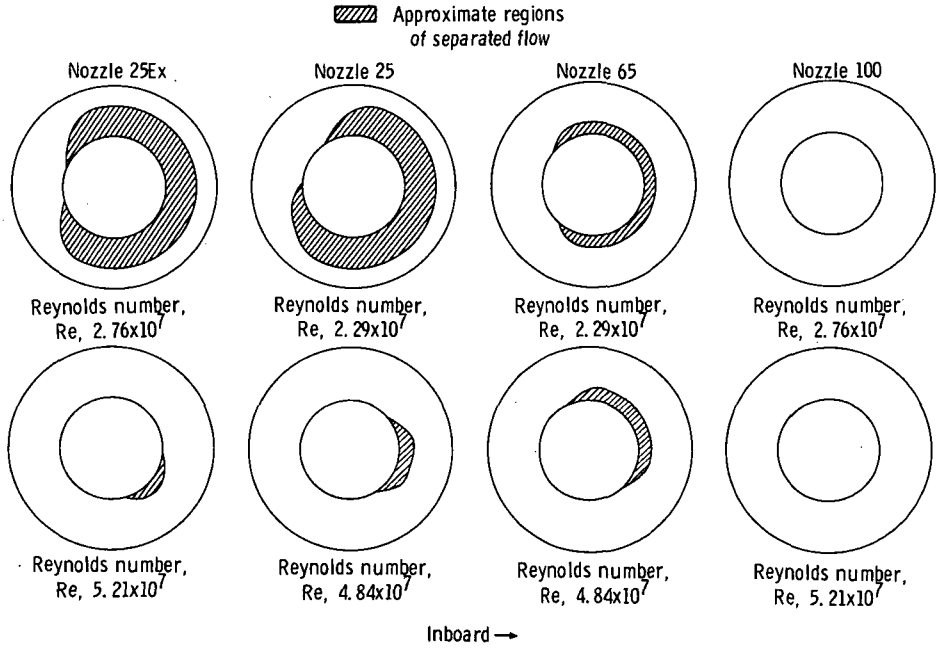

(b) Separation.

Figure 14. - Reynolds number effect on boattail drag, separation characteristics, and pressure distributions Mach 0.6; angle of attack, 11^{0}.

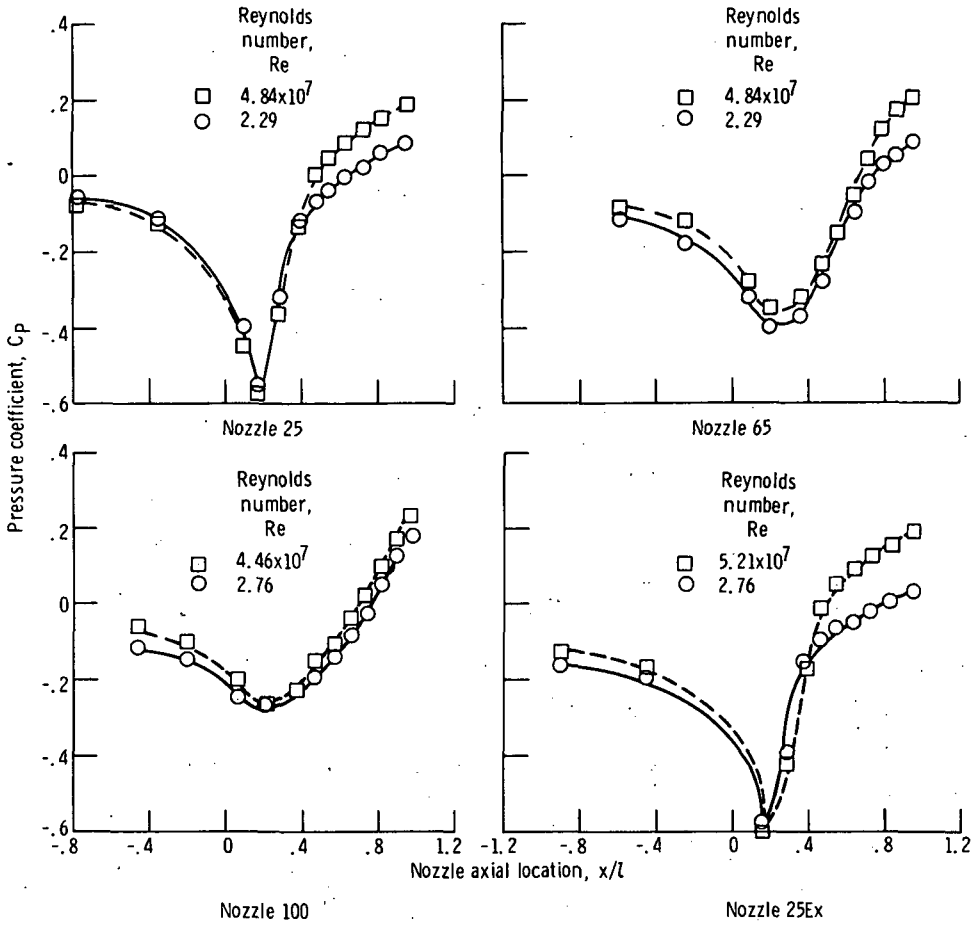

(c) Pressure distribution comparisons; meridian angle, 180°.

Figure 14. - Concluded.

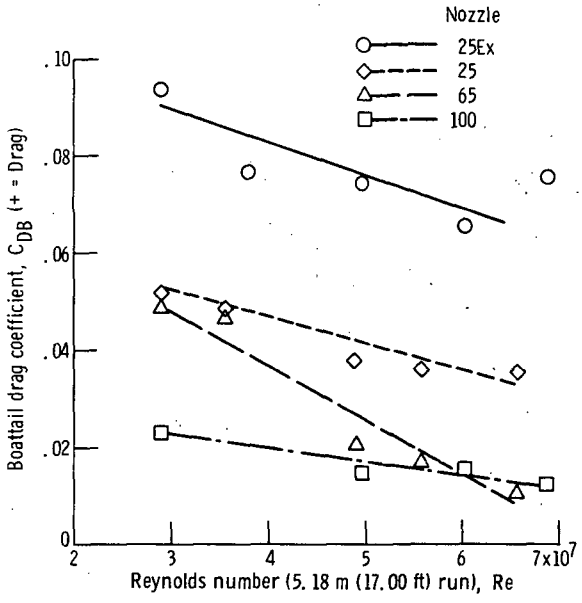

(a) Boattail drag coefficient.

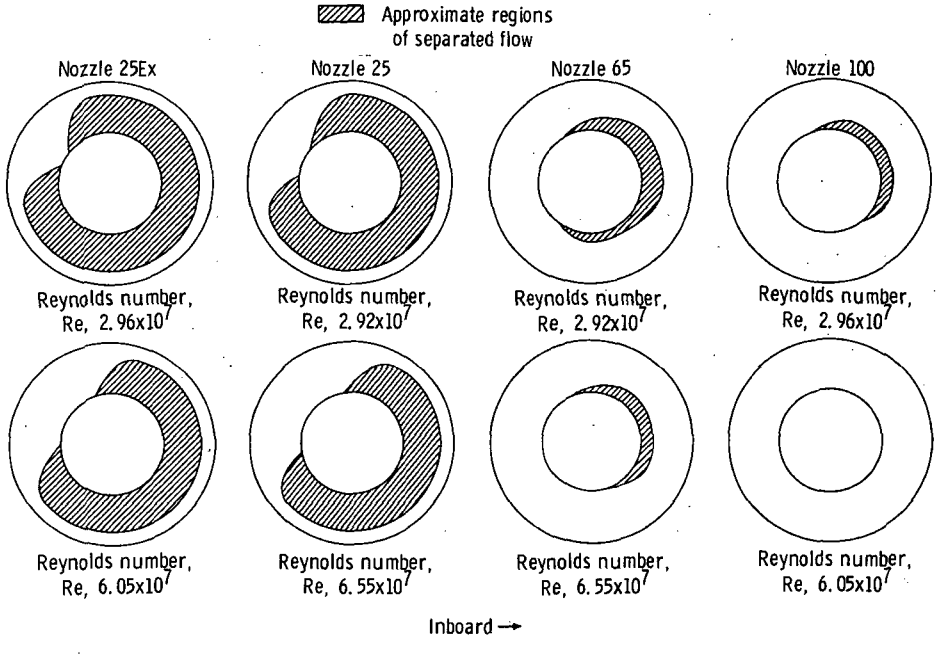

(b) Separation.

Figure 15. - Reynolds number effect on boattail drag, separation characteristics, and pressure distribution. Mach 0.9; angle of attack, 6^{0}.

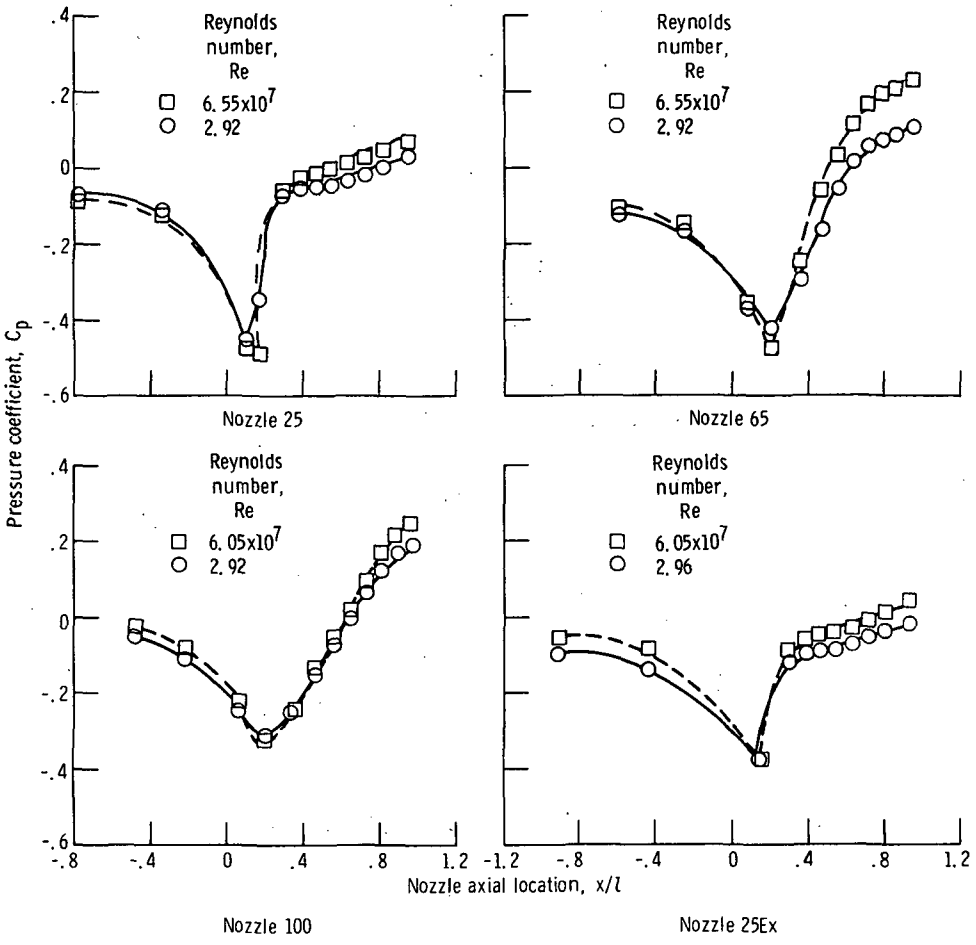

(c) Pressure distribution comparisons; meridian angle, 180^0.

Figure 15. - Concluded.

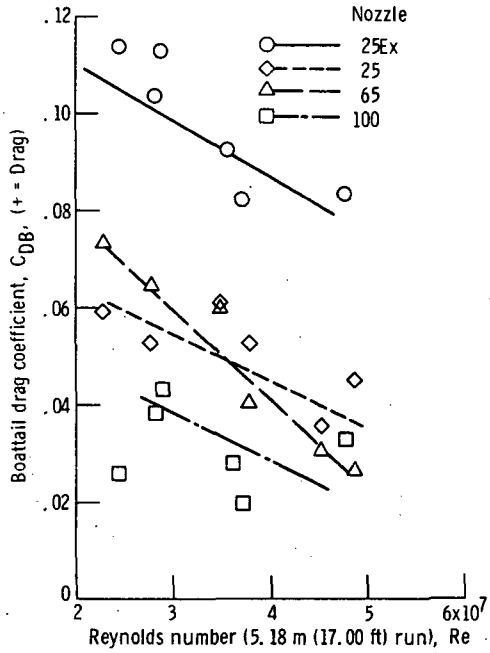

(a) Boattail drag coefficient.

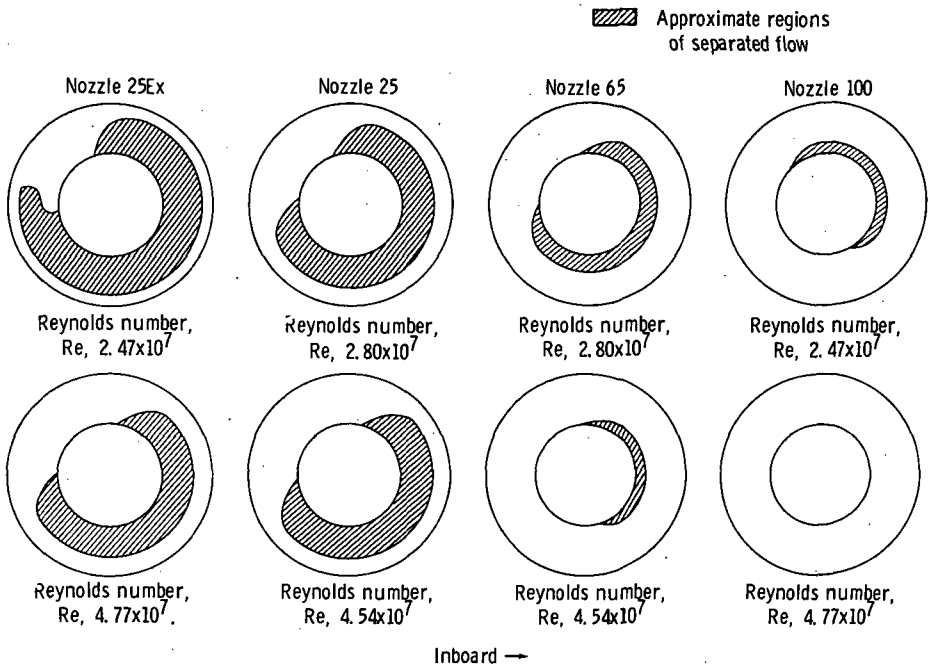

(b) Separation.

Figure 16. - Reynolds number effect on boattail drag, separation characteristics, and pressure distributions. Mach 0.9; angle of attack, 9°.

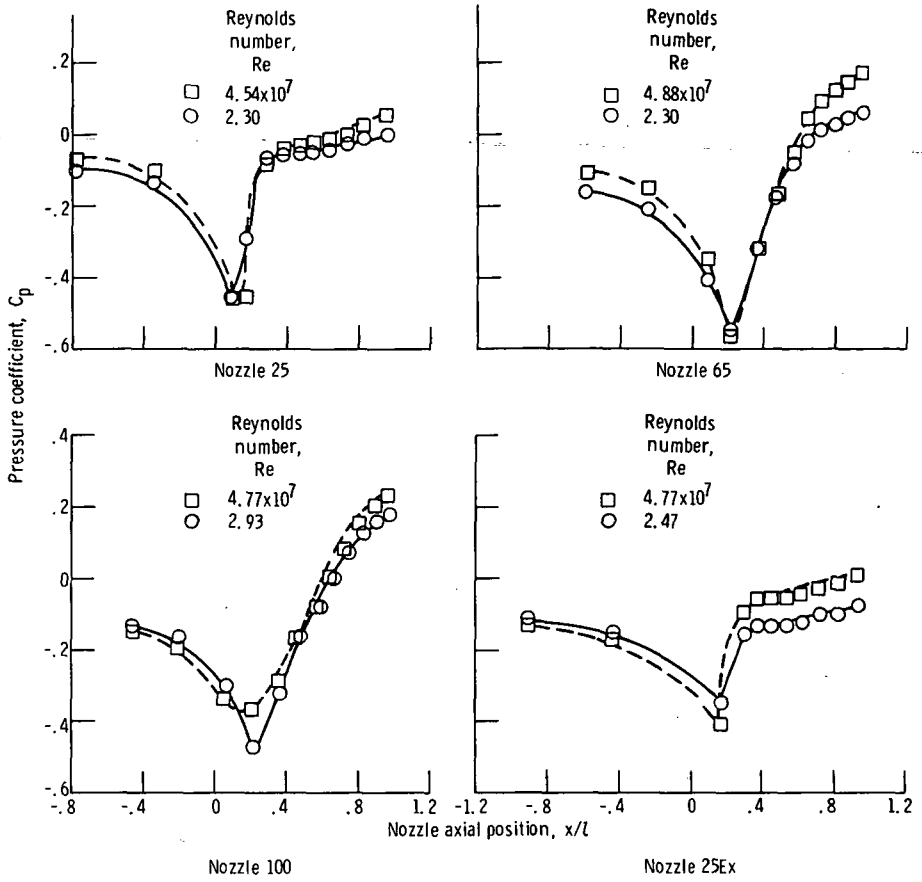

(c) Pressure distribution comparisons; meridian angle, 180^0.

Figure 16. - Concluded.

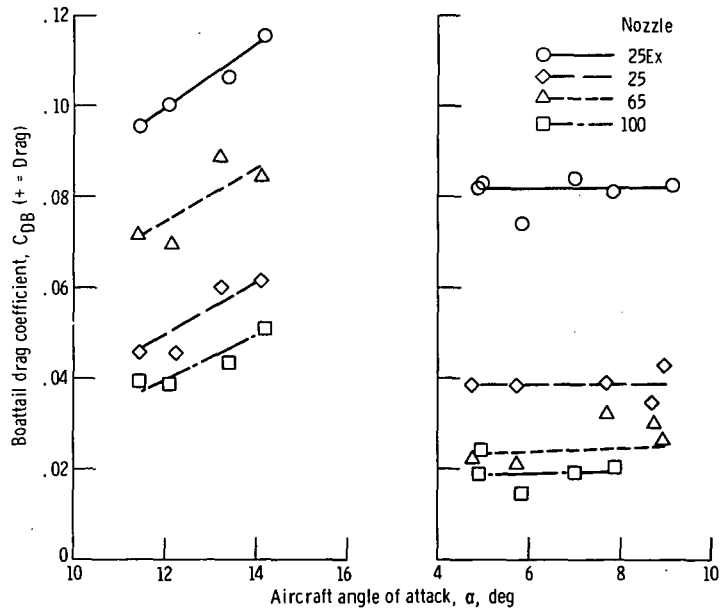

(a) Mach 0.6; altitude, 9144 meters (30 000 ft); Reynolds number (5.18 m (17.00 ft)), 2.5×10^7.

(b) Mach 0.9; altitude 7620 meters (25 000 ft); Reynolds number (5.18 m (17.00 ft)), 4.80×10^7.

Figure 17. - Angle of attack effects on boattail drag coefficient.

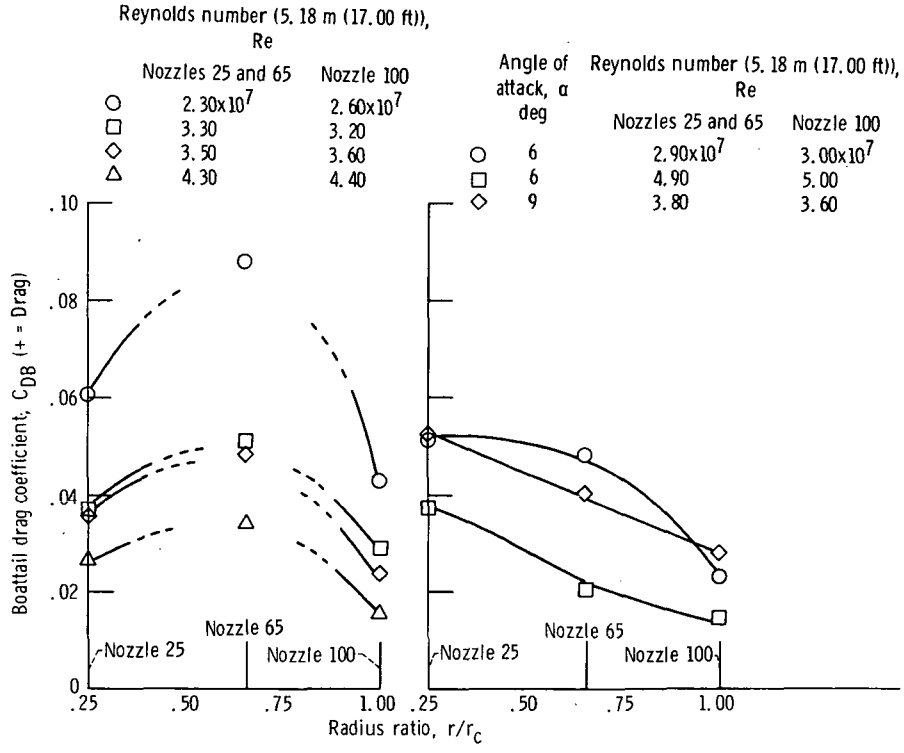

(a) Mach 0.6; angle of attack, 13^0. (b) Mach 0.9.

Figure 18. - Radius ratio effect on boattail drag coefficient.

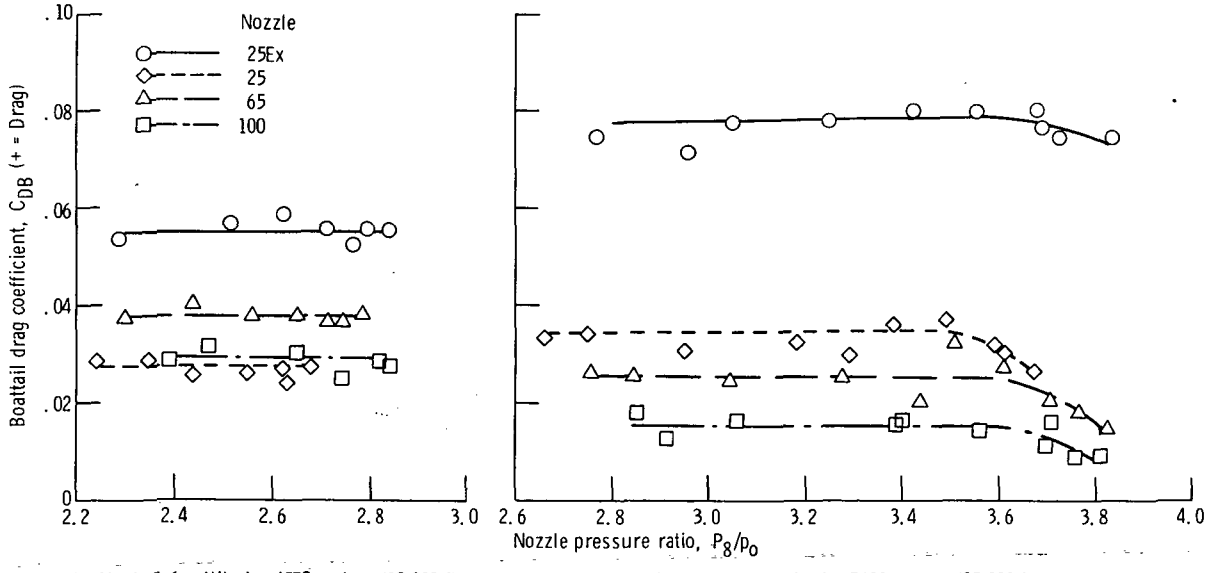

(a) Mach 0.6; altitude, 4572 meters (15 000 ft). (b) Mach 0.9; altitude, 7620 meters (25 000 ft).

Figure 19. - Nozzle pressure ratio effects on boattail drag coefficient. Nozzle exit area ratio, A_e/A^*, 1.12; nozzle exit isentropic pressure ratio, $(p/P)_{9,\,isen}$, 0.31.

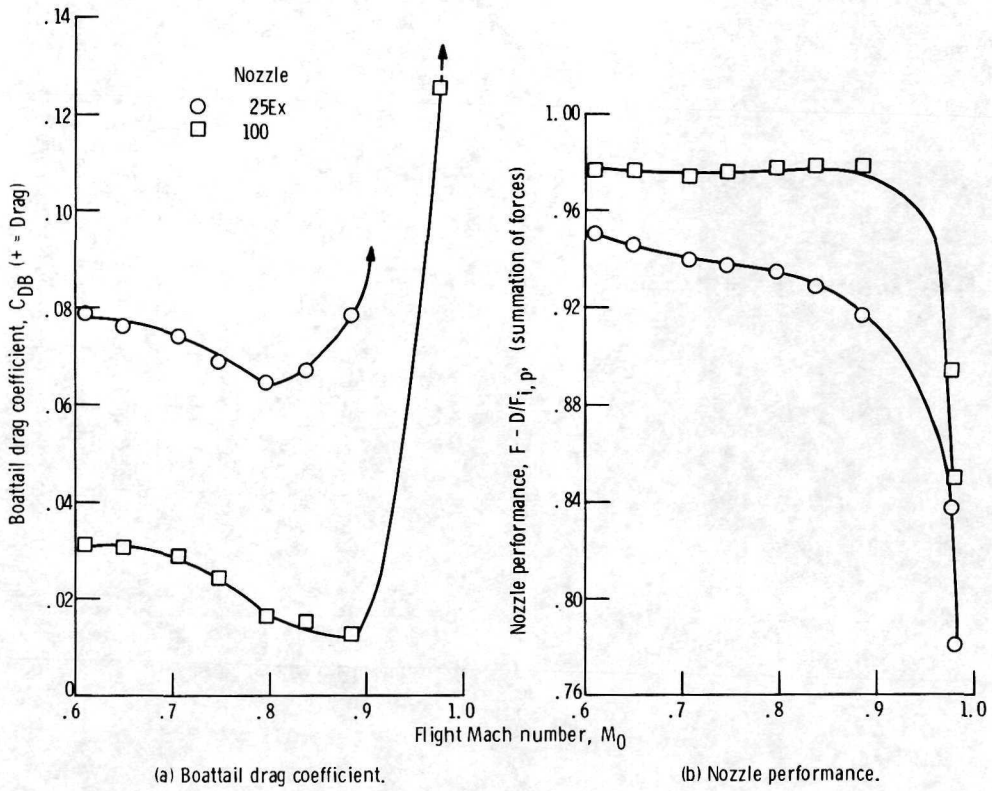

(a) Boattail drag coefficient.

(b) Nozzle performance.

Figure 20. - Mach number effects on boattail drag and nozzle performance. Level flight altitude, 7620 meters (25 000 ft).

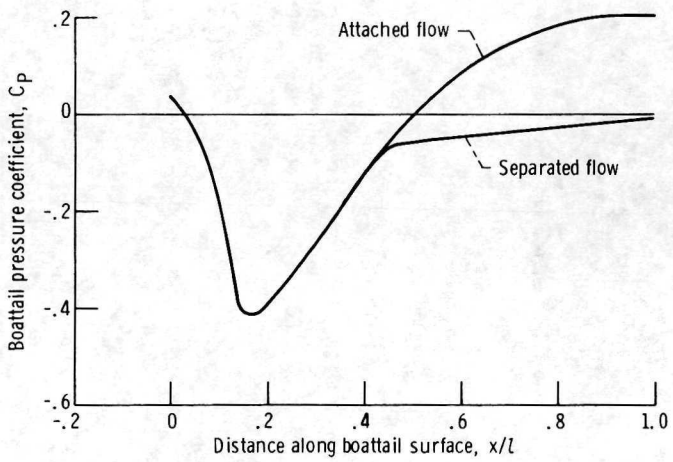

Figure 21. - Typical pressure distribution.

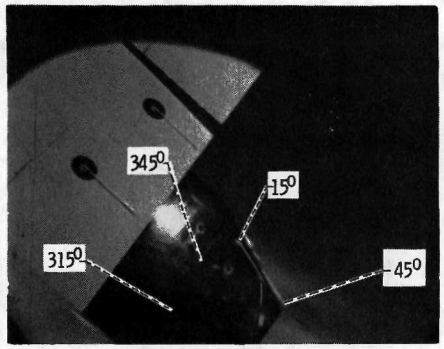

(a) Tuft picture.

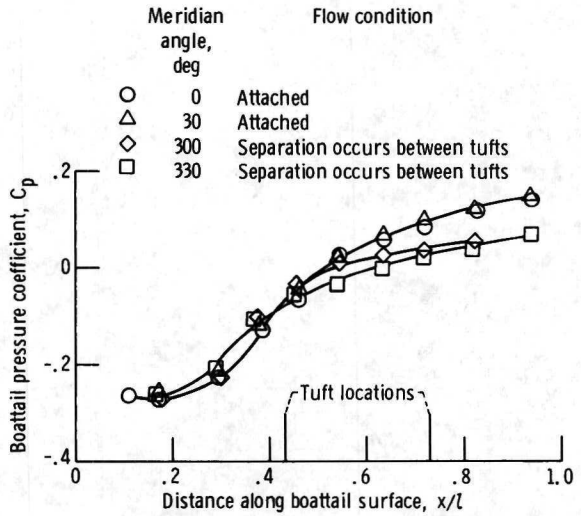

(b) Boattail pressure distribution.

Figure 22. - Separation-pressure correlation. Mach 0.6; altitude, 7620 meters (25 000 ft); Reynolds number, 3.34×10^7; angle of attack, 11^0; nozzle 25.

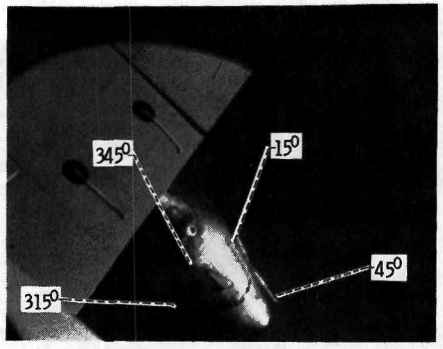

(a) Tuft picture.

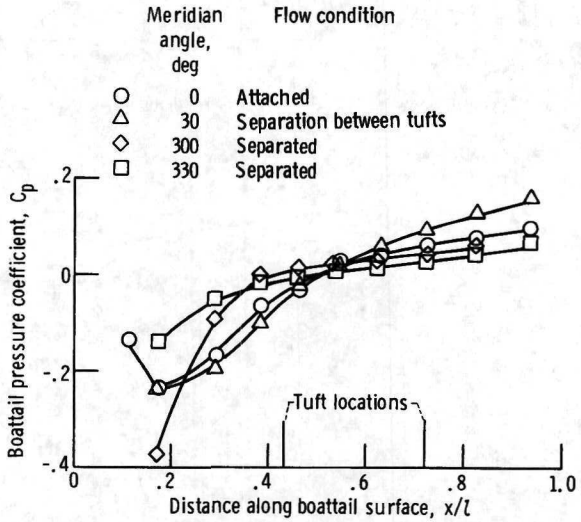

(b) Boattail pressure distribution.

Figure 23. - Separation-pressure correlation. Mach 0.9; altitude, 7620 meters (25 000 ft); Reynolds number, 4.89×10^7; angle of attack, 6^0; nozzle 25.

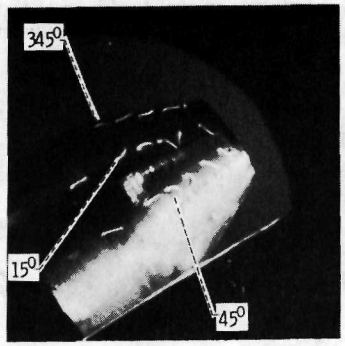

(a) Tuft picture.

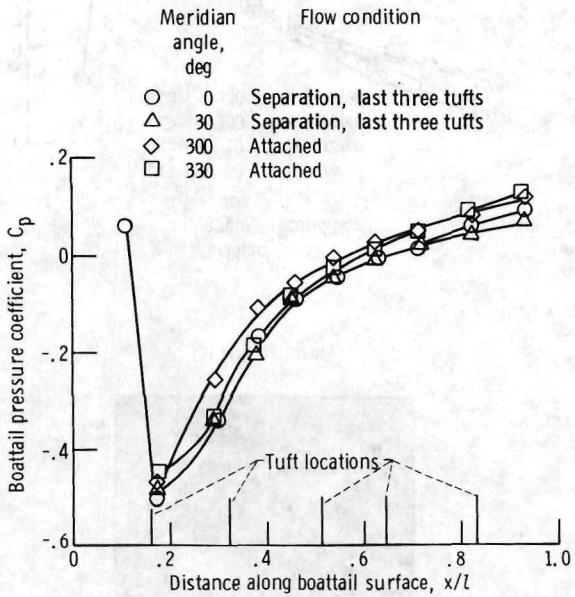

(b) Boattail pressure distribution.

Figure 24. - Separation-pressure correlation. Mach 0.9; altitude, 7620 meters (25 000 ft); Reynolds number, 4.92×10^7; angle of attack, 8^0; nozzle 25Ex.

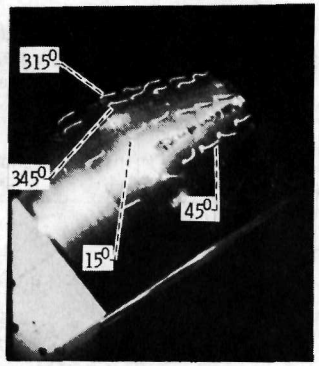

(a) Tuft picture.

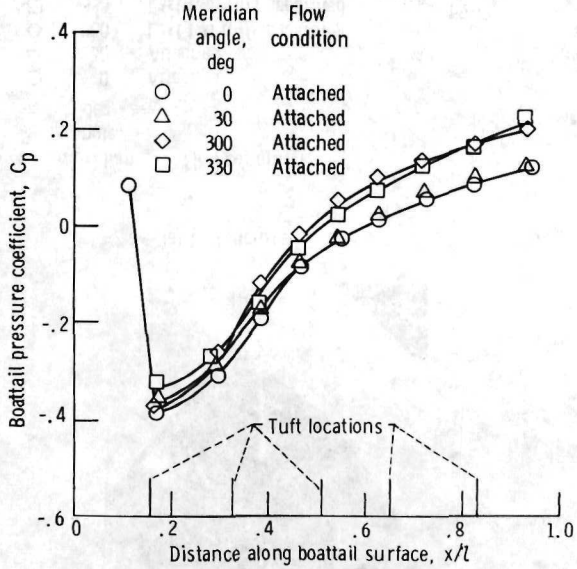

(b) Boattail pressure distribution.

Figure 25. - Separation-pressure correlation; Mach 0.6; altitude, 4572 meters (15 000 ft); Reynolds number, 4.79×10^7; angle of attack, 8^0; nozzle 25Ex.

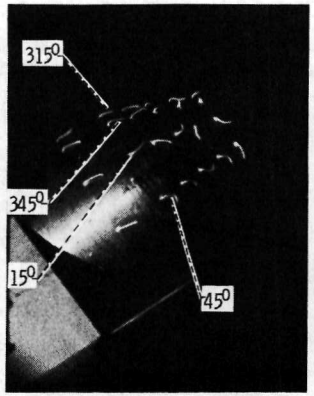

(a) Tuft picture.

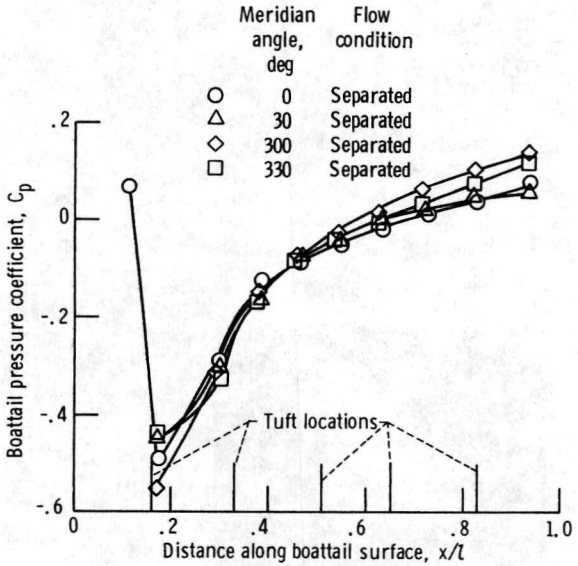

(b) Boattail pressure distribution.

Figure 26. - Separation-pressure correlation. Mach 0.9; altitude, 7620 meters (25 000 ft); Reynolds number, 4.92×10^7; angle of attack, 6^0; nozzle 25Ex.

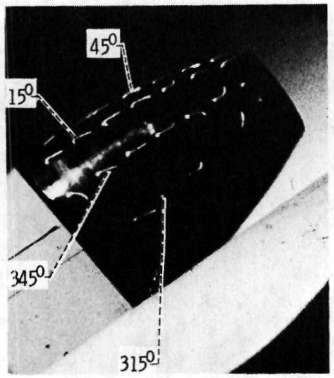

(a) Tuft picture.

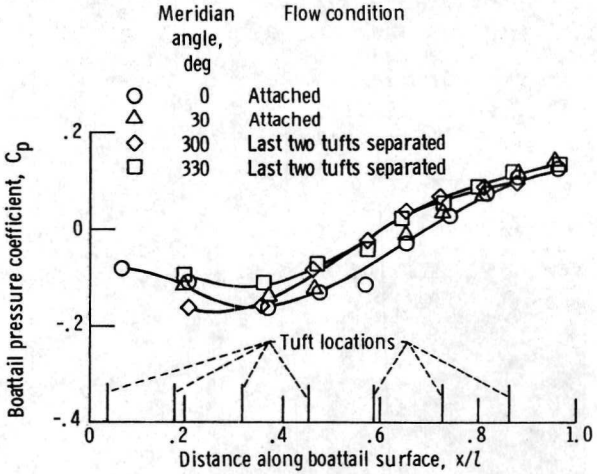

(b) Boattail pressure distribution.

Figure 27. - Separation-pressure correlation. Mach 0.9; altitude, 10 668 meters (35 000 ft); Reynolds number, 3.06×10^7; angle of attack, 7^0; nozzle 100.

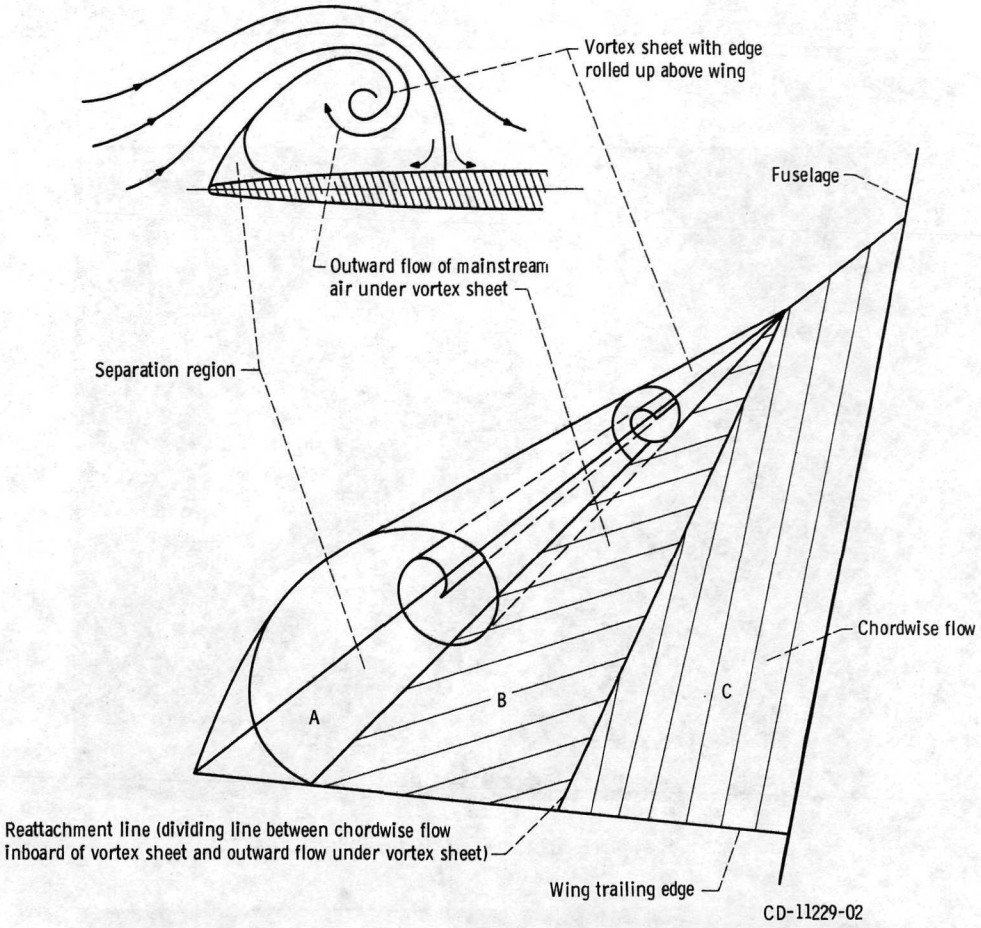

Figure 28. - Delta wing flow pattern (ref. 11).

Figure 29. - Tuft positions on left wing.

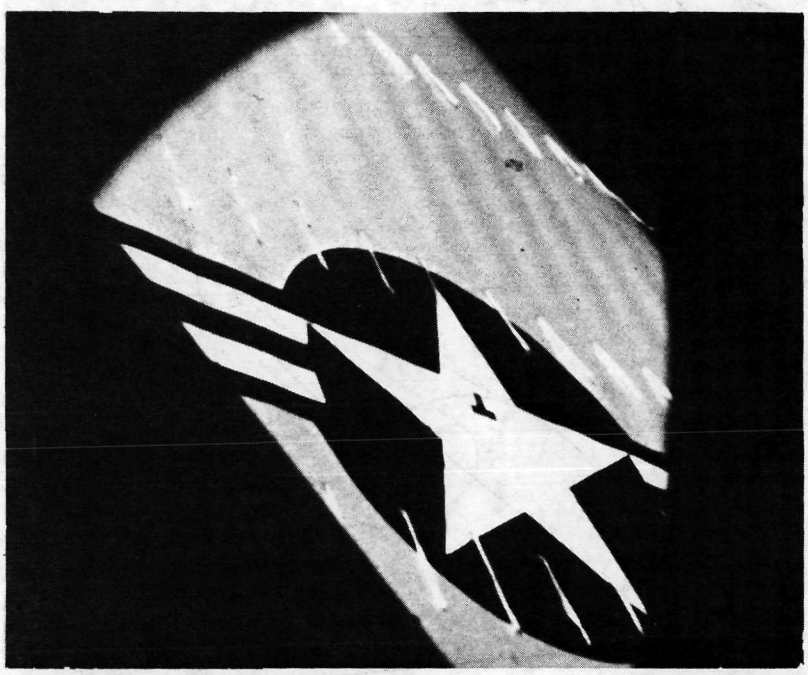

(a) Mach 0.6; altitude, 4572 meters (15 000 ft); angle of attack, 11°.

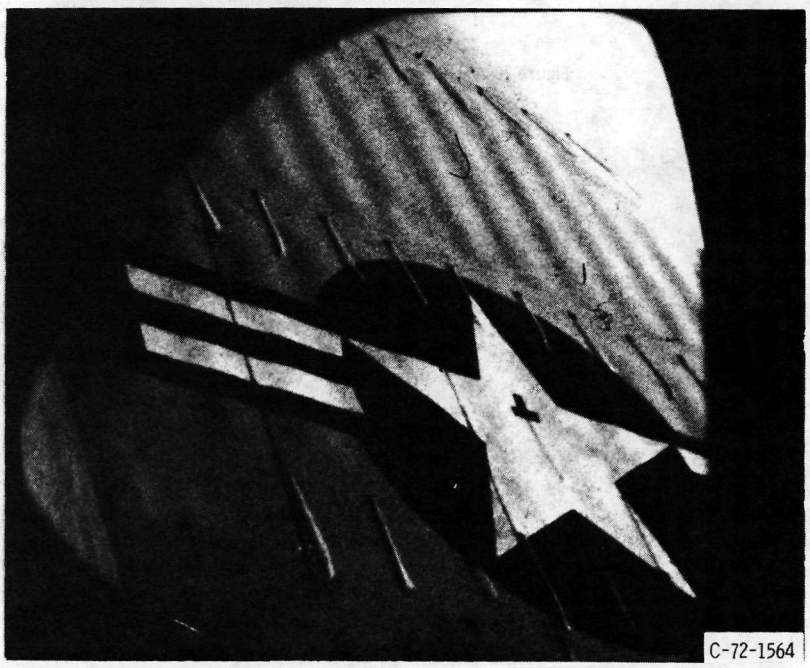

(b) Mach 0.9; altitude, 7620 meters (25 000 ft); angle of attack, 9°.

Figure 30. - Wing tuft pictures.

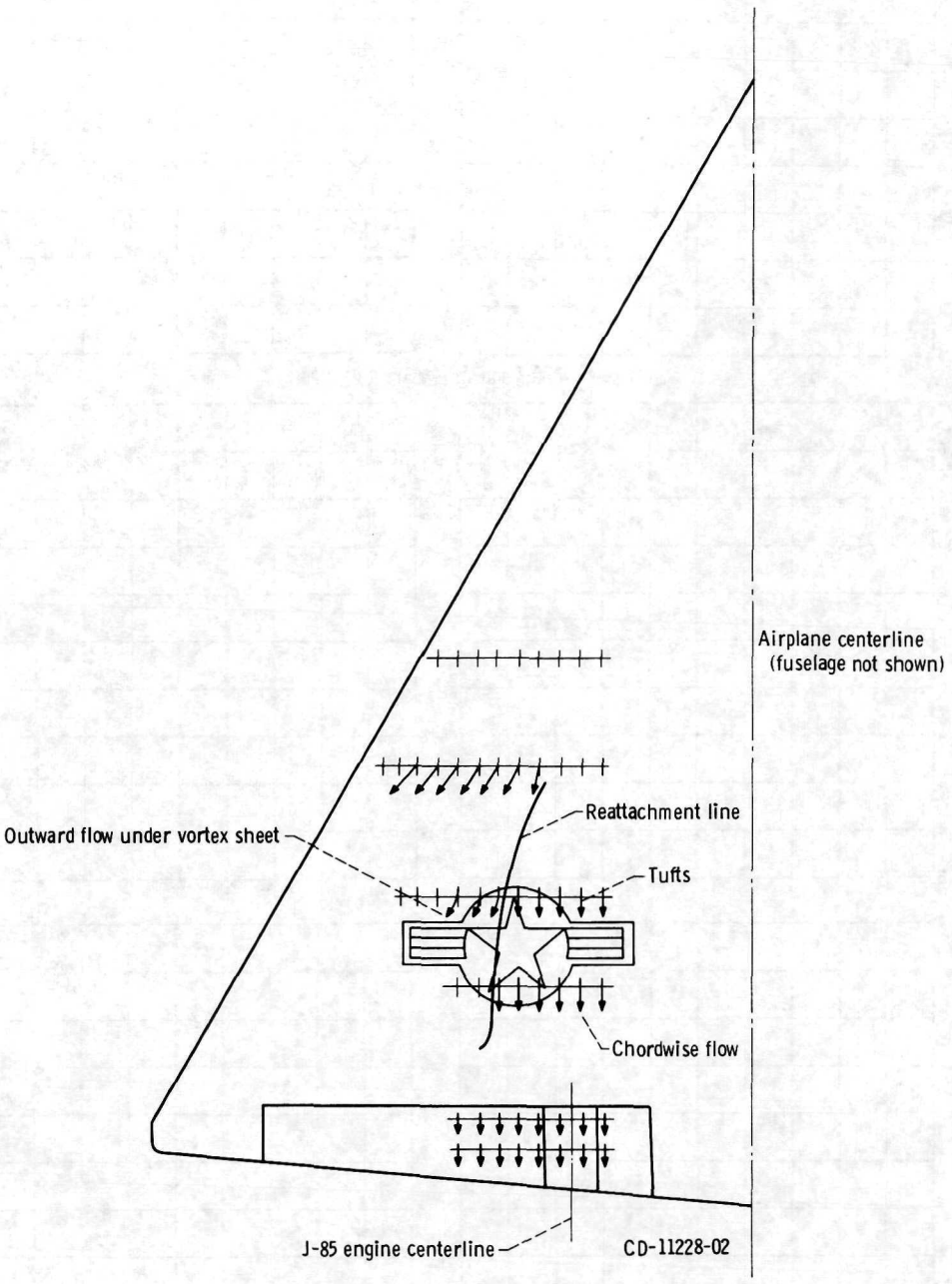

Figure 31. - Wing flow characteristics. Mach 0.6; altitude, 4572 meters (15 000 ft); angle of attack, 11^{0}.

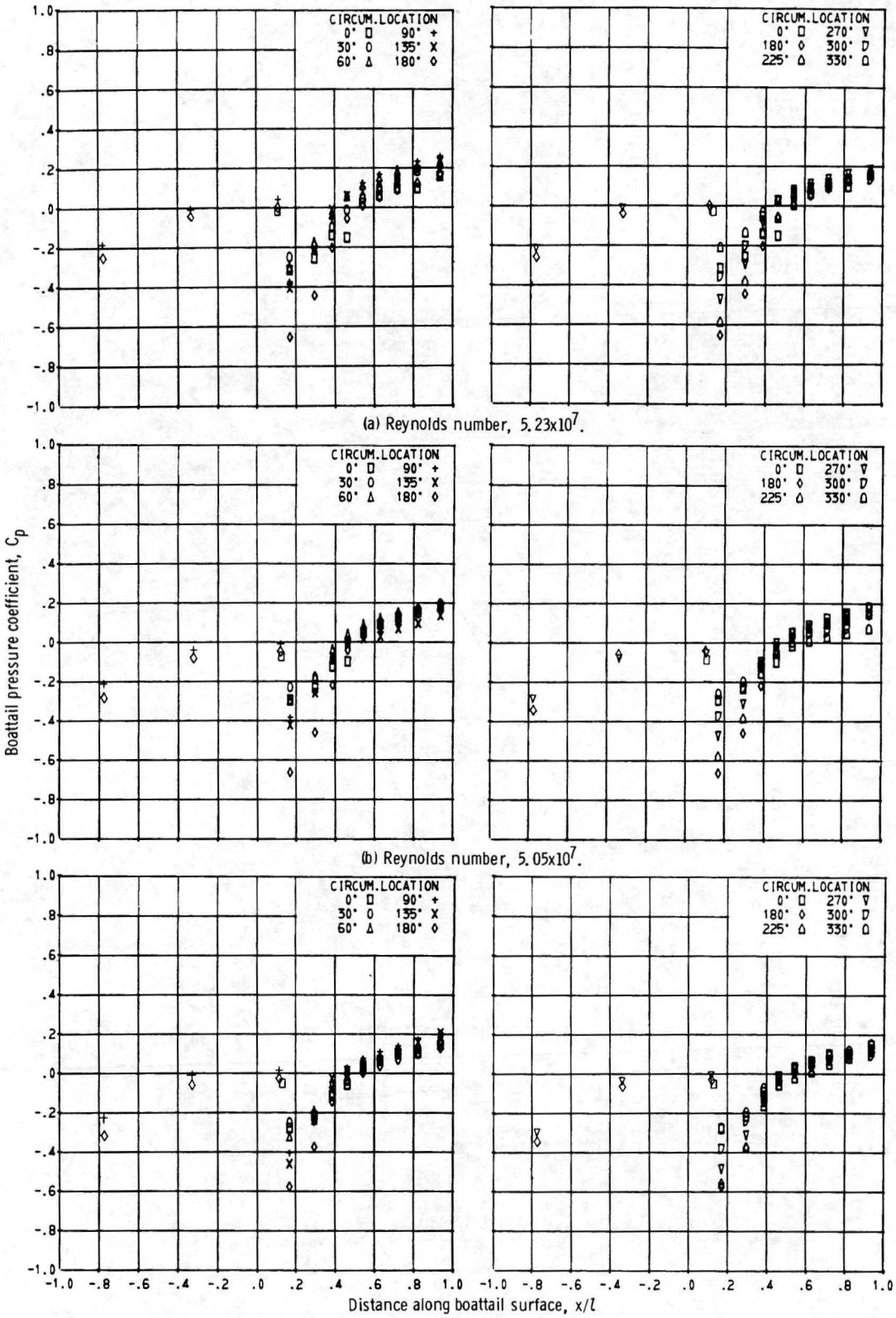

(a) Reynolds number, 5.23×10^7.

(b) Reynolds number, 5.05×10^7.

(c) Reynolds number, 4.27×10^7.

Figure 32. - Reynolds number effect on boattail pressure distribution. Mach 0.6; angle of attack, 13°; nozzle 25.

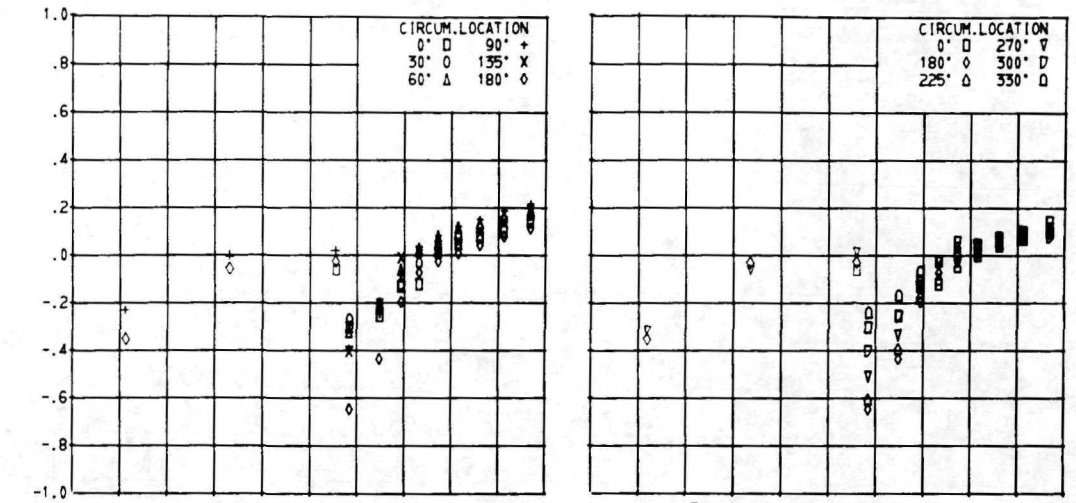

(d) Reynolds number, 3.52×10^7.

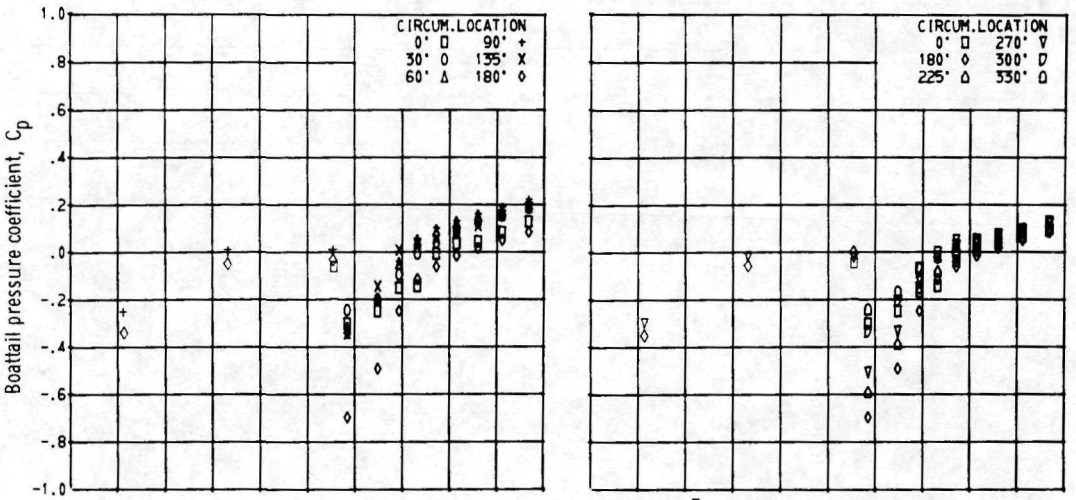

(e) Reynolds number, 2.90×10^7.

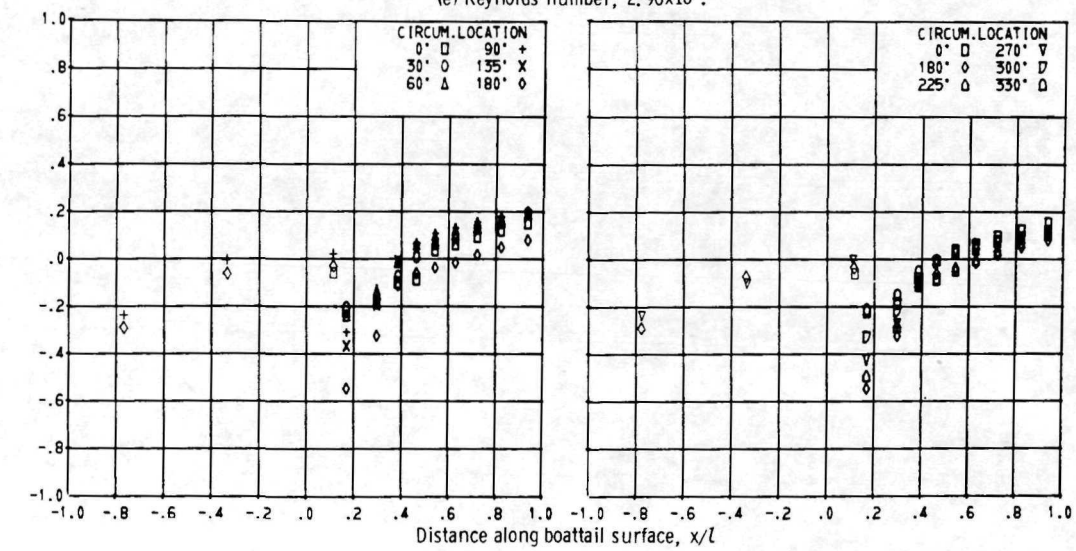

(f) Reynolds number, 2.86×10^7.

Figure 32. - Continued.

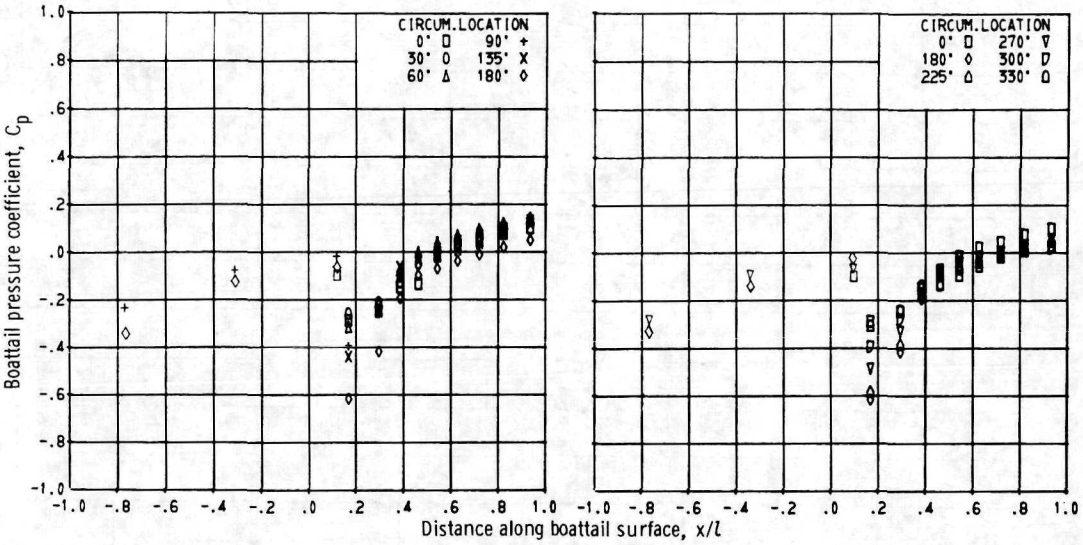

(g) Reynolds number, 2.30×10^7.

Figure 32. - Concluded.

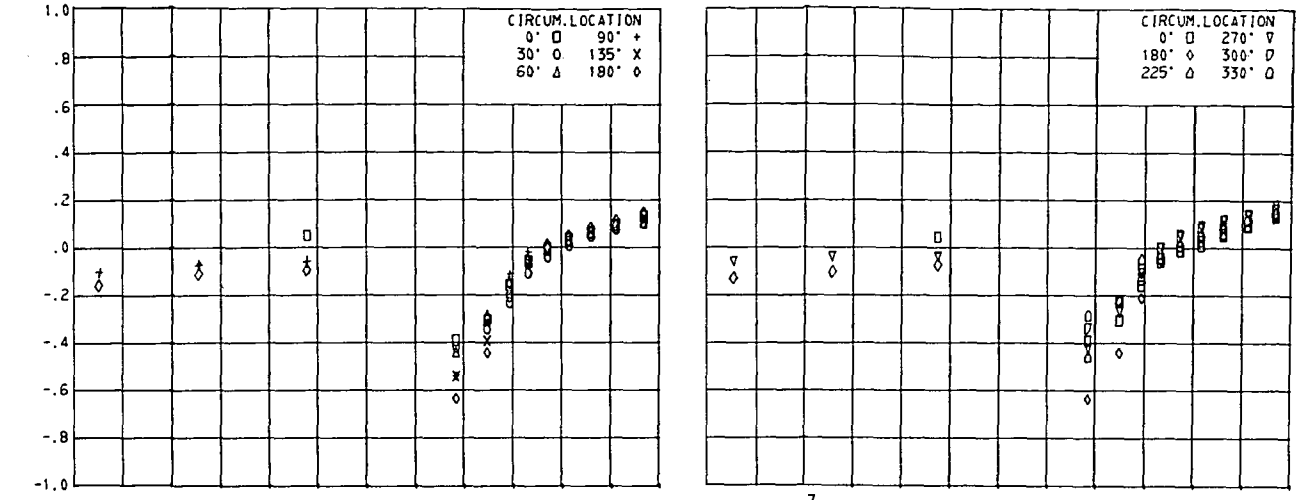

(a) Reynolds number, 4.58×10^7.

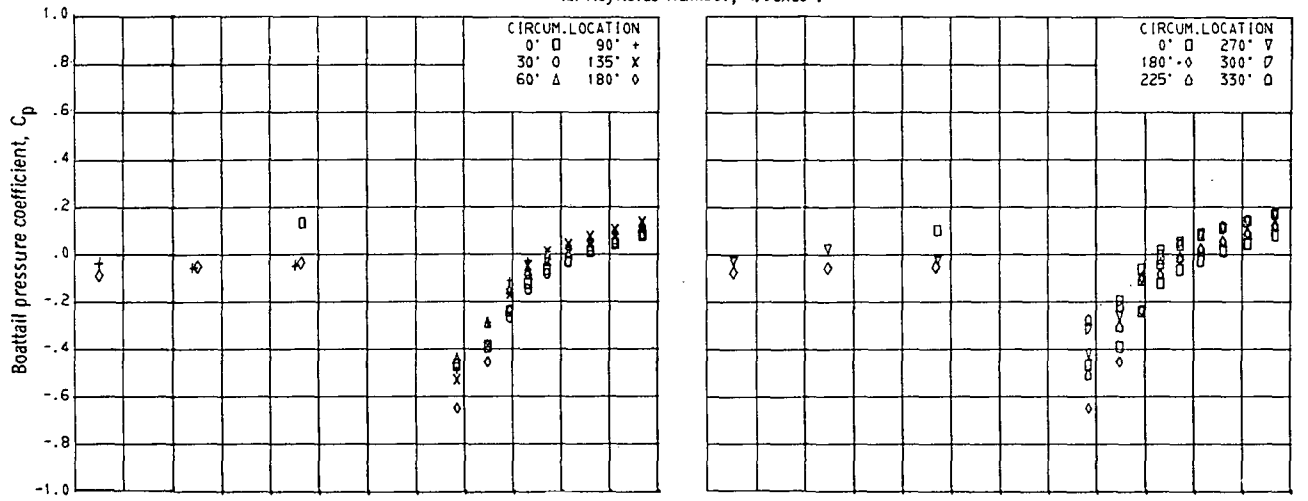

(b) Reynolds number, 3.65×10^7.

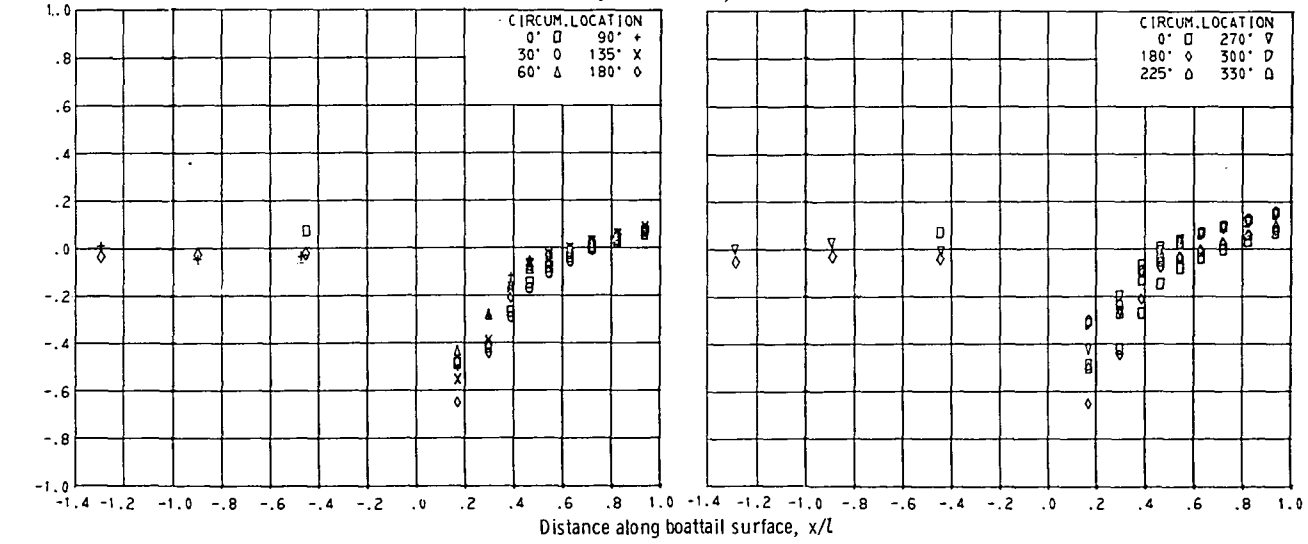

(c) Reynolds number, 3.18×10^7.

Figure 33. - Reynolds number effect on boattail pressure distribution. Mach 0.6; angle of attack, 13^0; nozzle 25 Ex.

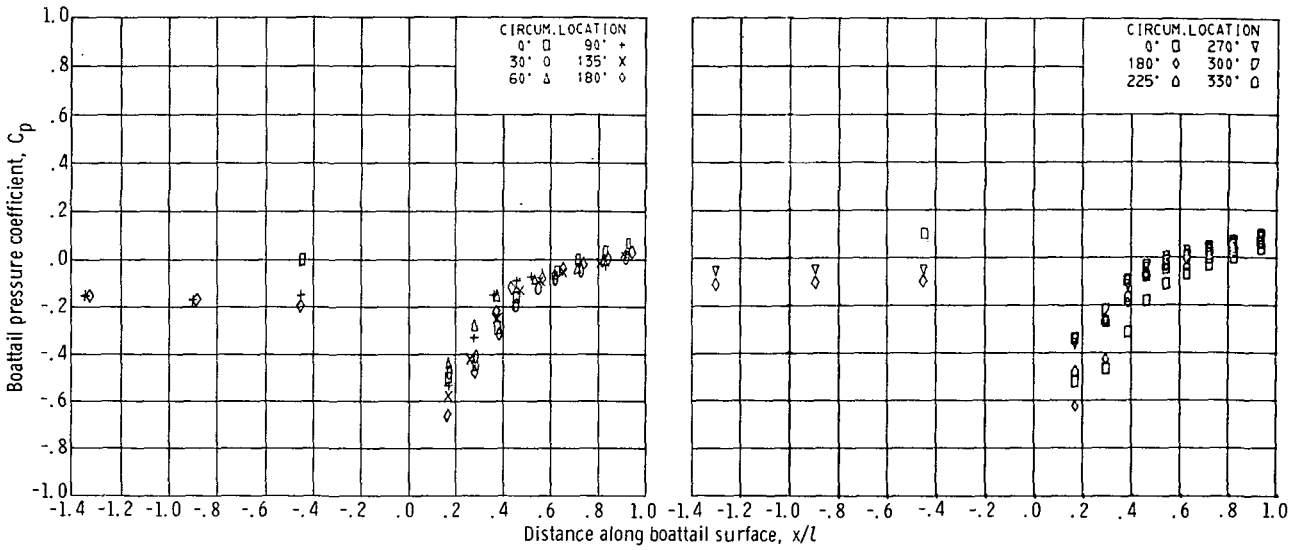

(d) Reynolds number, 2.64×10^7.

Figure 33. - Concluded.

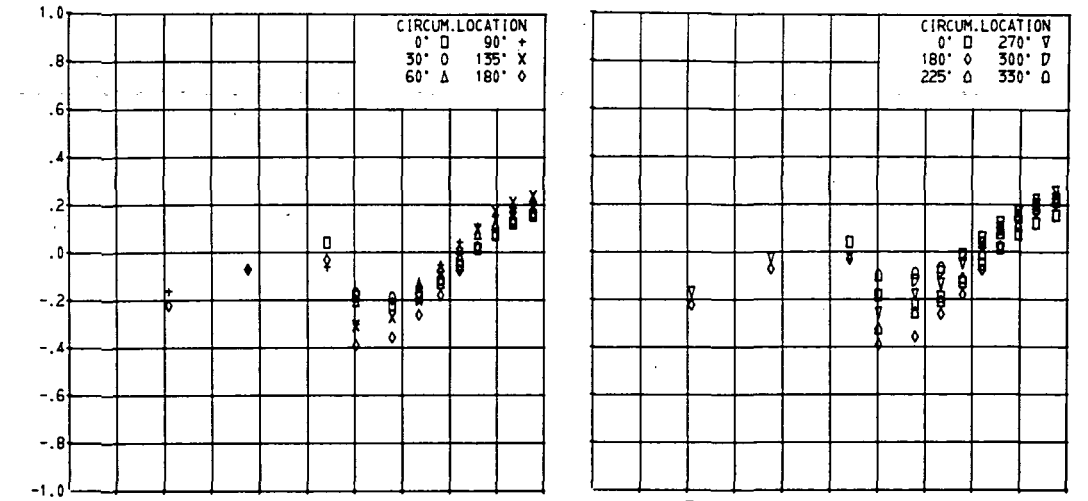

(a) Reynolds number, 5.23×10^7.

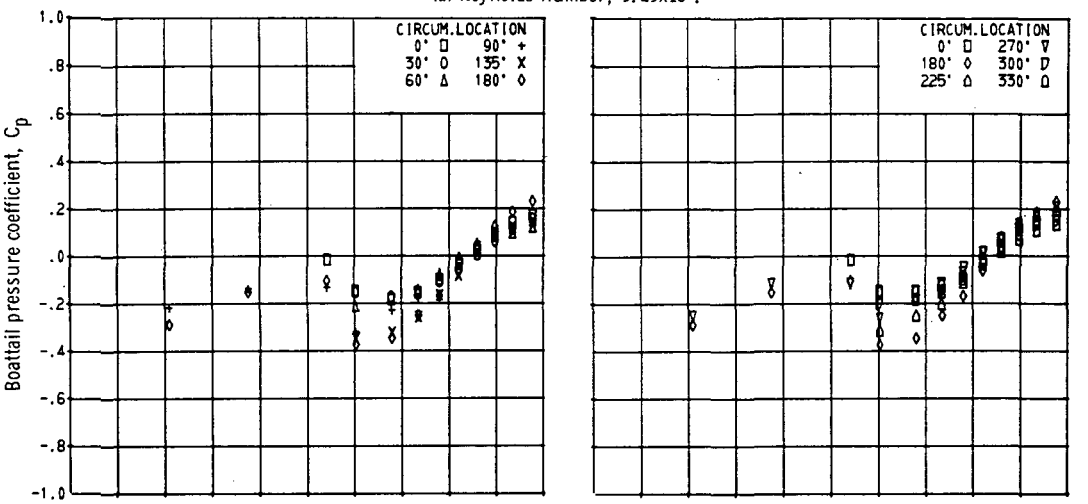

(b) Reynolds number, 5.05×10^7.

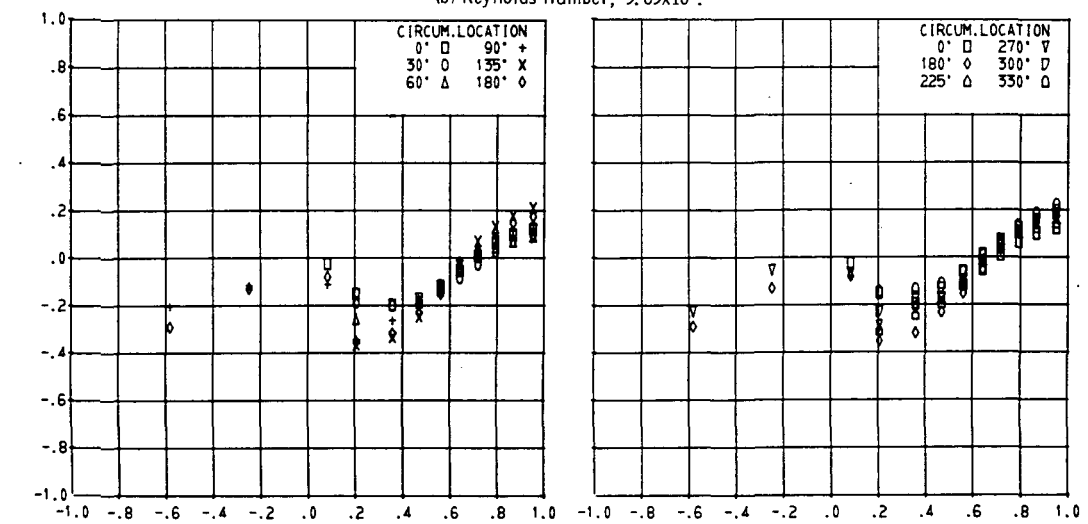

(c) Reynolds number, 4.27×10^7.

Figure 34. - Reynolds number effect on boattail pressure distribution. Mach 0.6; angle of attack, 13^0; nozzle 65.

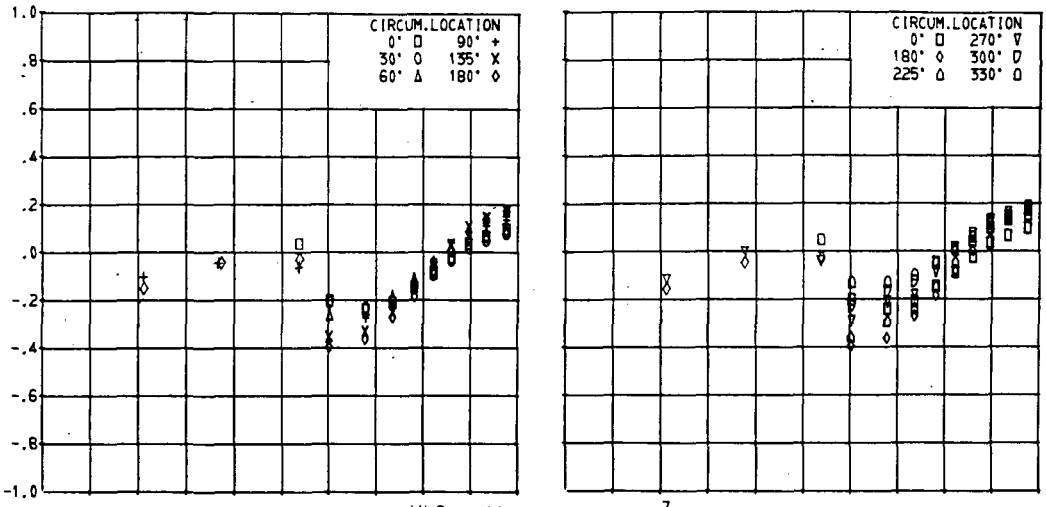

(d) Reynolds number, 3.52×10^7.

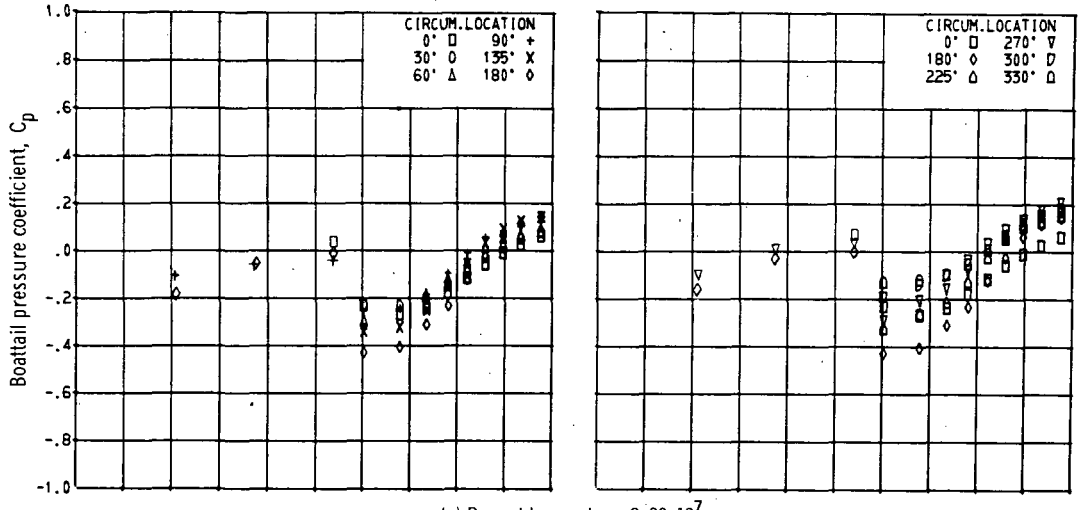

(e) Reynolds number, 2.90×10^7.

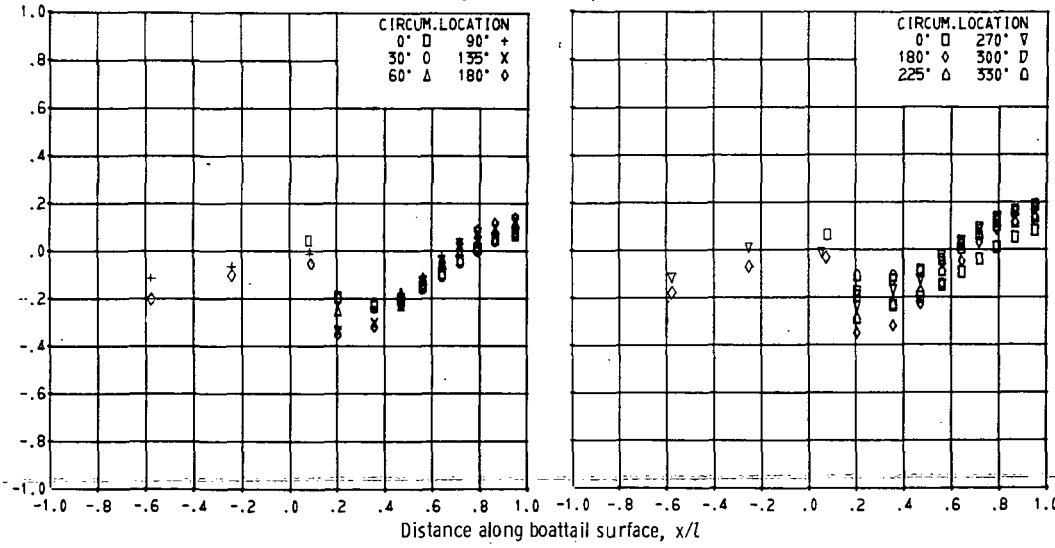

(f) Reynolds number, 2.86×10^7.

Figure 34. - Continued.

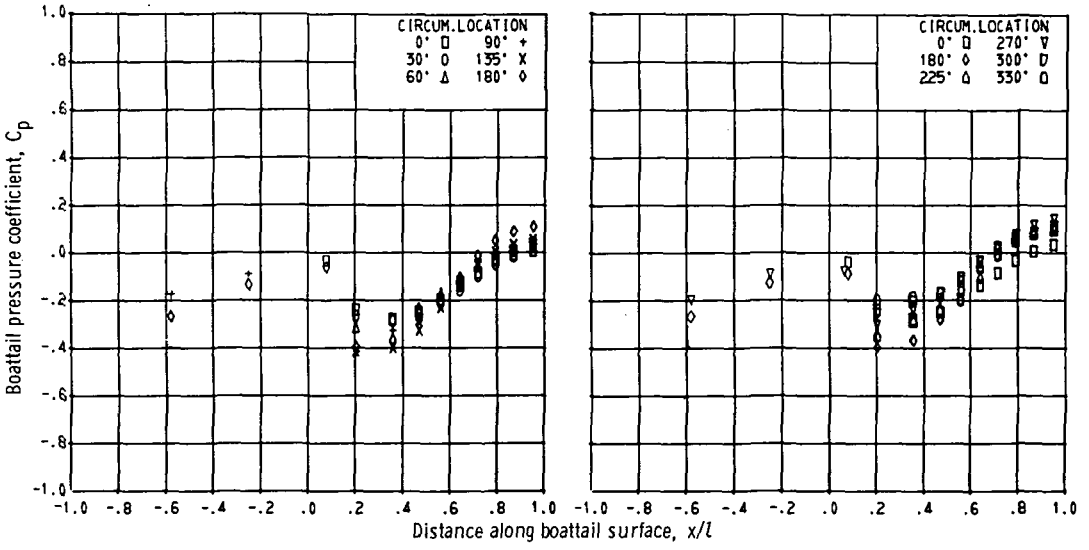

(g) Reynolds number, 2.30×10^7.

Figure 34. - Concluded.

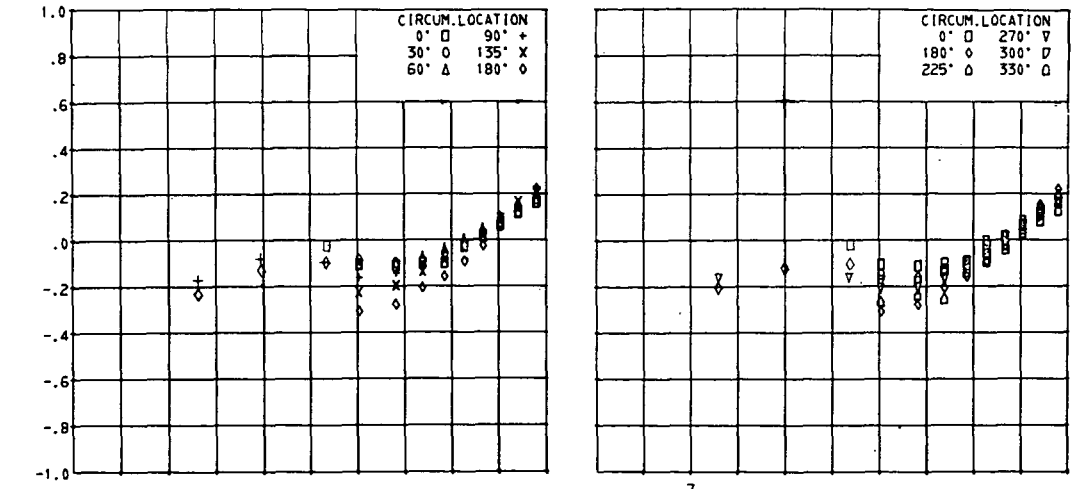

(a) Reynolds number, 4.58×10^7.

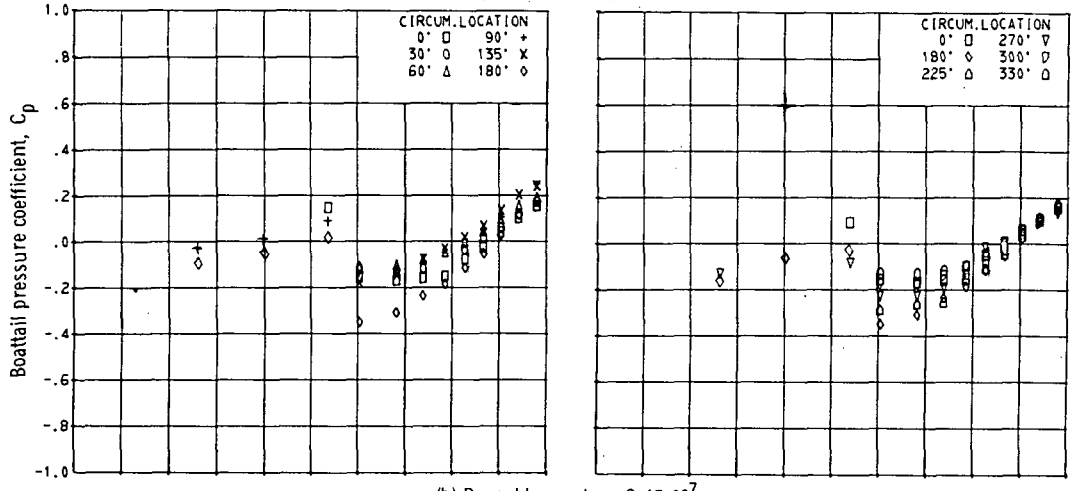

(b) Reynolds number, 3.65×10^7.

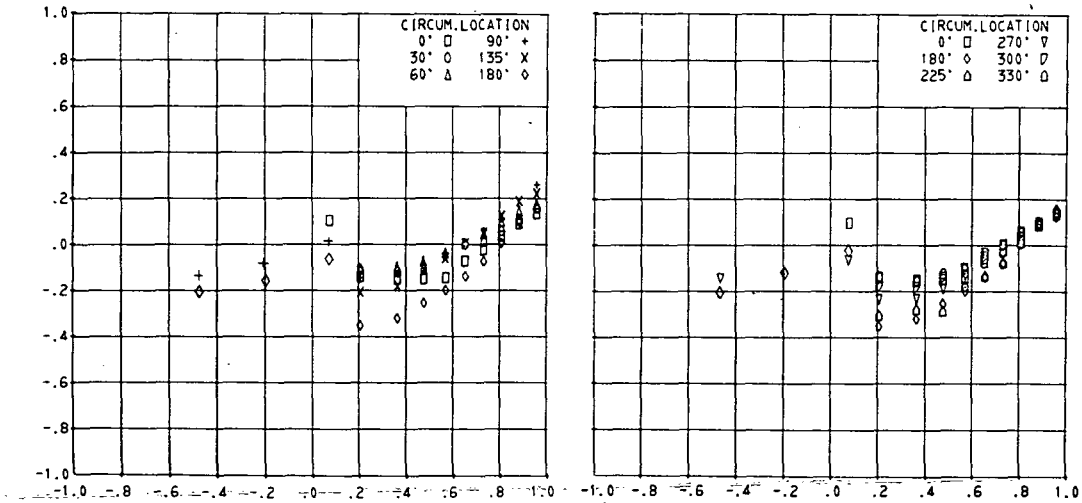

(c) Reynolds number, 3.18×10^7.

Boattail pressure coefficient, C_p

Distance along boattail surface, x/l

Figure 35. - Reynolds number effect on boattail pressure distribution. Mach 0.6; angle of attack, 13^0; nozzle 100.

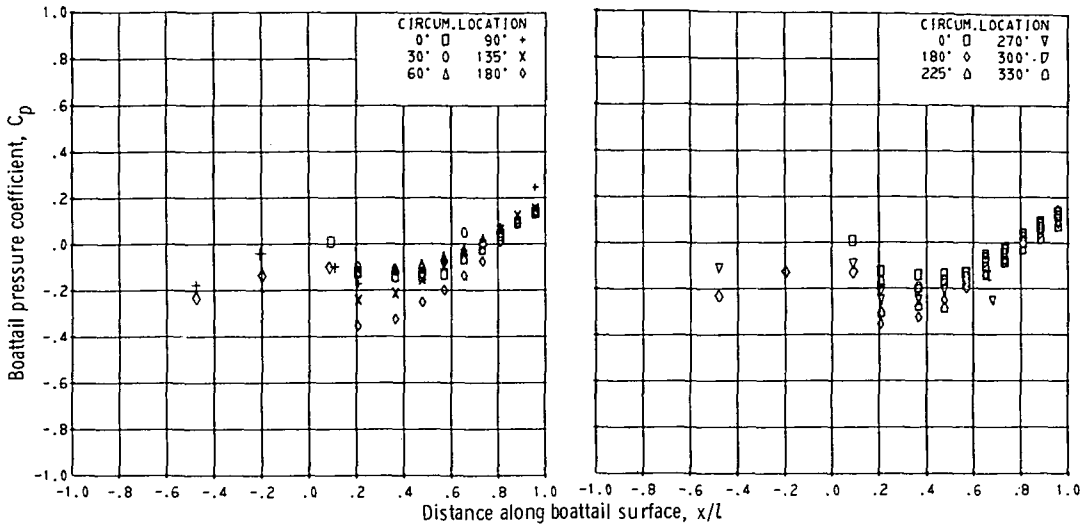

(d) Reynolds number, 2.64×10^7.

Figure 35. - Concluded.

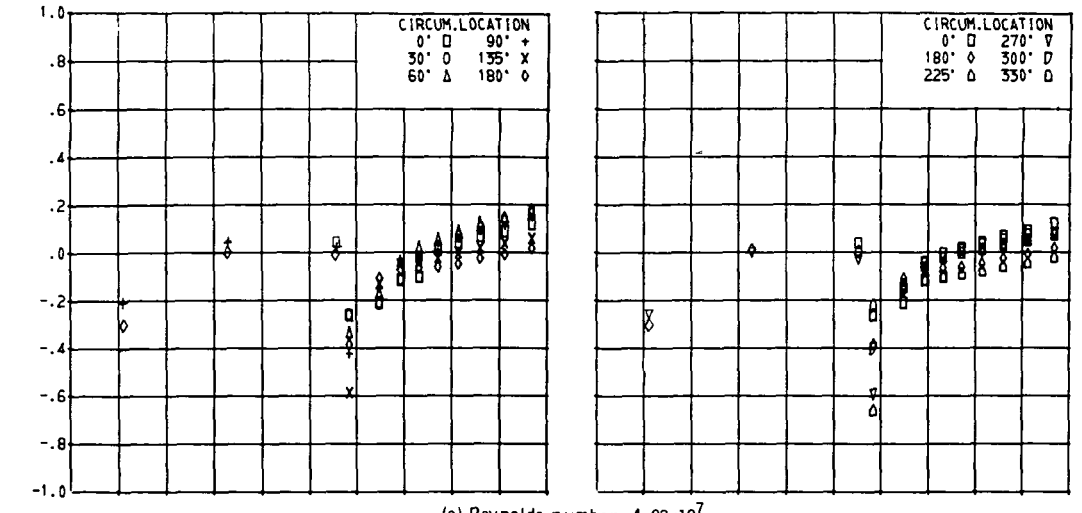

(a) Reynolds number, 4.88×10^7.

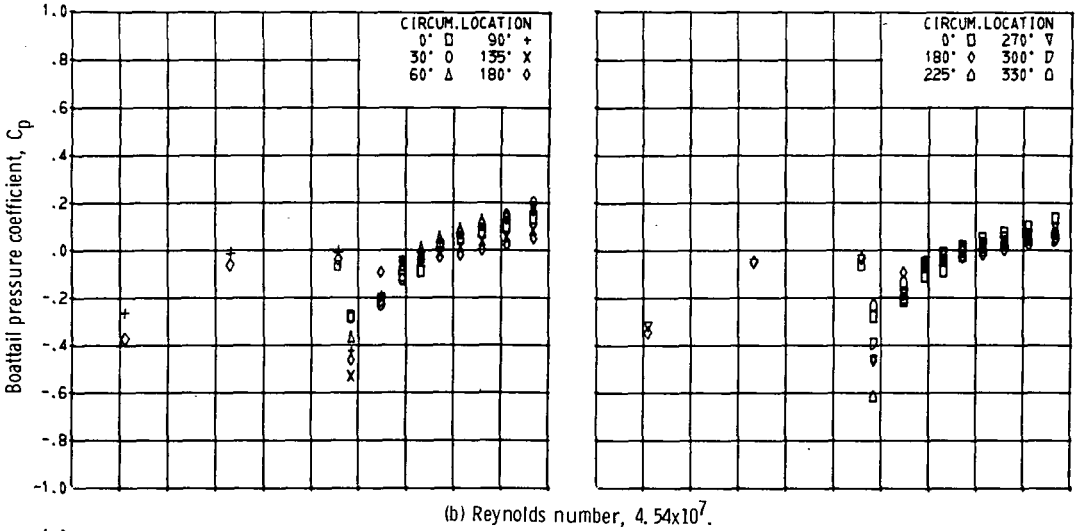

(b) Reynolds number, 4.54×10^7.

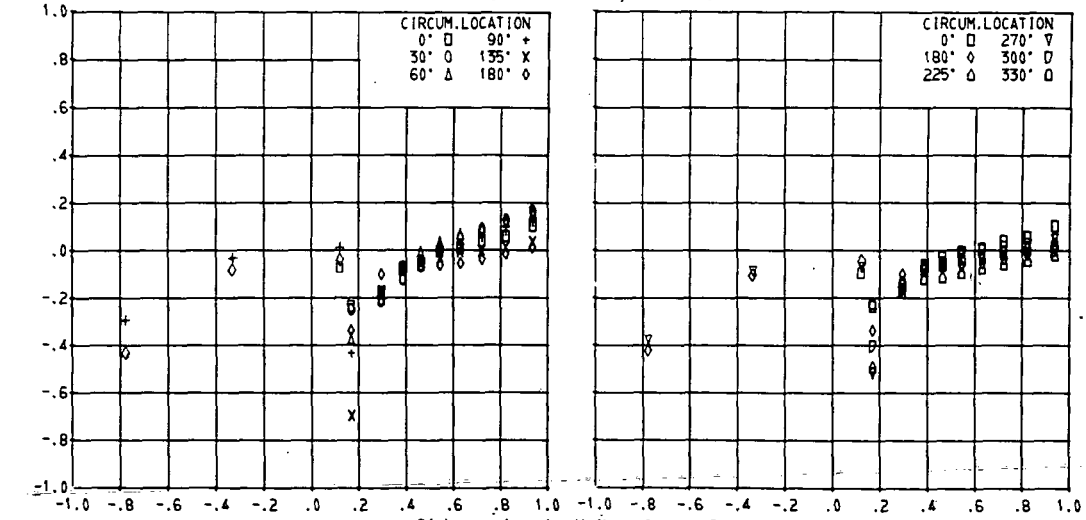

(c) Reynolds number, 3.81×10^7.

Boattail pressure coefficient, C_p

Distance along boattail surface, x/l

Figure 36. - Reynolds number effect on boattail pressure distribution, Mach 0.9; angle of attack, 9^0; nozzle 25.

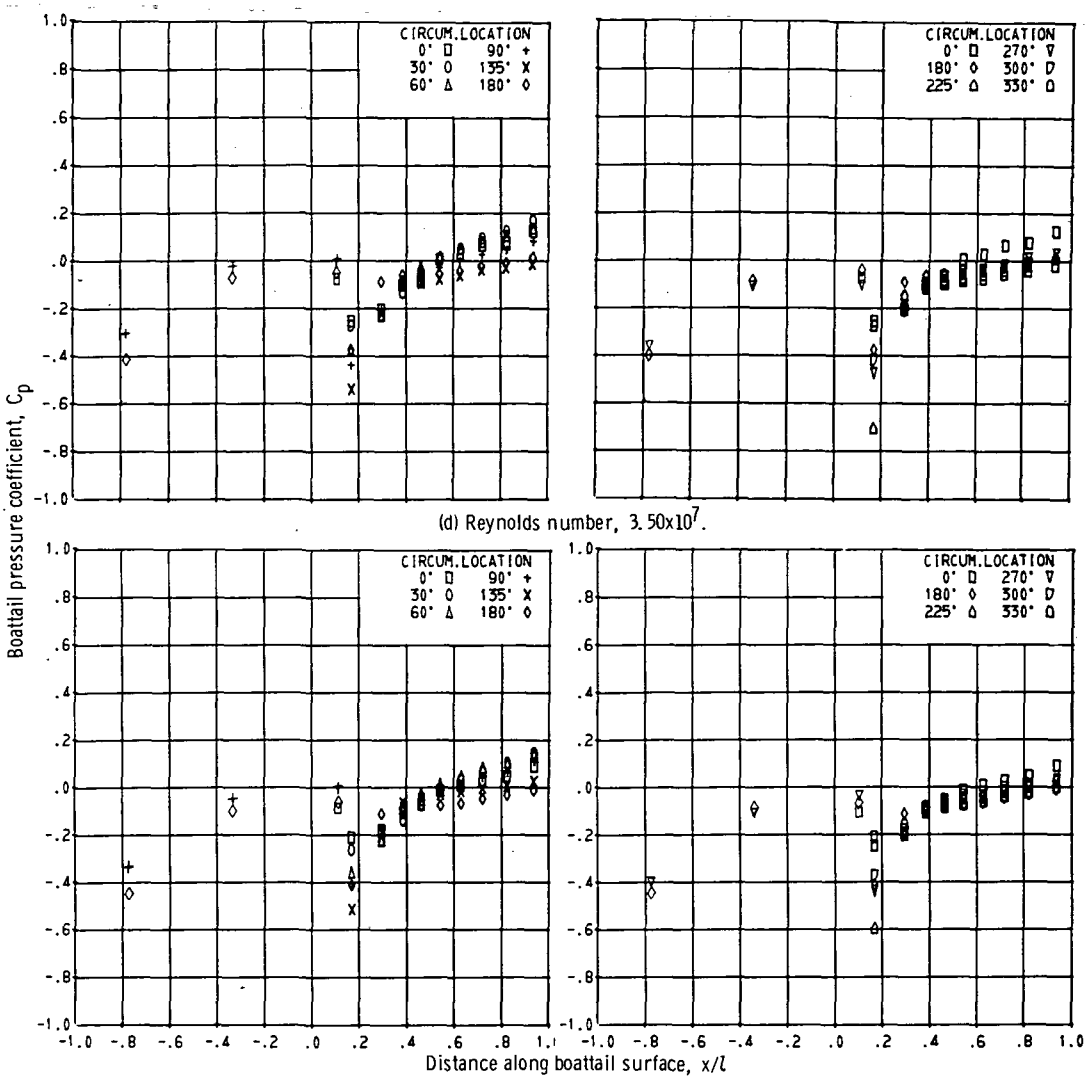

(d) Reynolds number, 3.50×10^7.

(e) Reynolds number, 2.80×10^7.

Figure 36. - Concluded.

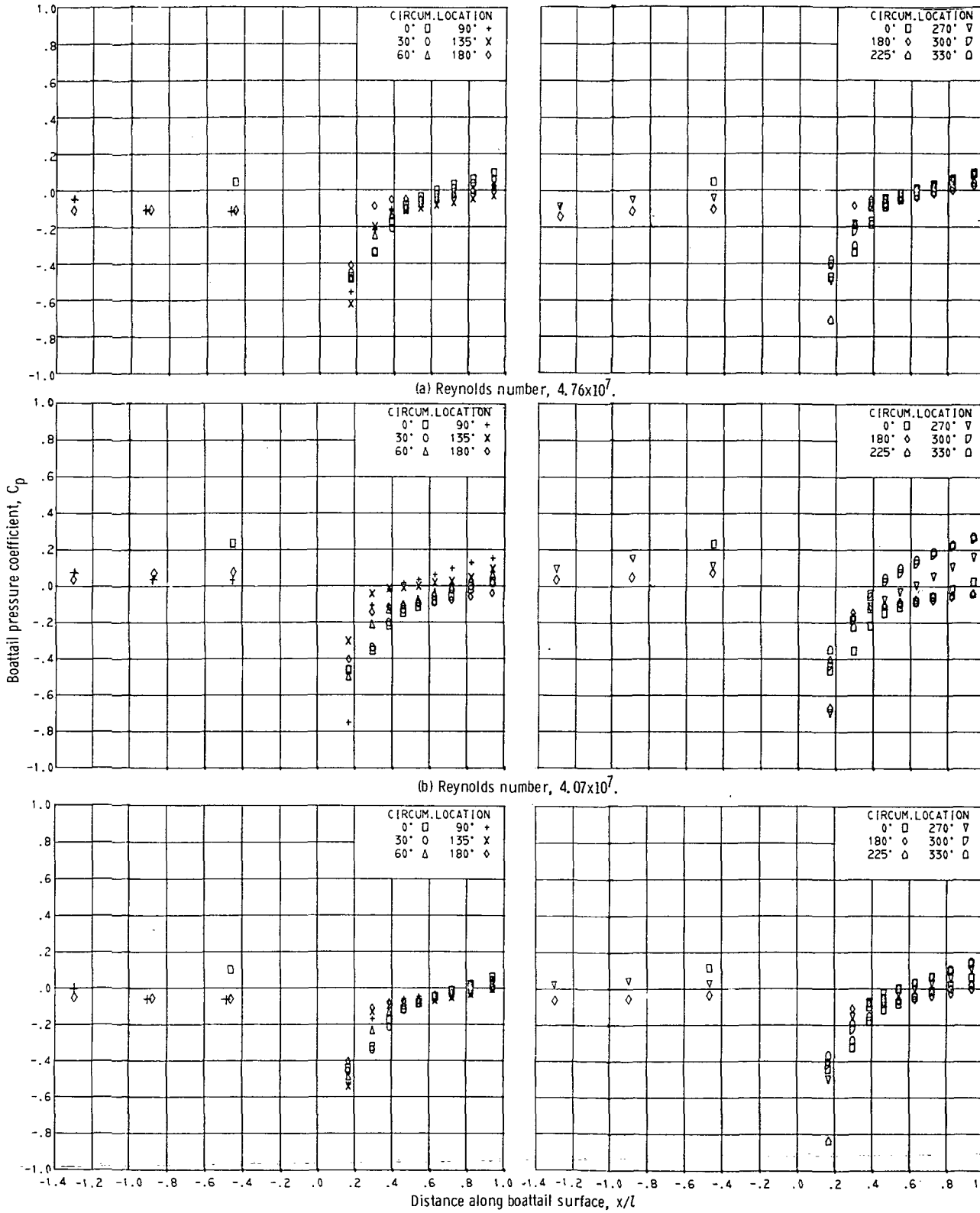

(a) Reynolds number, 4.76×10^7.

(b) Reynolds number, 4.07×10^7.

(c) Reynolds number, 3.75×10^7.

Figure 37. - Reynolds number effect on boattail pressure distribution. Mach 0.9; angle of attack, 9^0; nozzle 25 Ex.

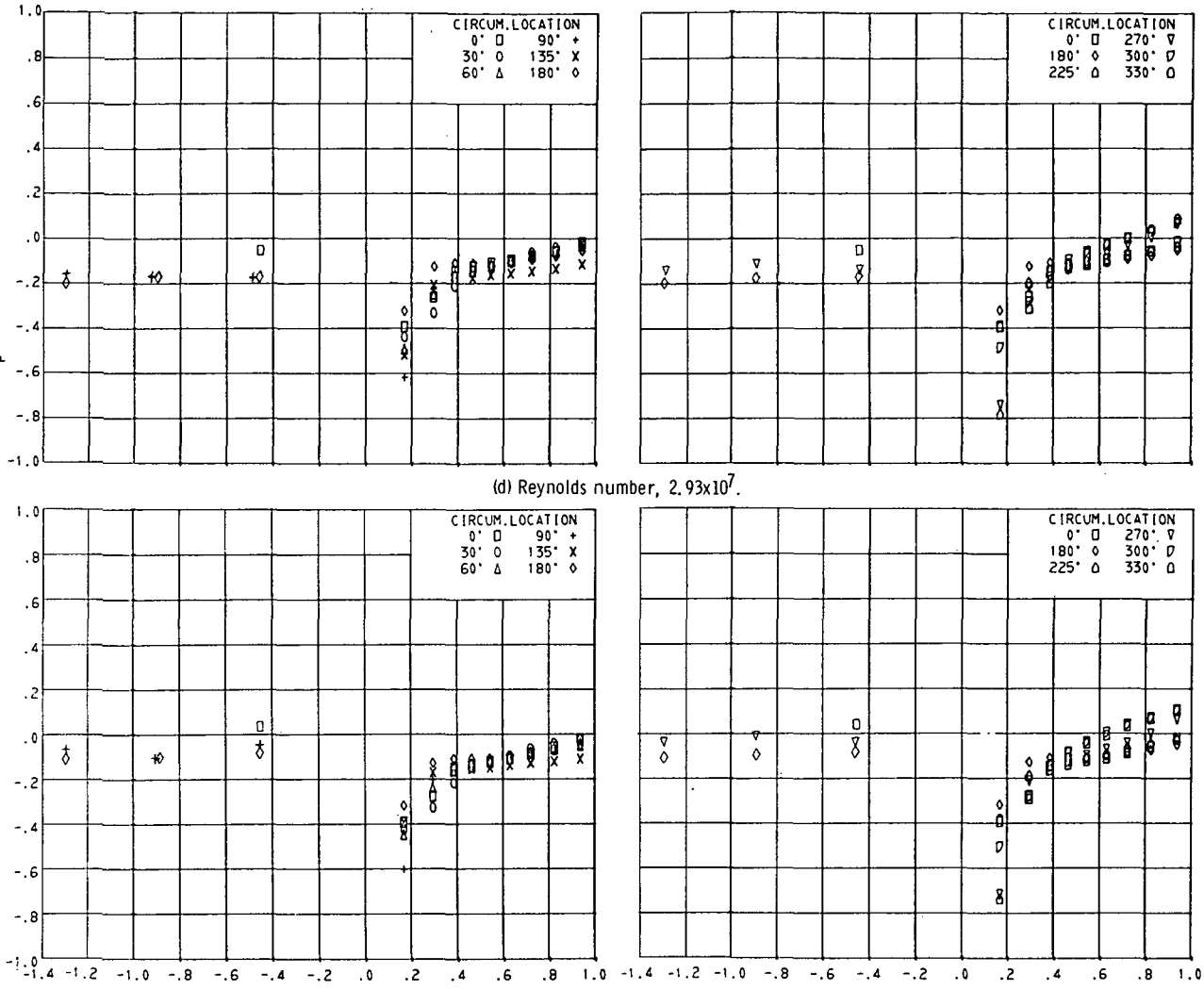

(d) Reynolds number, 2.93×10^7.

(e) Reynolds number, 2.47×10^7.

Figure 37. - Concluded.

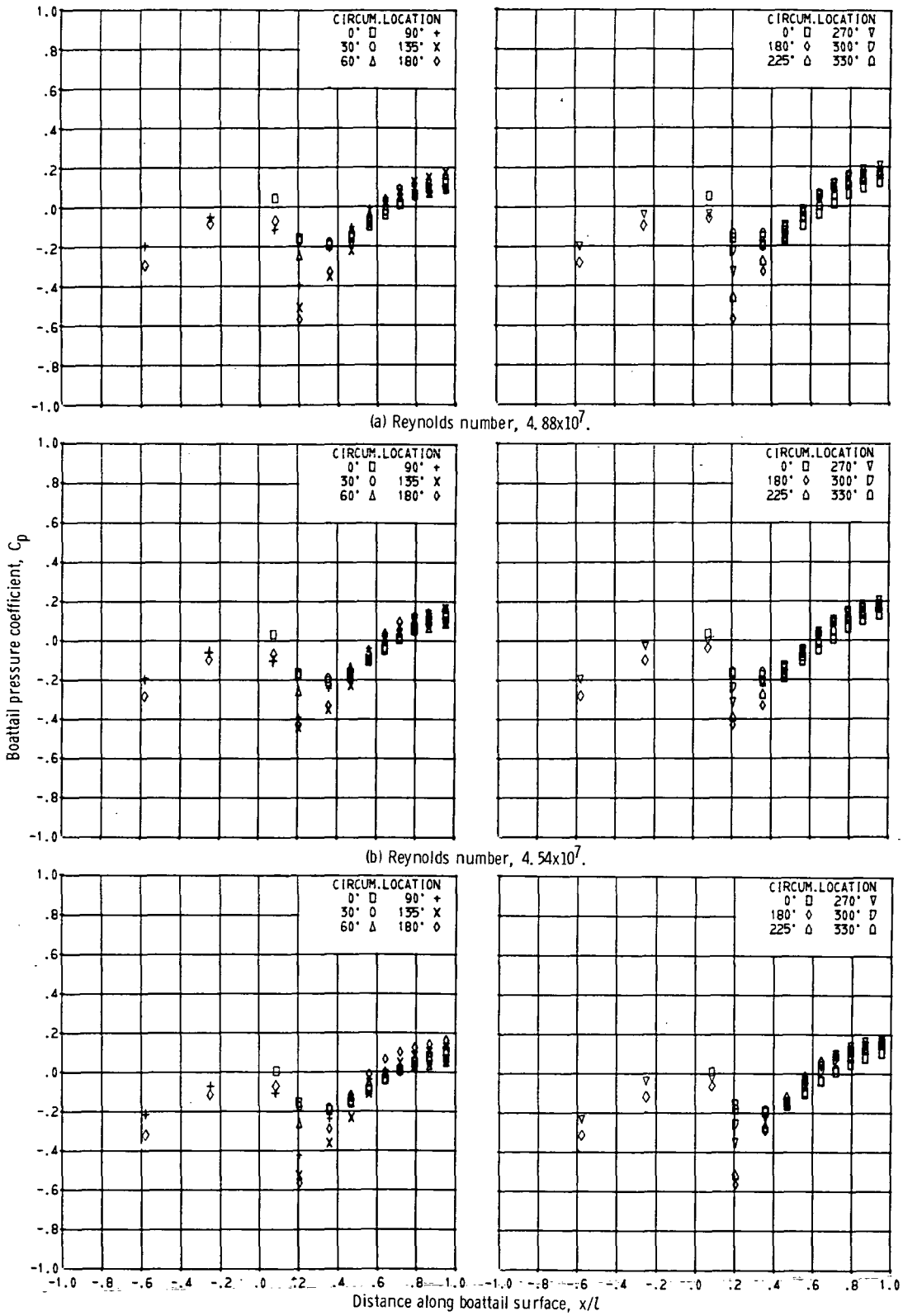

(a) Reynolds number, 4.88×10^7.

(b) Reynolds number, 4.54×10^7.

(c) Reynolds number, 3.81×10^7.

Figure 38. - Reynolds number effect on boattail pressure distribution. Mach 0.9; angle of attack, 9^0; nozzle 65.

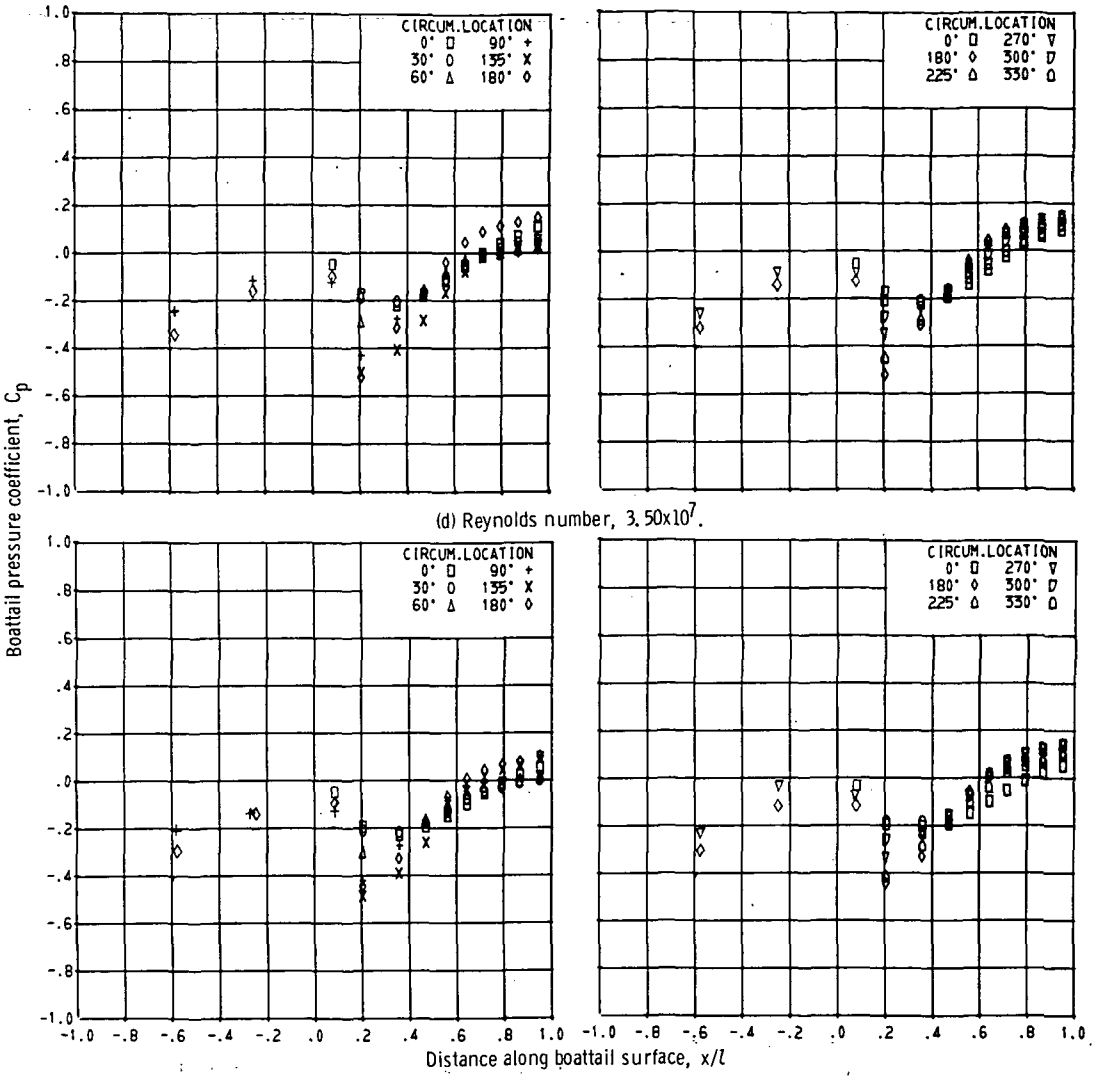

(d) Reynolds number, 3.50×10^7.

(e) Reynolds number, 2.80×10^7.

Figure 38. - Concluded.

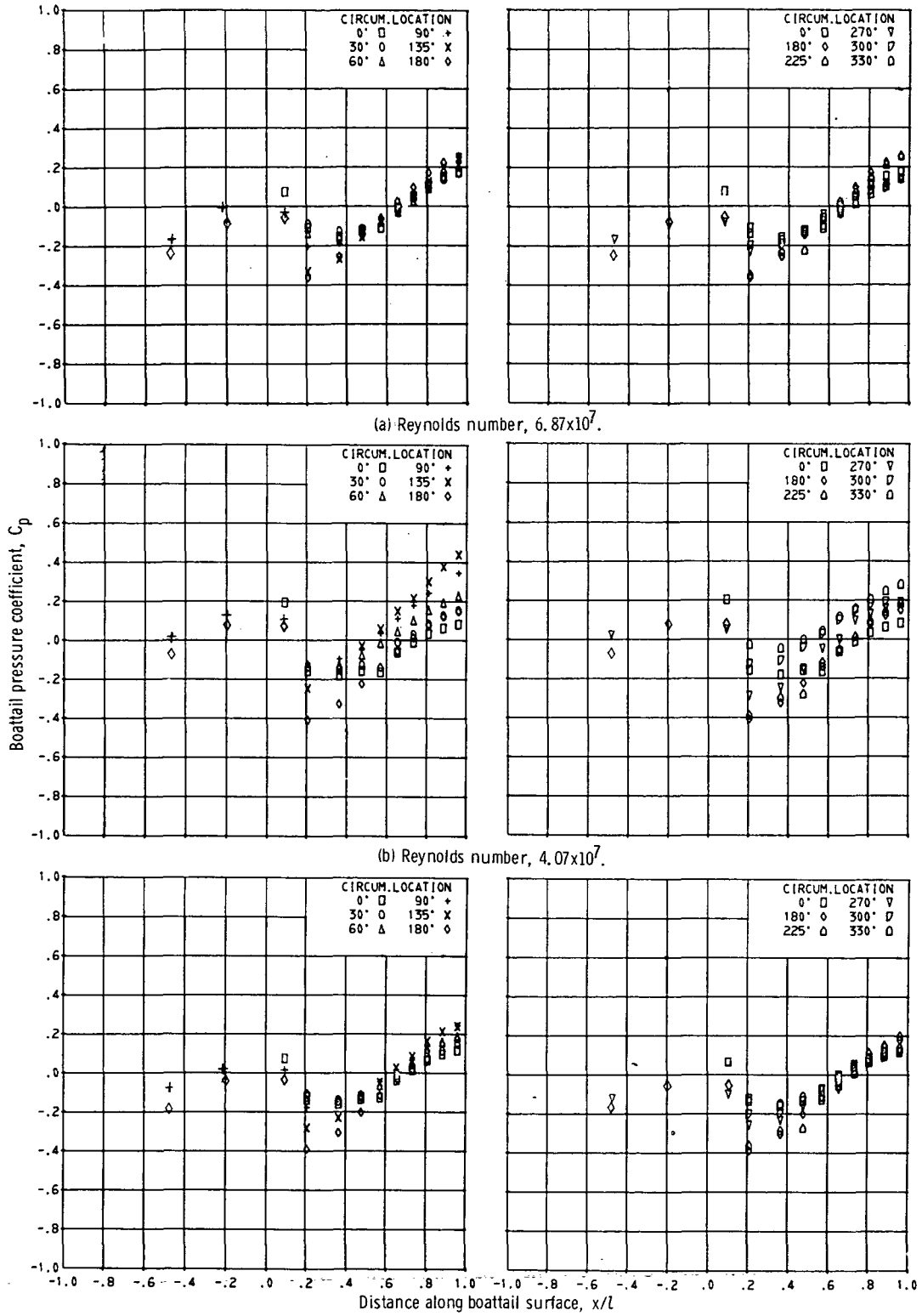

(a) Reynolds number, 6.87×10^7.

(b) Reynolds number, 4.07×10^7.

(c) Reynolds number, 3.75×10^7.

Figure 39. - Reynolds number effect on boattail pressure distribution. Mach 0.9; angle of attack, 9^0; nozzle 100.

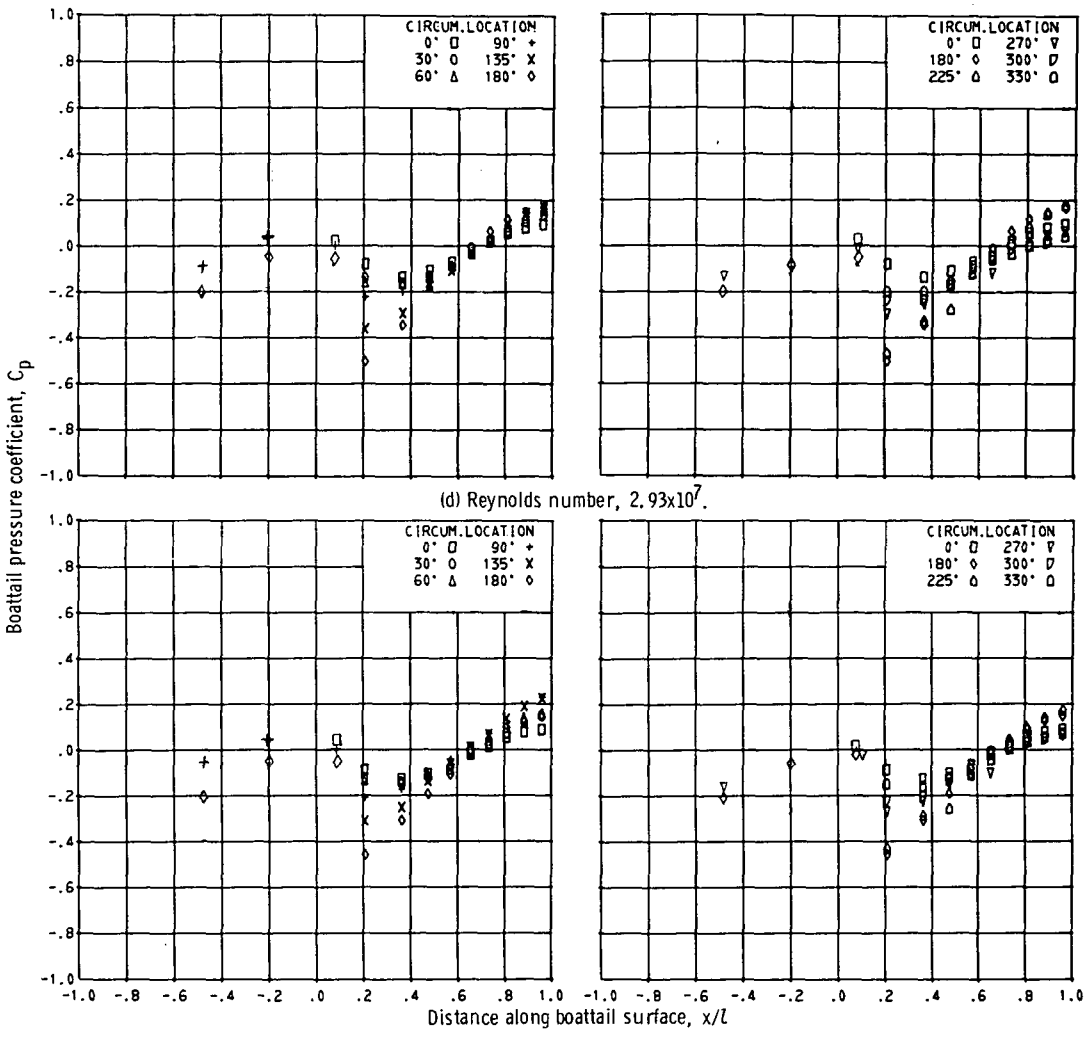

(d) Reynolds number, 2.93×10^7.

(e) Reynolds number, 2.47×10^7.

Figure 39. - Concluded.

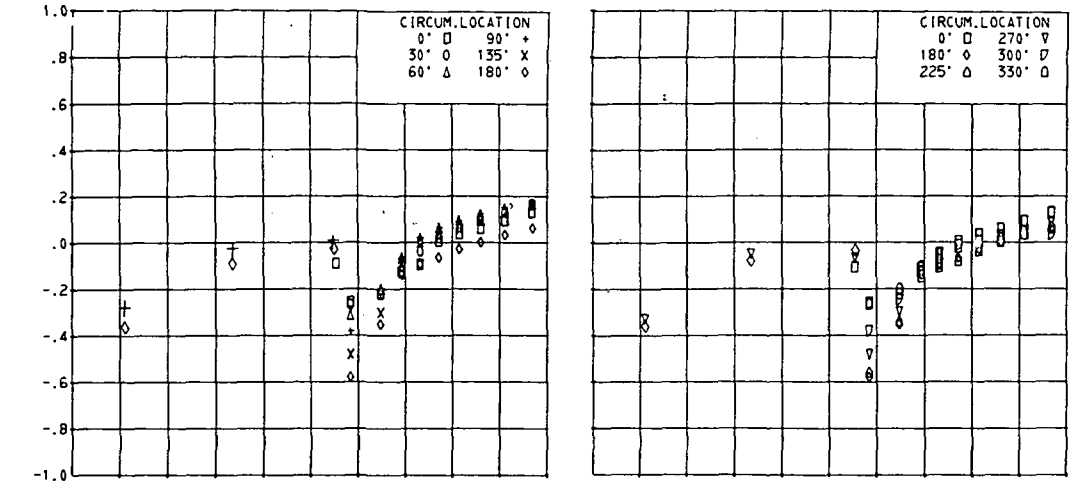

(a) Angle of attack, 11.4°.

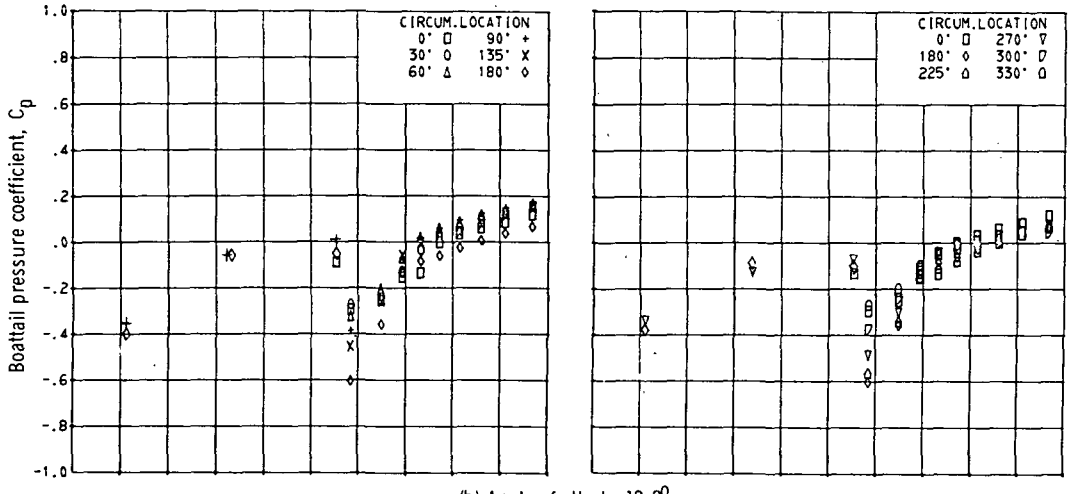

(b) Angle of attack, 12.2°.

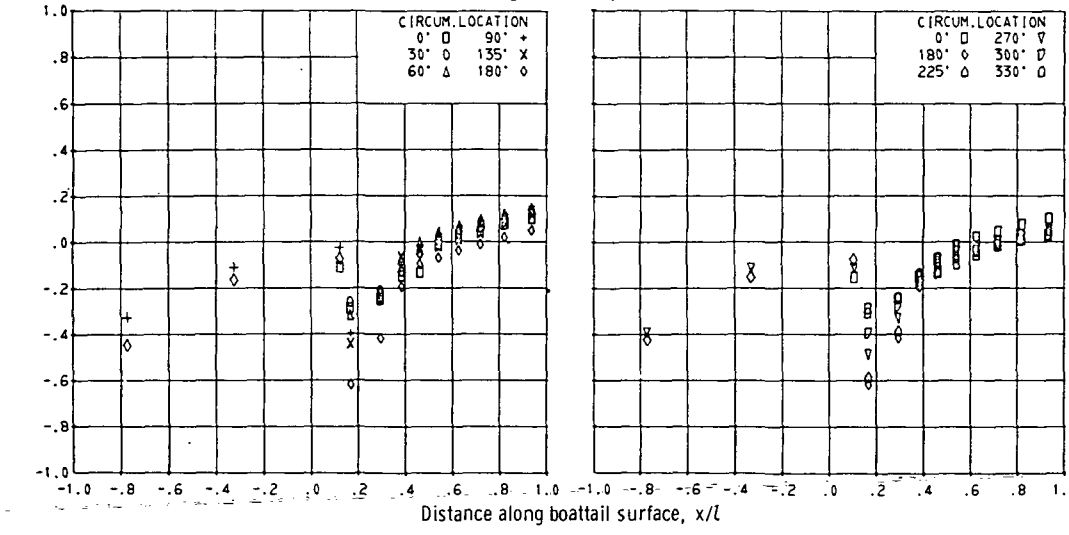

(c) Angle of attack, 13.2°.

Figure 40. - Effect of angle of attack on boattail pressure distribution. Mach 0.6; altitude, 9144 meters (30 000 ft); Reynolds number, 2.3×10^7; nozzle 25.

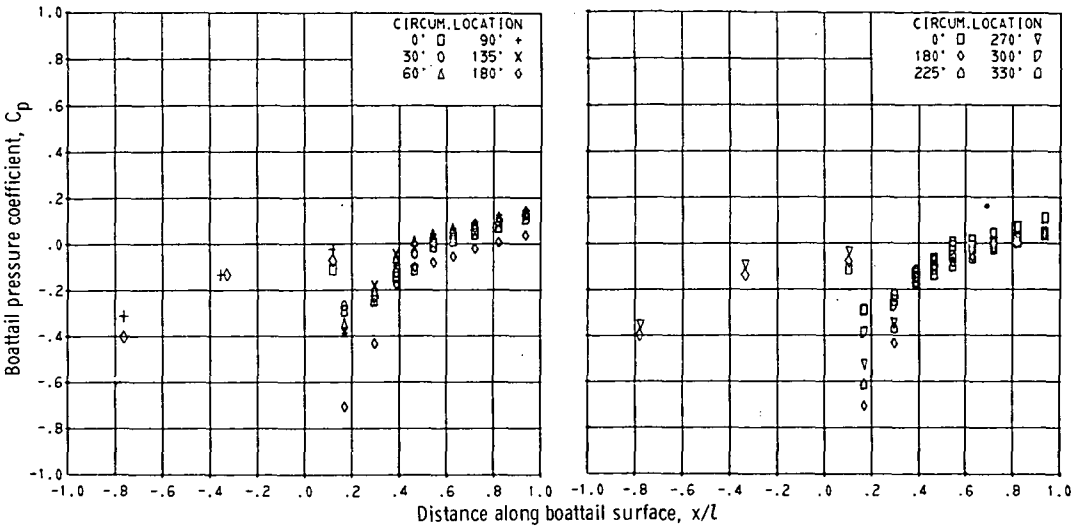

(d) Angle of attack, 14. 1^0.

Figure 40. - Concluded.

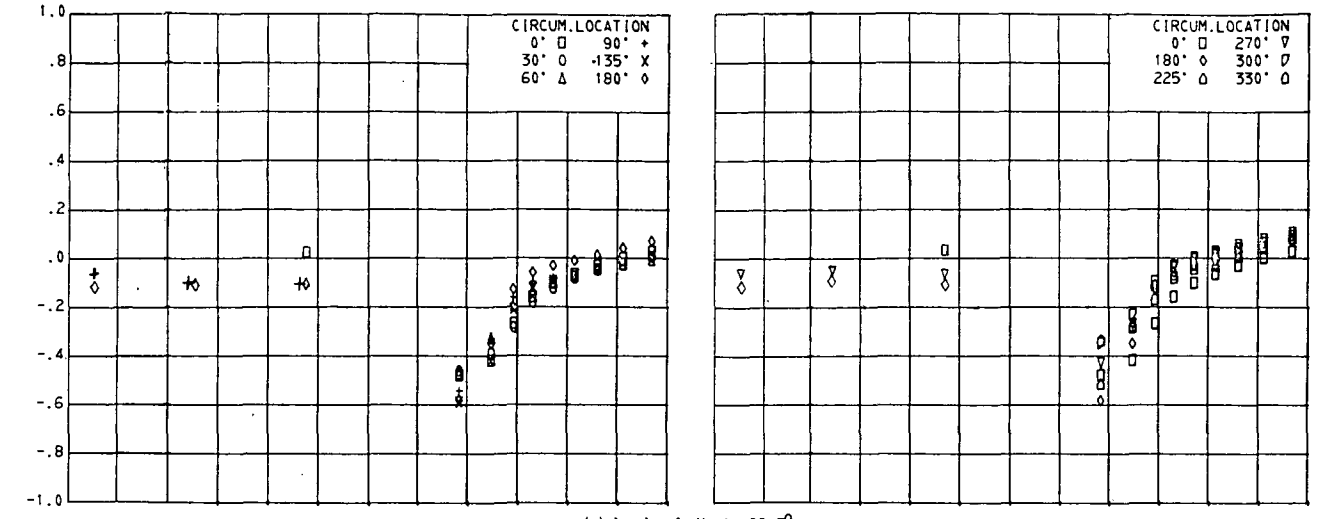

(a) Angle of attack, 11.5°.

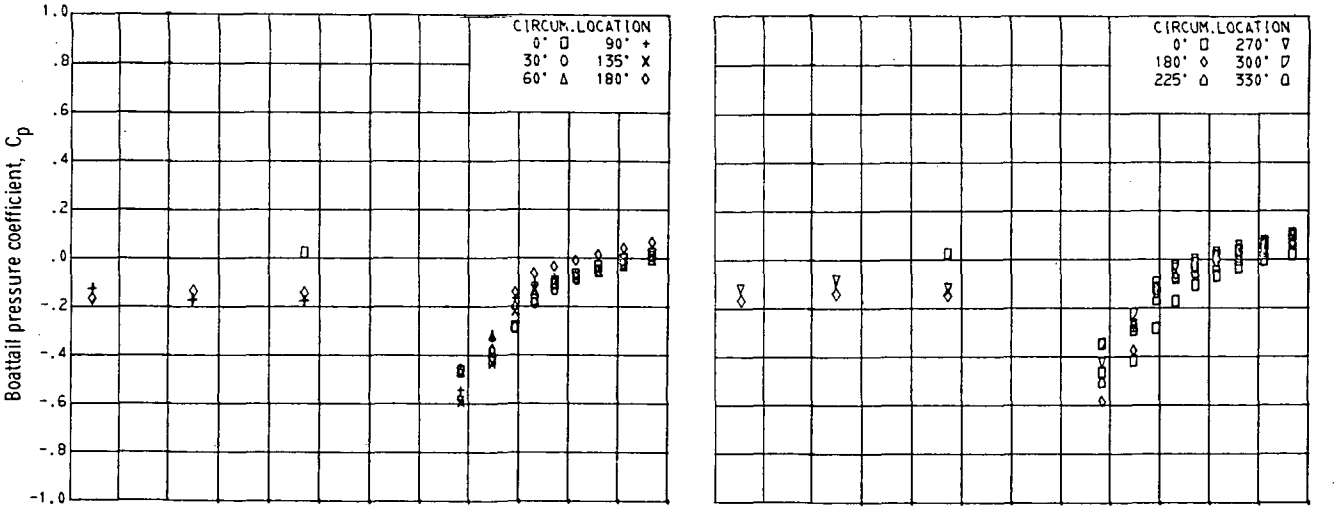

(b) Angle of attack, 12.1°.

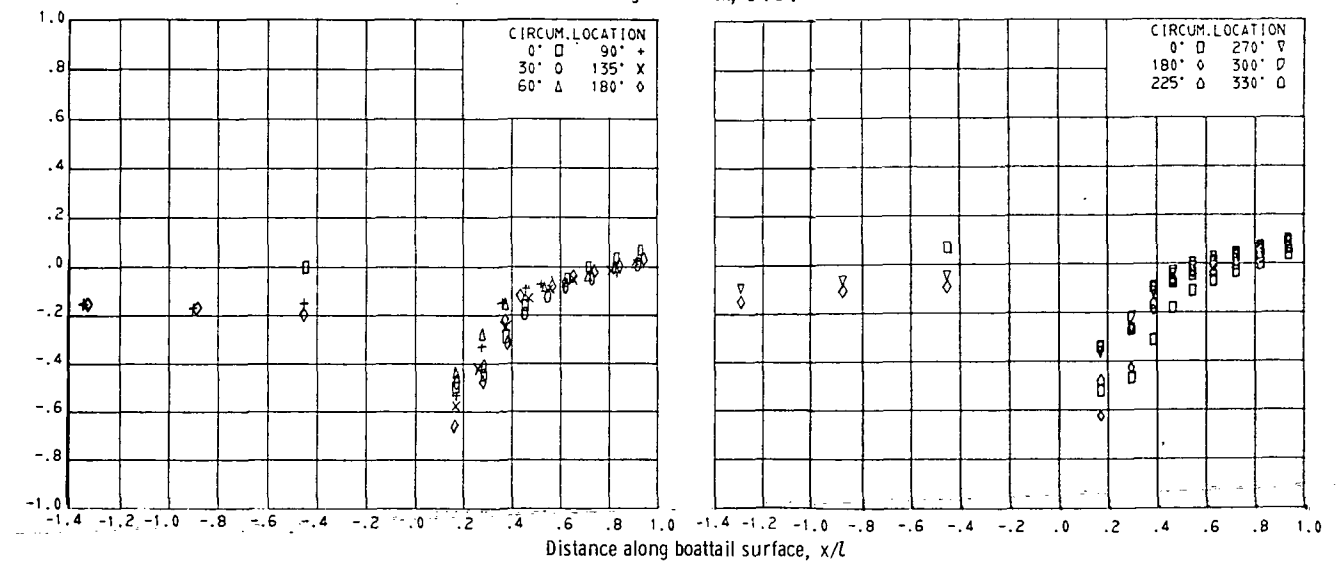

(c) Angle of attack, 13.4°.

Figure 41. - Effect of angle of attack on boattail pressure distribution. Mach 0.6; altitude, 9144 meters (30 000 ft); Reynolds number, 2.7×10^7; nozzle 25 Ex.

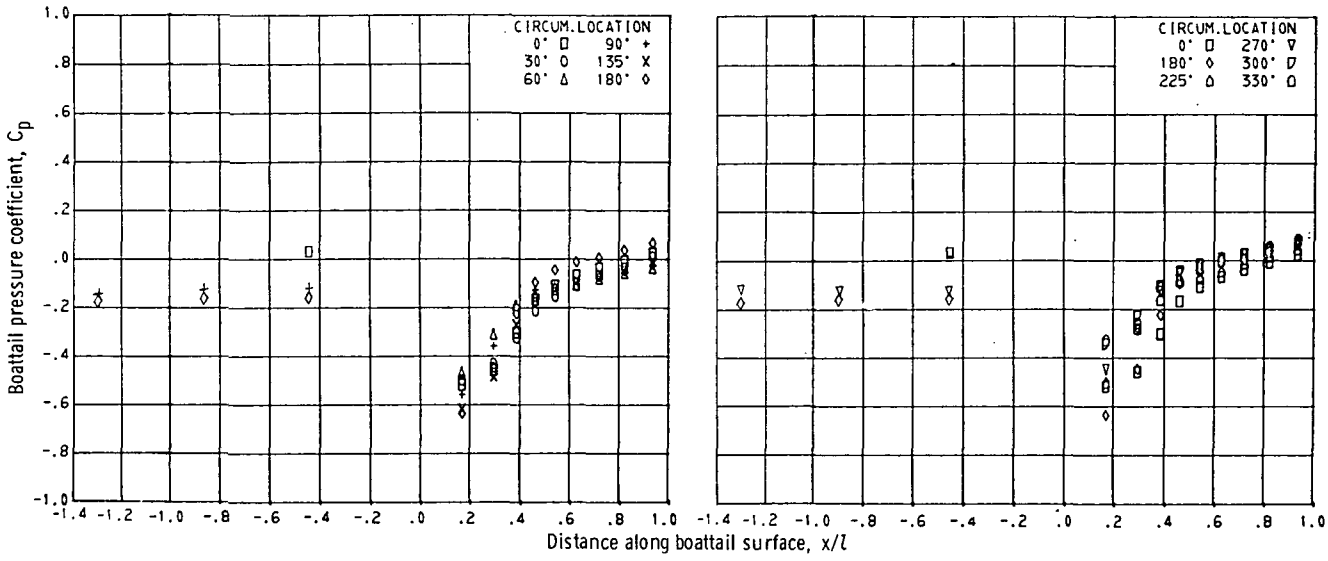

(d) Angle of attack, 14.2°.

Figure 41. - Concluded.

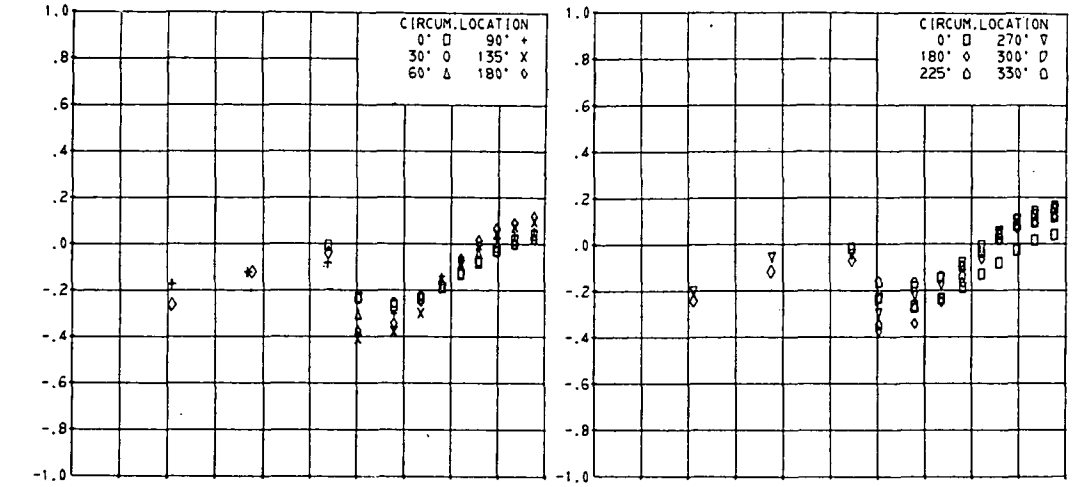

(a) Angle of attack, 11.4°.

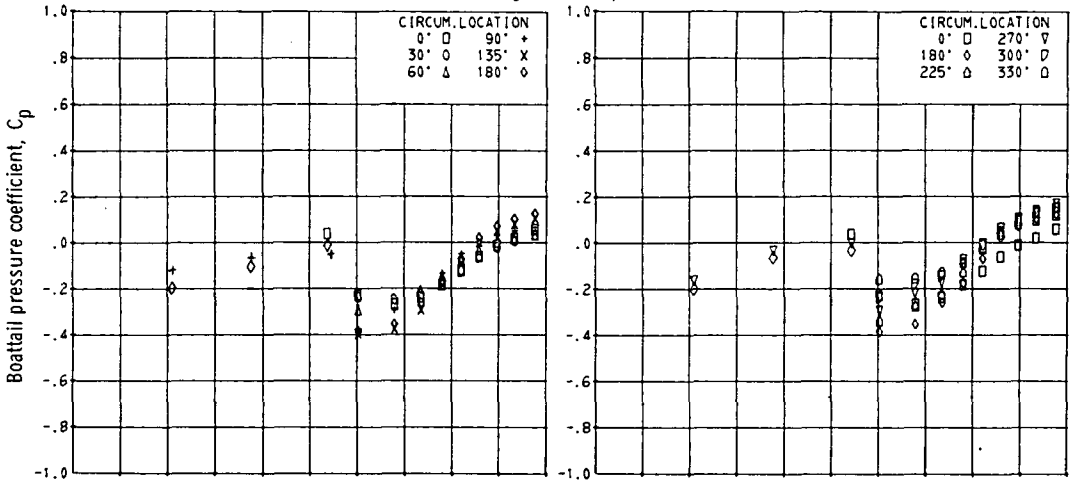

(b) Angle of attack, 12.2°.

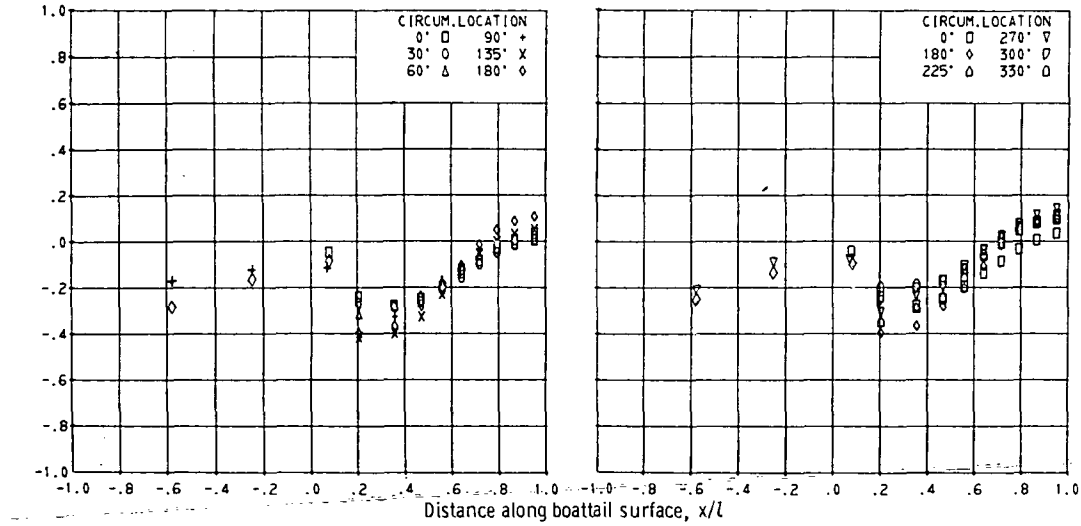

(c) Angle of attack, 13.2°.

Figure 42. - Effect of angle of attack on boattail pressure distribution. Mach 0.6; altitude, 9144 meters (30 000 ft); Reynolds number, 2.3×10^7; nozzle 65.

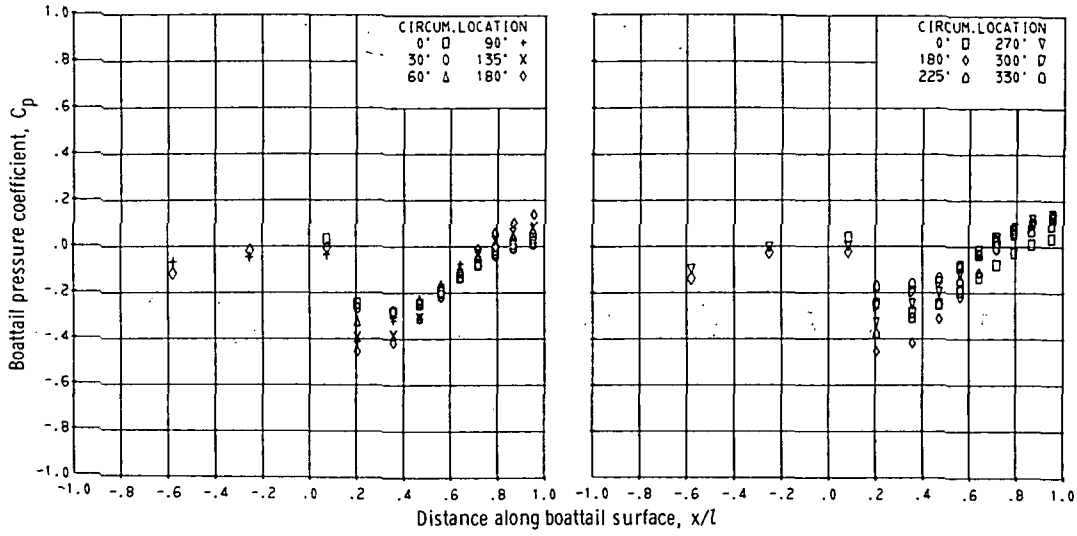

(d) Angle of attack, 14.1°.

Figure 42. - Concluded.

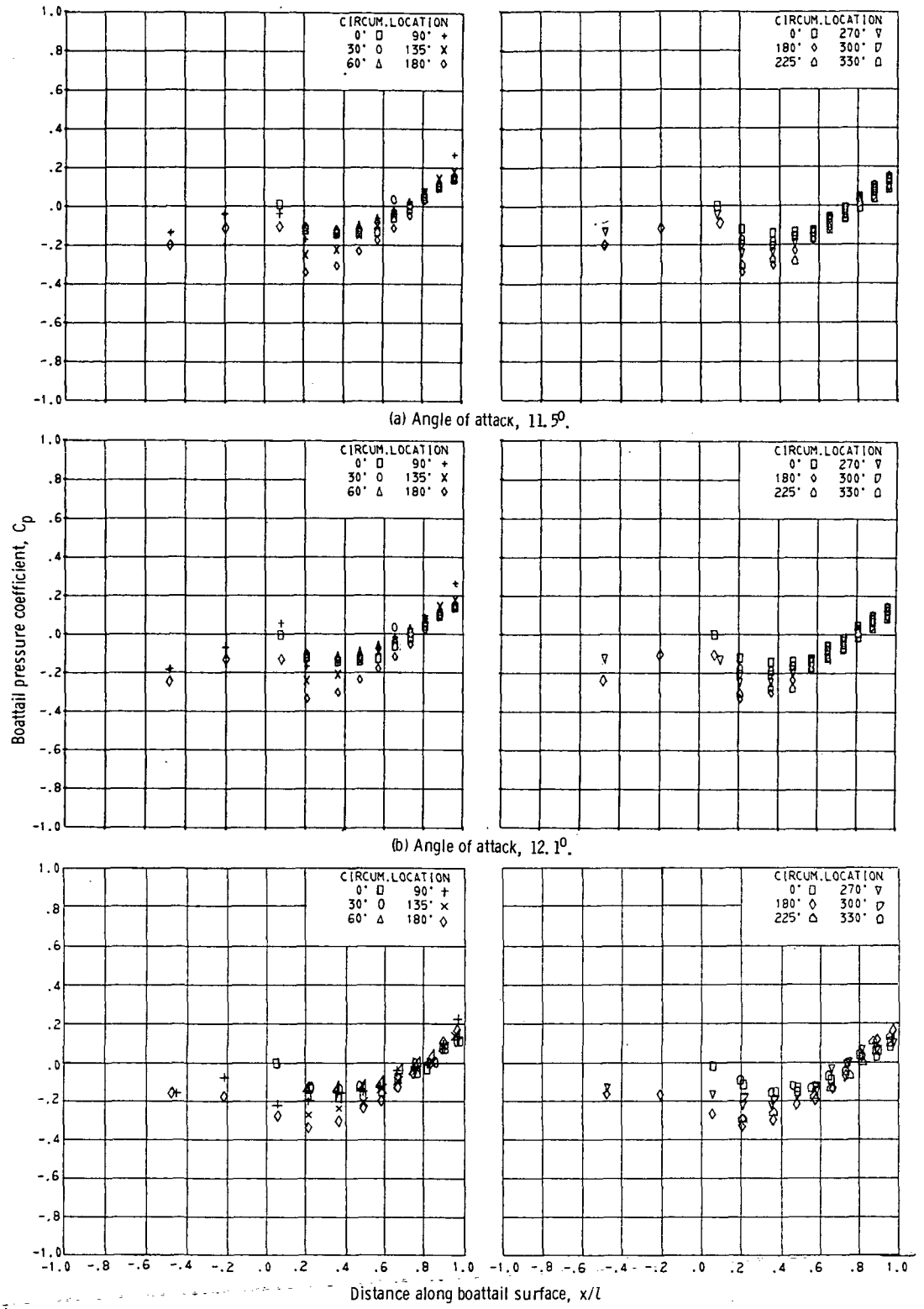

(a) Angle of attack, 11.5°.

(b) Angle of attack, 12.1°.

(c) Angle of attack, 13.4°.

Figure 43. - Effect of angle of attack on boattail pressure distribution. Mach 0.6; altitude, 9144 meters (30 000 ft); Reynolds number, 2.7×10^7; nozzle 100.

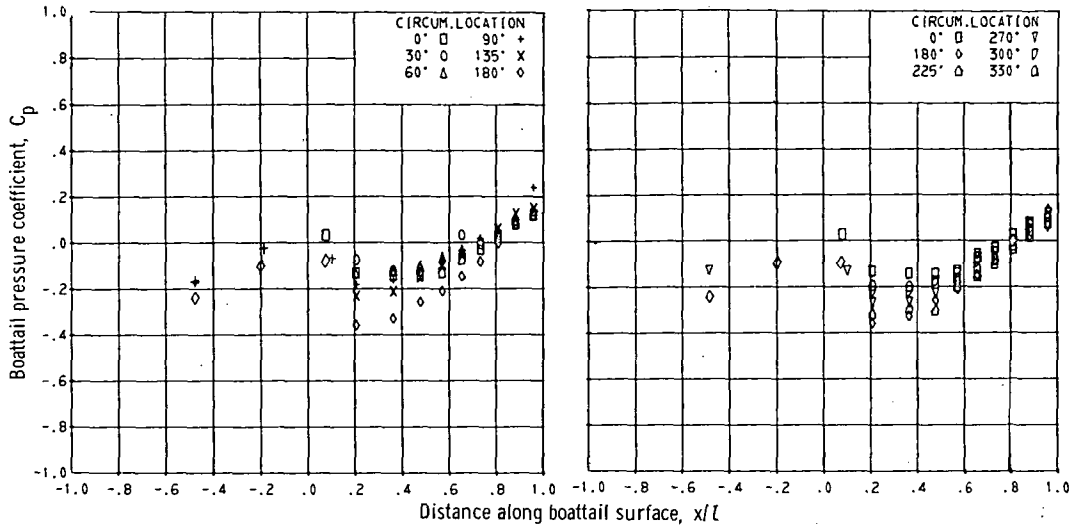

(d) Angle of attack, 14.2°.

Figure 43. - Concluded.

NATIONAL AERONAUTICS AND SPACE ADMINISTRATION
WASHINGTON, D.C. 20546

OFFICIAL BUSINESS
PENALTY FOR PRIVATE USE $300

SPECIAL FOURTH-CLASS RATE
BOOK

POSTAGE AND FEES PAID
NATIONAL AERONAUTICS AND
SPACE ADMINISTRATION
451

U.S.MAIL

POSTMASTER: If Undeliverable (Section 158 Postal Manual) Do Not Return

"The aeronautical and space activities of the United States shall be conducted so as to contribute . . . to the expansion of human knowledge of phenomena in the atmosphere and space. The Administration shall provide for the widest practicable and appropriate dissemination of information concerning its activities and the results thereof."

—NATIONAL AERONAUTICS AND SPACE ACT OF 1958

NASA SCIENTIFIC AND TECHNICAL PUBLICATIONS

TECHNICAL REPORTS: Scientific and technical information considered important, complete, and a lasting contribution to existing knowledge.

TECHNICAL NOTES: Information less broad in scope but nevertheless of importance as a contribution to existing knowledge.

TECHNICAL MEMORANDUMS: Information receiving limited distribution because of preliminary data, security classification, or other reasons. Also includes conference proceedings with either limited or unlimited distribution.

CONTRACTOR REPORTS: Scientific and technical information generated under a NASA contract or grant and considered an important contribution to existing knowledge.

TECHNICAL TRANSLATIONS: Information published in a foreign language considered to merit NASA distribution in English.

SPECIAL PUBLICATIONS: Information derived from or of value to NASA activities. Publications include final reports of major projects, monographs, data compilations, handbooks, sourcebooks, and special bibliographies.

TECHNOLOGY UTILIZATION PUBLICATIONS: Information on technology used by NASA that may be of particular interest in commercial and other non-aerospace applications. Publications include Tech Briefs, Technology Utilization Reports and Technology Surveys.

Details on the availability of these publications may be obtained from:

SCIENTIFIC AND TECHNICAL INFORMATION OFFICE

NATIONAL AERONAUTICS AND SPACE ADMINISTRATION

Washington, D.C. 20546